

D. L. Sondak R. H. Pletcher W. R. Van Dalsem

Wall Functions for the k - ϵ Turbulence Model in Generalized Nonorthogonal Curvilinear Coordinates

Final Report

Funds for the support of this study have been allocated
by the NASA-Ames Research Center, Moffett Field, California
under Interchange No. NCA2 - 526

Heat Transfer Laboratory
Department of Mechanical Engineering
Computational Fluid Dynamics Center



engineering
research institute
iowa state university



TABLE OF CONTENTS

ABSTRACT	xiii
ACKNOWLEDGEMENTS	xv
NOTATION	xvii
1. INTRODUCTION	1
1.1 Problem Description	1
1.2 Historical Review	2
1.2.1 Turbulence modeling	2
1.2.2 Near-wall modeling	8
1.3 Scope of the Present Research	10
2. CONSERVATION OF MASS, MOMENTUM, AND ENERGY .	13
2.1 Introduction	13
2.2 Instantaneous Equations	13
2.3 Averaging Techniques	14
2.4 Mass-Averaged Transport Equations	16
2.4.1 Continuity	17
2.4.2 Momentum	17
2.4.3 Energy	17

PRECEDING PAGE BLANK NOT FILMED

11 INTENTIONALLY BLANK

2.5	Closure Problem	19
3.	$k - \epsilon$ MODEL	21
3.1	Introduction	21
3.2	Turbulent Kinetic Energy Transport Equation	24
3.3	Modeled Turbulent Kinetic Energy Equation	26
3.4	Modeled Dissipation Rate Equation	28
4.	WALL FUNCTIONS	31
4.1	Background	31
4.2	Detailed Formulation	35
4.2.1	Introduction	35
4.2.2	Friction velocity	35
4.2.3	Boundary conditions for k and ϵ	36
4.2.4	Application of τ_w to the Navier-Stokes equations	40
5.	OTHER TURBULENCE MODELS	53
5.1	Introduction	53
5.2	Chien Low-Reynolds-Number Model	53
5.3	Baldwin-Lomax Algebraic Model	55
6.	NUMERICAL METHOD	57
6.1	Nondimensional Equations	57
6.2	Vector Form of Equations	58
6.3	Coordinate Transformation	61
6.4	Navier-Stokes Solver	66
6.5	$k - \epsilon$ Solver	69

7. RESULTS	73
7.1 Introduction	73
7.2 Flat plate	74
7.2.1 Skewed grid	80
7.2.2 Angled domain	81
7.2.3 Low-Reynolds-number model test case	84
7.3 Body of Revolution	90
7.3.1 Introduction	90
7.3.2 Fine grid	91
7.3.3 Medium grid	97
7.3.4 Coarse grid	102
7.4 Prolate Spheroid	102
7.4.1 Introduction	102
7.4.2 Grid	109
7.4.3 Boundary conditions	112
7.4.4 Additional considerations	117
7.4.5 Results	120
8. CONCLUSIONS AND RECOMMENDATIONS	135
9. REFERENCES	141
10. APPENDIX A: FLUX JACOBIANS	151
10.1 Navier-Stokes	151
10.2 $k - \epsilon$	154

11. APPENDIX B: $k - \epsilon$ SOLVER	155
11.1 Banded Solver	155
11.2 Block Solver	158

LIST OF TABLES

Table 4.1:	Summary of shear stress transformations	51
Table 7.1:	Previous computations of DFVLR prolate spheroid	110

LIST OF FIGURES

Figure 4.1:	Typical turbulent boundary layer velocity profile	33
Figure 4.2:	Definition of γ coordinate direction	41
Figure 4.3:	Covariant base vectors	42
Figure 4.4:	Example contravariant base vector	43
Figure 4.5:	Physical velocity components parallel to wall	48
Figure 7.1:	Orthogonal flat plate grid	76
Figure 7.2:	Friction coefficient, flat plate, orthogonal grid	79
Figure 7.3:	Velocity profile, flat plate, orthogonal grid	79
Figure 7.4:	Skewed flat plate grid	82
Figure 7.5:	Friction coefficient, flat plate, skewed grid	83
Figure 7.6:	Velocity profile, flat plate, skewed grid	84
Figure 7.7:	Friction coefficient, flat plate, angled domain	85
Figure 7.8:	Velocity profile, flat plate, angled domain	85
Figure 7.9:	Flat plate grid, low-Reynolds-number model test case	87
Figure 7.10:	Friction coefficient, flat plate, low-Reynolds-number model test case	88
Figure 7.11:	Velocity profile, flat plate, low-Reynolds-number model test case	89

Figure 7.12: Body of revolution, 101×104 grid	93
Figure 7.13: Body of revolution coordinate system	95
Figure 7.14: Pressure coefficient, body of revolution, 101×104 grid	96
Figure 7.15: Friction coefficient, body of revolution, 101×104 grid	97
Figure 7.16: Velocity profiles, body of revolution, 101×104 grid	98
Figure 7.17: Body of revolution, 101×91 grid	100
Figure 7.18: Pressure coefficient, body of revolution, 101×91 grid	101
Figure 7.19: Friction coefficient, body of revolution, 101×91 grid	101
Figure 7.20: Velocity profiles, body of revolution, 101×91 grid	103
Figure 7.21: Body of revolution, 101×80 grid	105
Figure 7.22: Pressure coefficient, body of revolution, 101×80 grid	106
Figure 7.23: Friction coefficient, body of revolution, 101×80 grid	106
Figure 7.24: Velocity profiles, body of revolution, 101×80 grid	107
Figure 7.25: Prolate spheroid, $121 \times 53 \times 57$ grid	113
Figure 7.26: Friction coefficient map from Kreplin, Vollmers, and Meier (1982)	118
Figure 7.27: Unwrapped surface grid with trip points, prolate spheroid	119
Figure 7.28: Pressure coefficient, prolate spheroid	122
Figure 7.29: Friction coefficient, prolate spheroid	125
Figure 7.30: Friction coefficient angle, prolate spheroid	129
Figure 7.31: Surface oil flow pattern, top view	132
Figure 7.32: Surface oil flow pattern, side view	133
Figure 11.1: Structure of banded matrix	156
Figure 11.2: Structure of vector of unknowns	156

Figure 11.3: Structure of right hand side 157

Figure 11.4: Structure of block matrix 159

ABSTRACT

Wall functions are often employed to model turbulent flow near solid walls. A method has not been available, however, for the application of wall functions to generalized curvilinear coordinate systems, particularly those with nonorthogonal grids. A general method for this application is developed herein.

A $k - \epsilon$ turbulence model suitable for compressible flow, including the new wall function formulation, has been incorporated into an existing compressible Reynolds-averaged Navier-Stokes code, F3D. The low-Reynolds-number $k - \epsilon$ model of Chien (1982) was added for comparison with the present method. A number of features were also added to F3D, including improved far-field boundary conditions and viscous terms in the streamwise direction.

A series of computations of increasing complexity was run to test the effectiveness of the new formulation. Flow over a flat plate was computed using both orthogonal and nonorthogonal grids, and the friction coefficients and velocity profiles compared with a semi-empirical equation. Flow over a body of revolution at zero angle of attack was then computed to test the method's ability to handle flow over a curved surface. Friction coefficients and velocity profiles were compared to test data. The same case was also computed using the Chien (1982) low-Reynolds-number $k - \epsilon$ model and the Baldwin-Lomax (1978) algebraic model for comparison. All three models gave good

results on a relatively fine grid, but only the wall function formulation was effective with coarser grids. Finally, in order to demonstrate the method's ability to handle complex flowfields, separated flow over a prolate spheroid at angle of attack was computed, and results were compared to test data. The results were also compared to the computation of Kim and Patel (1991), in which a $k - \epsilon$ model with a one-equation model patched in at the wall was employed. Both models gave reasonable solutions, but they require improvement for accurate prediction of friction coefficients in the separated regions.

ACKNOWLEDGEMENTS

The authors gratefully acknowledge the support provided for this research under NASA Ames Research Center contracts NCC2-476 and NCA2-526. Special thanks also goes to Dr. I.-T. Chiu for his help in setting up formats for figures and tables in this report, and also for his help in exorcising various computer-related gremlins along the way.

NOTATION

Roman Symbols

a	speed of sound
A, B, C	flux Jacobian matrices
a_i	covariant base vector
a^i	contravariant base vector
b	proportionality constant between metrics
B	constant for law of the wall, 5.0
c_l	constant for Norris and Reynolds near-wall length scale equation
c_p	specific heat at constant pressure
c_μ	constant for $k - \epsilon$ model, 0.09
C_{cp}	constant for Baldwin-Lomax model, 1.6
C_f	friction coefficient
C_{kleb}	constant for Baldwin-Lomax model, 0.3
C_{wk}	constant for Baldwin-Lomax model, 0.25
C_1	constant for $k - \epsilon$ model, 1.44
C_2	constant for $k - \epsilon$ model, 1.92
C_3	constant for Chien model, 0.0115

~~SECRET~~ XVI INTENTIONALLY BLANK

PRECEDING PAGE BLANK NOT FILMED

C_4	constant for Chien model, 0.5
D	dissipation term in turbulent kinetic energy transport equation
D	$k - \epsilon$ source term Jacobian matrix
\mathcal{D}	smoothing operator
e_i	unit covariant base vector
e_5^v, f_5^v, g_5^v	energy equation fluxes
E, F, G	inviscid flux vectors
E_v, F_v, G_v	viscous flux vectors
\mathcal{E}	total internal energy per unit volume
f	damping function for Chien model
F_{kleb}	Klebanoff intermittancy function, for Baldwin-Lomax model
F_{wake}	Klebanoff wake function, for Baldwin-Lomax model
$g_{\alpha\beta}$	metric tensor
\mathbf{G}	metric matrix
h	static enthalpy per unit mass
H	total enthalpy per unit mass
H_t	source term vector for turbulence transport equations
J	Jacobian of coordinate transformation
k	turbulent kinetic energy
K_c	Clauser constant for Baldwin-Lomax model, 0.02688
K	geometric stretching ratio
l	length scale
l_ϵ	near-wall length scale of Norris and Reynolds
\mathcal{N}	defined by equation (6.83)

n	coordinate direction normal to wall
p	static pressure
P	production of turbulent kinetic energy
\mathcal{P}	term proportional to production of turbulent kinetic energy
\mathbf{P}	physical shear stress matrix
Pr	Prandtl number, 0.72
Pr_t	turbulent Prandtl number, 0.9
q	heat transfer rate
Q	dependent variable vector
\mathbf{r}	position vector
R	gas constant
Re	Reynolds number based on freestream speed of sound
Re_t	turbulent Reynolds number
Re_{u_∞}	Reynolds number based on freestream velocity and reference length
Re_x	Reynolds number based on freestream velocity and distance from virtual origin
s	spectral radius of inviscid flux Jacobian
S	constant for Sutherland's law
\mathbf{S}	diagonal matrix containing functions of metrics
T	static temperature
\mathbf{T}	matrix, columns of which are right eigenvectors of inviscid flux matrix
\mathbf{T}	shear stress matrix
T_0	constant for Sutherland's law

t	time
u	velocity parallel to wall (2-D examples)
u, v, w	velocity components in physical coordinate directions
u^+	velocity normalized by friction velocity
u_*	friction velocity
$u(\alpha)$	physical velocity component in α direction
U, V, W	contravariant velocity components
W	Coles' wake function
x, y, z	physical coordinate directions
y	coordinate direction normal to wall (2-D examples)
y^+	distance from wall in wall coordinates
y_c^+	point where viscous sublayer intersects log region, neglecting buffer region
Z	function of C_f , defined by equation (7.9)

Greek Symbols

β	function to switch from fourth to second order smoothing near shocks
γ	ratio of specific heats, 1.4
γ	coordinate direction normal to wall
γ	friction coefficient angle
δ_{ij}	Kronecker delta

δ	central difference operator for inviscid fluxes
δ	boundary layer thickness
$\bar{\delta}$	central difference operator for viscous fluxes
Δ	forward difference operator
ϵ	dissipation rate of turbulent kinetic energy
ϵ_2	second difference smoothing coefficient
ϵ_4	fourth difference smoothing coefficient
ϵ	total internal energy per unit mass
θ	circumferential angle
ϑ	velocity scale
κ	Von Karman constant, 0.41
Λ	diagonal matrix containing eigenvalues of inviscid flux Jacobian
μ	molecular viscosity
μ_0	constant for Sutherland's law
μ_h	turbulent diffusion coefficient for static enthalpy
μ_t	turbulent viscosity
ν	kinematic viscosity
ν_ϕ	diffusion coefficient for passive scalar
ξ, η, ζ, τ	transformed coordinates
Π	constant for Coles' law of the wake, 0.5
ρ	density
σ_ϵ	constant for $k - \epsilon$ model, 1.3
σ_k	constant for $k - \epsilon$ model, 1.0
τ	shear stress

$\tau(\alpha\beta)$	physical shear stress components in α, β directions
ω	vorticity

Subscripts

<i>exp</i>	explicit
<i>i, j, k, l</i>	tensor indices
<i>imp</i>	implicit
<i>ref</i>	reference
<i>t</i>	turbulent
<i>v</i>	viscous
<i>w</i>	wall
<i>x, y, z</i>	partial differentiation in physical coordinate directions
α, β	tensor indices
∞	freestream

Superscripts

<i>n</i>	time level
<i>v</i>	viscous
+	wall variable
+	positive eigenvalue
-	negative eigenvalue

$'$	fluctuating quantity, Reynolds average
$''$	fluctuating quantity, Favre average

Other Symbols

∇	backward difference operator
∇	gradient operator
$—$	time average
\sim	tensor in transformed coordinates
\approx	modified by wall functions
\sim	mass-weighted average
$\hat{\sim}$	vector in transformed coordinates, conservation law form

1. INTRODUCTION

1.1 Problem Description

The understanding of turbulence is of critical importance for the prediction of flows encountered in many important engineering applications such as flow over flight vehicles, impingement cooling in industrial processes, and the transport of atmospheric pollutants. In principle, these flowfields could be predicted by solving the full Navier-Stokes equations. This approach is not practical, however, since present computers do not have the speed and memory required to resolve the wide range of length and time scales in most turbulent flows. In practice, the Navier-Stokes equations are employed to resolve large scales, and turbulence models are relied upon to simulate the effects of the small-scale motion.

Turbulence is diffusive, and most approaches to turbulence modeling are directed toward computing the rates of turbulent diffusion of momentum and energy. Unfortunately, a general method for determining these diffusion rates has proven elusive. Turbulence models have been developed which work well for certain classes of flows, but their range of applicability is limited. Some models, for example, work well for attached flows, but perform poorly in regions of separated flow.

Aside from the generality of turbulence models, another concern is the amount of computing power required to apply them. Computations of complex flows may

require millions of grid points and hundreds of hours of CPU time, even on the fastest available computers. It is therefore important to consider both accuracy and computing requirements in the development and application of turbulence models.

1.2 Historical Review

1.2.1 Turbulence modeling

The earliest attempt to analyze the turbulence problem is usually attributed to Reynolds (1895). He was trying to explain the result of his famous transition experiment in which he showed that pipe flow becomes turbulent at a distinct Reynolds number. Being familiar with the kinetic theory of gases, Reynolds tried an analogous approach for fluid flow, decomposing velocities into mean and fluctuating parts. When expressions for the decomposed velocities were substituted into the Navier-Stokes equations, a set of additional terms appeared. These terms are the gremlins which we now call the Reynolds stresses, and the subsequent ninety years or so have been littered with attempts to find a general method of predicting their values.

Since viscous stress in a Newtonian fluid is a linear function of the velocity gradient, it was hypothesized that Reynolds stresses behave in the same manner. Unfortunately, determining the proportionality constant, the turbulent viscosity, at first proved to be as intractable as determining the Reynolds stresses themselves.

In the 1920s, it was shown that transport equations could be written for moments of arbitrary order (Monin and Yaglom 1987). However, each equation for a specified moment contains the next higher moment as an unknown. For example, the equations for the Reynolds stresses, which are second order moments (the correlation between two velocity components), contain third order moments (the correlation between

three velocity components) as unknowns. This is the “closure problem” and was a harbinger of difficulties to come.

Some headway was achieved by Prandtl’s “mixing length” hypothesis. It is interesting to note that Prandtl, like Reynolds before him, turned toward the kinetic theory of gases for inspiration. According to the kinetic theory, kinematic viscosity is proportional to the product of a velocity scale (the rms velocity of the molecules) and a length scale (the mean free path of the molecules) (Hinze 1987). Treating “lumps of fluid” like molecules, Prandtl hypothesized that the turbulent viscosity is also proportional to the product of a velocity scale and a length scale. Unfortunately, the analogy with molecular motion is on shaky ground at best. Molecules retain their identity, while lumps of fluid do not. Also, the length scale of molecular motion is small compared to the overall system, and this is not the case for turbulent fluid flow (Tennekes and Lumley 1972). Even with these weaknesses, the mixing length theory has proven to be useful for the prediction of simple flowfields such as free jets and boundary layers on flat plates. Its main drawback is that the proportionality constant must be determined empirically, and a given constant is useful only for a very limited class of flows.

An approach very different from mixing length theory was taken by G. I. Taylor (1935). Since the Reynolds stresses are expressed as correlations between fluctuating components of velocity, it was natural to apply statistical methods to attempt to find general expressions for these correlations. Taylor developed this method for isotropic and, to a lesser degree, homogeneous turbulence. A great deal of insight into the mechanisms of turbulent energy transfer has been gleaned from this work. Its application to useful turbulence models has been limited, though, since turbulence

is not actually isotropic, and only approximates homogeneity for certain very simple flows, such as wind tunnel turbulence behind a grid.

While statistical methods were being developed, other approaches to improving upon mixing length theory were investigated. One of the disadvantages of mixing length models is that they do not account for “history” (transport) effects on the turbulence. To alleviate this shortcoming, one or more transport equations can be employed. It is possible to derive an exact equation for the transport of turbulent kinetic energy, although additional unknowns are introduced in the process. The new unknowns can be modeled, and the resulting equation can be used to deduce a velocity scale distribution of the turbulence. Specification of a length scale distribution then closes the problem. If the length scale is calculated algebraically, the resulting model is known as a “one-equation model,” since one partial differential equation is employed.

One-equation models yield better results than mixing length models for flows in which convection and diffusion of turbulent kinetic energy are important (Launder et al. 1972). For many complex flows, however, algebraic specification of the length scale can be difficult. The next logical step would therefore be to develop a transport equation for length scale, or a quantity which can be easily related to a length scale. This equation, along with the turbulent kinetic energy transport equation, yields a two-equation model. The second equation is usually written for the rate of dissipation of turbulent kinetic energy, ϵ , although other quantities are sometimes used, such as the length scale, L , (Rodi and Spalding 1970), the rate of dissipation per unit energy, ω , (Wilcox 1988), and the time scale, τ (Abid, Speziale, and Thangam 1991). Two-equation models came to the forefront upon publication of a series of papers from Los

Alamos Scientific Laboratory (Harlow and Nakayama 1967; Harlow and Nakayama 1968; Daly and Harlow 1970). Derivation of the second equation is not as rigorous as that of the turbulent kinetic energy equation, and this is often cited as a point of weakness of two-equation models. Even so, calculation of the length scale as part of the model has proven to be advantageous for many flowfields.

Daunted by the prospect of solving the complete second-moment equations and searching for a method to improve the performance of two-equation models, Rodi (1972) investigated the possibility of simplifying the second-moment equations. He developed an algebraic expression for the Reynolds stresses as a function of the dependent variables in his two-equation model, and the model is therefore referred to as an algebraic Reynolds stress model. Since the new equation is algebraic, little computational effort is required above that for the two-equation model. Although algebraic Reynolds stress models show promise, they have not exhibited the expected improvements over two-equation models (Ferziger 1987).

Other variations of two-equation models have also been investigated. One weakness of two-equation models is that a single velocity scale and a single length scale are assumed to be sufficient to describe the turbulence. This implies that the energy spectrum is similar in different regions of the flowfield, which is not generally true. In “multiscale” two-equation models, the energy spectrum is divided into two parts (Launder 1979). The first is the production range, which is the region of highest energy. The second is the transfer range, where the energy is transferred from large scales to small scales. Separate k and ϵ transport equations are written for each range. Multiscale models have shown improvements over standard two-equation models for flowfields such as flow over a backward-facing step (Kim and Chen 1989) and swirling

jets (Ko and Rhode 1990). The results are not consistently better, however, and a significant increase in computer power is required due to the addition of two transport equations.

Another variation of two-equation models is the “nonlinear” model. In some flowfields, anisotropy of the normal turbulent stresses is important. An example of this is the secondary flow observed to occur in turbulent flow through straight rectangular channels. Since the Boussinesq approximation does not admit anisotropy of the normal turbulent stresses, it is impossible to predict these secondary flows with the standard model. In nonlinear models (Speziale 1987; Yoshizawa 1988; Barton, Rubinstein, and Kirtley 1991), the Boussinesq approximation is replaced by a nonlinear function of the mean strain rate. This method is not restricted to two-equation models, but can be applied to other models which utilize the Boussinesq approximation (e.g., algebraic models). Initial results from these models look promising, but more applications need to be investigated before their value can be fully assessed.

As mentioned above, the closure problem precludes the solution of the transport equations for correlations between fluctuating velocity components. Also, these equations contain terms such as pressure-velocity correlations, which are generally unknown. Chou (1945) made various assumptions about the unknown quantities in the second and third moment transport equations in order to close them, creating what is now referred to as a Reynolds stress transport model. An advantage of this type of model is that the Boussinesq approximation is not employed. Although the Boussinesq approximation is effective for many types of flows, it is known to be inaccurate for some flowfields such as wall jets. Chou’s model laid fairly dormant for many years, because means for solving the equations for general cases were not avail-

able. As computers came into prominence and improved in capability, greater efforts were put into the development of Reynolds stress models. These models require a great deal of computational effort, and they do not presently yield results which are generally better than two-equation models. As they are further refined, it is expected that they will come into greater use in the future.

The goal of all techniques discussed so far is to compute the Reynolds stresses. The Reynolds stresses represent momentum transfer averaged over a wide range of scales. If a flowfield is computed using a very fine grid, large-scale structures can be resolved, and only the momentum transfer occurring at smaller scales needs to be modeled. Since the required model represents a subset of the full range of scales, it can be simpler in form than models which represent the full Reynolds stresses. This approach is called "large eddy simulation." The disadvantage of large eddy simulation is the great amount of computer power required to run with such a fine grid. This method is therefore presently constrained to relatively simple flowfields.

In theory, a grid could be constructed which is fine enough to resolve the full spectrum of scales encountered in turbulent motion, obviating the need for any turbulence model at all. This approach, "direct numerical simulation," has been applied to very simple geometries at low turbulent Reynolds numbers (e.g., Rai and Moin 1989). Since a doubling of the turbulent Reynolds number requires an order-of-magnitude increase in computer capability (Yakhot and Orszag 1986), it will not be possible to use direct simulation to solve "real world" problems in the near term future. It has been estimated that if a terraflop (10^{12} floating point operations per second) machine were available, several hundred thousand years of CPU time would still be required to compute a direct simulation of flow over an entire aircraft (Peterson et al. 1989).

This would prove to be a major annoyance to typical computer system managers, and is therefore untenable. Even so, present direct simulation results are valuable for studying the detailed structure of turbulence. Quantities which are not measurable can be extracted from the simulation results, and this is an excellent way to check details of turbulence models.

1.2.2 Near-wall modeling

As solid walls are approached, the structure of turbulent flow changes due to the increasing importance (and eventual dominance) of viscous effects. Many turbulence models have been developed with the assumption that the flow is fully turbulent (i.e., far from walls), and they require additional attention in order to model wall regions correctly.

An early near-wall model which has proven quite useful, and often appears today in many guises, is that of Van Driest (1956). Van Driest was looking for a way to modify the Prandtl mixing length to account for damping of turbulent eddies near walls. He noted that in Stokes' solution for flow over an oscillating flat plate, the amplitude of motion falls off exponentially with distance from the plate. This function may be interpreted as quantifying the region of viscous influence. Van Driest used a similar function to damp the mixing length near walls, since turbulent effects decrease as viscous effects increase.

As more complex turbulence models came into use, new approaches to modeling near-wall behavior were required. Most of these near-wall models attempt to approximate the effects of anisotropy, which are neglected elsewhere in the flowfield. These models are sometimes referred to as "low-Reynolds-number models," since they come

into play in regions of low turbulent Reynolds number. Harlow and Nakayama (1967) presented a tentative anisotropy correction to the turbulent kinetic energy in their two-equation model, but they showed no results. Daly and Harlow (1970) used a “wall-effect tensor” to modify the fluctuating pressure/strain rate correlation term in their Reynolds stress model. They showed that this term drove the peak turbulent kinetic energy closer to the wall as the Reynolds number increased, which is in accord with experimental data.

A different approach, “wall functions,” was applied by Patankar and Spalding (1970). They reasoned that equations describing the structure of turbulent boundary layers, e.g., the law of the wall, could be coupled with numerical solution schemes, thereby eliminating the need to resolve the turbulent boundary layer in the region where anisotropy is important. This technique is limited by the accuracy and range of applicability of the equations employed.

An early two-equation near-wall model which has been quite influential is that of Jones and Launder (1972). They interpreted the ϵ transport equation as modeling only the isotropic part of the dissipation rate. Using asymptotic analysis, a term was added to the turbulent kinetic energy transport equation to account for anisotropy of the dissipation rate. Damping functions were employed for several terms in the ϵ equation, and an ad-hoc term was added to bring the maximum level of turbulent kinetic energy into line with experimental data.

Development of both wall functions and low-Reynolds-number models has continued in parallel. Chieng and Launder (1980) refined the computation of the wall shear stress, and their approach has been implemented by many investigators. Their method was further generalized for compressible, separated flow by Viegas, Rubesin,

and Horstman (1985). Chien (1982) took an approach similar to that of Jones and Launder (1972) to create a low-Reynolds-number model which has gained wide acceptance. There has been a great deal of activity in recent years in the development of improved low-Reynolds-number models, usually based on asymptotic analysis. A useful comparison of eight of these models is given by Patel, Rodi, and Sheuerer (1985), where it is concluded that even the best performing models need more development if they are to be used with confidence. Avva, Smith, and Singhal (1990) directly compared results of wall functions and a common low-Reynolds-number model for three two-dimensional flowfields, and found that wall functions gave comparable or better results in all three cases.

The best choice between the two techniques has yet to be conclusively determined. Wall functions yield good results for many problems, and they require less computer power than low-Reynolds-number models. Low-Reynolds-number models have the potential to be more general and to give better results for some flowfields, but that potential has yet to be demonstrated. Both approaches will most likely continue to be used in the future.

1.3 Scope of the Present Research

One disadvantage of wall functions is that they are difficult to apply to complex geometries. Early applications generally involved two-dimensional flows over flat surfaces such as duct flows, backward-facing steps, and compression corners. Computation of flow over complex three-dimensional geometries is now commonplace, but a method for applying wall functions to these geometries has not been available. In the present work, a method has been developed for the application of wall functions

to three-dimensional generalized curvilinear coordinates with nonorthogonal grids. A high-Reynolds-number $k - \epsilon$ turbulence model with the new wall function formulation has been added to F3D, a Reynolds-averaged compressible Navier-Stokes solver. F3D utilizes an implicit, partially flux-split, two-factor approximate factorization algorithm, and the $k\epsilon$ model utilizes an implicit, fully flux-split, three-factor approximate factorization algorithm. The Chien (1982) low-Reynolds-number $k - \epsilon$ model has also been added for comparison with the wall function formulation. F3D contains the Baldwin-Lomax (1978) algebraic turbulence model, which was also run for comparison with the present method.

The new wall function technique was applied to a series of test cases. First, flow over a flat plate was computed using two different grids, one which is orthogonal and one which is skewed at the wall, to test the nonorthogonal grid capabilities of the present formulation. For these cases, the computed friction coefficients were compared with those from a semi-empirical equation. Velocity profiles were also compared with experimental data.

Flow over a body of revolution at zero angle of attack was then computed to show the method's effectiveness for flow over a curved surface. Friction coefficients and velocity profiles were compared with test data. The same case was also computed using the Chien (1982) low-Reynolds-number $k - \epsilon$ model and the Baldwin-Lomax (1978) algebraic model for comparison. Each of the cases was run on three grids with different wall spacings, demonstrating the advantage of wall functions for coarse grids.

Finally, flow over a prolate spheroid at angle of attack was computed using the wall function formulation, and results were compared with test data. This demon-

strated the effectiveness of the wall function formulation for a complex flowfield with regions of separated flow.

2. CONSERVATION OF MASS, MOMENTUM, AND ENERGY

2.1 Introduction

For turbulent flows, it is not possible to solve the equations of motion numerically due to the immense computer power which would be required to resolve the wide range of length scales. In order to make the problem tractable, the equations are averaged in time, introducing additional unknowns. The additional unknowns, which represent turbulent transport of momentum and energy, are then modeled using a combination of analysis and empiricism. In this chapter, the technique for averaging fluctuating quantities is presented, and it is then applied to the equations of motion.

2.2 Instantaneous Equations

The working fluid is assumed to be a homogeneous continuum, and therefore may not contain voids or particulates. It is also assumed that the fluid is Newtonian, i.e. that the stress is proportional to the rate of strain. Stokes' hypothesis that the bulk and molecular viscosities (λ and μ respectively) are related by the equation $\lambda = -(2/3)\mu$ is employed. Finally, buoyancy and other body forces are neglected. Given these assumptions, the equations of conservation of mass per unit volume,

momentum per unit volume, and total enthalpy per unit volume are given by

$$\frac{\partial \rho}{\partial t} + \frac{\partial}{\partial x_j}(\rho u_j) = 0 \quad (2.1)$$

$$\frac{\partial}{\partial t}(\rho u_i) + \frac{\partial}{\partial x_j}(\rho u_i u_j + \delta_{ij} p - \tau_{ij}) = 0 \quad (2.2)$$

$$\frac{\partial}{\partial t}(\rho H - p) + \frac{\partial}{\partial x_j}(\rho u_j H + q_j - u_i \tau_{ij}) = 0 \quad (2.3)$$

where

$$\tau_{ij} = \mu \left(\frac{\partial u_i}{\partial x_j} + \frac{\partial u_j}{\partial x_i} - \frac{2}{3} \delta_{ij} \frac{\partial u_k}{\partial x_k} \right) \quad (2.4)$$

This is a system of five equations with seven unknowns, and must be closed with the aid of an equation of state and an expression for molecular viscosity. The fluid is assumed to be a perfect gas,

$$p = \rho RT \quad (2.5)$$

where temperature is related to total enthalpy by

$$H = h + \frac{1}{2}(u_i u_i) \quad (2.6)$$

$$= c_p T + \frac{1}{2}(u_i u_i) \quad (2.7)$$

The molecular viscosity will be calculated from Sutherland's Law (White 1974),

$$\frac{\mu}{\mu_0} \approx \left(\frac{T}{T_0} \right)^{3/2} \frac{T_0 + S}{T + S} \quad (2.8)$$

where for air, $\mu_0 = 0.1716 mP$, $T_0 = 491.6^\circ R$, and $S = 199^\circ R$.

2.3 Averaging Techniques

Following Reynolds' approach toward dealing with turbulent flow, values of velocity and fluid properties are decomposed into mean and fluctuating parts. There are

two common techniques of decomposition, “Reynolds averaging” and “mass-weighted averaging.” Reynolds averaging is usually employed for incompressible flows, while mass-weighted averaging is more convenient for compressible flows. Here, the word “average” will be used to refer to averaging over time, defined by

$$\bar{\phi} = \frac{1}{\Delta t} \int_t^{t+\Delta t} \phi d\tau \quad (2.9)$$

where ϕ is the quantity being averaged, and t is time. In practice, the time must be large with respect to the fluctuation time scale, but small with respect to the time scale of global changes in the mean flowfield.

The mass-weighted average is defined by

$$\tilde{\phi} = \frac{\overline{\rho\phi}}{\bar{\rho}} \quad (2.10)$$

where ρ represents density, and the tilde is used to indicate a mass-weighted average.

In Reynolds decomposition, quantities are decomposed into mean and fluctuating parts as follows:

$$\phi = \bar{\phi} + \phi' \quad (2.11)$$

where ϕ is the instantaneous value of the quantity being averaged, $\bar{\phi}$ is defined by equation (2.9), and ϕ' is the fluctuating part of ϕ . The analogous equation for mass-weighted averaging is

$$\phi = \tilde{\phi} + \phi'' \quad (2.12)$$

Now several useful properties of these averages will be developed. First averages of fluctuating components will be examined. From equations (2.9) and (2.11),

$$\begin{aligned}
\overline{\phi'} &= \frac{1}{\Delta t} \int_t^{t+\Delta t} (\phi - \bar{\phi}) d\tau \\
&= \frac{1}{\Delta t} \int_t^{t+\Delta t} \phi d\tau - \frac{1}{\Delta t} \int_t^{t+\Delta t} \bar{\phi} d\tau \\
&= \bar{\phi} - \bar{\phi} \\
&= 0
\end{aligned} \tag{2.13}$$

For mass-weighted averages,

$$\begin{aligned}
\overline{\rho\phi''} &= \frac{1}{\Delta t} \int_t^{t+\Delta t} \rho\phi'' d\tau \\
&= \frac{1}{\Delta t} \int_t^{t+\Delta t} \rho(\phi - \tilde{\phi}) d\tau \\
&= \frac{1}{\Delta t} \int_t^{t+\Delta t} \rho\phi d\tau - \frac{1}{\Delta t} \int_t^{t+\Delta t} \rho\tilde{\phi} d\tau \\
&= \overline{\rho\phi} - \overline{\rho\tilde{\phi}}
\end{aligned}$$

From equation (2.10), $\overline{\rho\phi} = \overline{\rho\tilde{\phi}}$, so

$$\overline{\rho\phi''} = 0 \tag{2.14}$$

It is important to note that $\overline{\phi''} \neq 0$.

2.4 Mass-Averaged Transport Equations

The variables in the continuity, momentum, and energy equations will now be decomposed into average and fluctuating components, and the results averaged. Equation (2.11) will be used to decompose ρ , p , and τ , and equation (2.12) will be used for u_j and H .

2.4.1 Continuity

Decomposing the variables in the continuity equation (2.1) and averaging yields

$$\frac{\partial}{\partial t}(\overline{\rho} + \rho') + \frac{\partial}{\partial x_j} \overline{\rho(\tilde{u}_j + u_j'')} = 0 \quad (2.15)$$

Applying equations (2.13) and (2.14),

$$\frac{\partial}{\partial t} \overline{\rho} + \frac{\partial}{\partial x_j} (\overline{\rho \tilde{u}_j}) = 0 \quad (2.16)$$

2.4.2 Momentum

Decomposing and averaging the momentum equation (2.2) yields

$$\begin{aligned} \frac{\partial}{\partial t} \overline{[\rho(\tilde{u}_i + u_i'')] } + \frac{\partial}{\partial x_j} \overline{[\rho(\tilde{u}_i + u_i'')(\tilde{u}_j + u_j'')] } \\ + \delta_{ij} \frac{\partial}{\partial x_j} (\overline{\rho} + \rho') - \frac{\partial}{\partial x_j} (\overline{\tau_{ij} + \tau_{ij}''}) = 0 \end{aligned} \quad (2.17)$$

Applying equations (2.13) and (2.14),

$$\frac{\partial}{\partial t} (\overline{\rho \tilde{u}_i}) + \frac{\partial}{\partial x_j} [\overline{\rho \tilde{u}_i \tilde{u}_j} + \delta_{ij} \overline{\rho} - (\overline{\tau_{ij}} - \overline{\rho u_i'' u_j''})] = 0 \quad (2.18)$$

2.4.3 Energy

Decomposing and averaging the energy equation (2.3) yields

$$\begin{aligned} \frac{\partial}{\partial t} \overline{[\rho(\tilde{H} + H'')] } \\ + \frac{\partial}{\partial x_j} \overline{[\rho(\tilde{u}_j + u_j'')(\tilde{H} + H'')] + (\overline{q_j} + q_j') - (\tilde{u}_j + u_j'')(\overline{\tau_{ij}} + \tau_{ij}'')] } = 0 \end{aligned} \quad (2.19)$$

Applying equations (2.13) and (2.14),

$$\frac{\partial}{\partial t} (\overline{\rho \tilde{H}} - \overline{\rho}) + \frac{\partial}{\partial x_j} [\overline{\rho \tilde{u}_j \tilde{H}} + \overline{\rho u_j'' H''} + \overline{q_j} - \tilde{u}_i \overline{\tau_{ij}} - \overline{u_i'' \tau_{ij}''}] = 0 \quad (2.20)$$

It will be useful to express H'' in terms of h'' , \tilde{u}_i , u_i'' , ρ , and $\bar{\rho}$. From the definition of total enthalpy,

$$H \equiv h + \frac{1}{2}u_i u_i \quad (2.21)$$

$$= \tilde{h} + h'' + \frac{1}{2}(\tilde{u}_i + u_i'')(\tilde{u}_i + u_i'') \quad (2.22)$$

$$= \left(\tilde{h} + \frac{1}{2}\tilde{u}_i \tilde{u}_i\right) + \left(h'' + \frac{1}{2}u_i'' u_i''\right) + \tilde{u}_i u_i'' \quad (2.23)$$

The definition of mass-average, equation (2.10), applied to the total enthalpy gives

$$\tilde{H} = \frac{\overline{\rho H}}{\bar{\rho}} \quad (2.24)$$

$$= \frac{\overline{\rho \left(h + \frac{1}{2}u_i u_i\right)}}{\bar{\rho}} \quad (2.25)$$

$$= \tilde{h} + \frac{\overline{\frac{1}{2}\rho(\tilde{u}_i + u_i'')(\tilde{u}_i + u_i'')}}{\bar{\rho}} \quad (2.26)$$

$$= \tilde{h} + \frac{1}{2}\tilde{u}_i \tilde{u}_i + \frac{1}{2}\frac{\overline{\rho u_i'' u_i''}}{\bar{\rho}} \quad (2.27)$$

Subtracting equation (2.27) from equation (2.23) yields an expression for the fluctuating component of total enthalpy,

$$H'' = h'' + \frac{1}{2}u_i'' u_i'' - \frac{1}{2}\frac{\overline{\rho u_i'' u_i''}}{\bar{\rho}} + \tilde{u}_i u_i'' \quad (2.28)$$

Applying this equation to equation (2.20) yields

$$\frac{\partial}{\partial t}(\bar{\rho}\tilde{H} - \bar{p}) + \frac{\partial}{\partial x_j} \left[\bar{\rho}\tilde{u}_j \tilde{H} + \overline{\rho u_j'' h''} + \bar{q}_j - \tilde{u}_i (\tau_{ij} - \overline{\rho u_i'' u_j''}) - \overline{u_i'' (\tau_{ij} - \frac{1}{2}\rho u_i'' u_j'')} \right] = 0 \quad (2.29)$$

If the boundary-layer approximation is used, the last term on the left hand side may be neglected (Cebeci and Smith 1974; Anderson, Tannehill, and Pletcher 1984). It is common practice to neglect this term even in full Navier-Stokes computations, and this approximation will be used here.

The energy equation may be expressed in terms of total internal energy rather than total enthalpy. Let the total internal energy per unit mass be denoted by ε .

$$\varepsilon = H - \frac{p}{\rho} \quad (2.30)$$

Multiplying by ρ , dividing by $\bar{\rho}$, and averaging gives

$$\frac{\bar{\rho}\bar{\varepsilon}}{\bar{\rho}} = \frac{\bar{\rho}\bar{H}}{\bar{\rho}} - \frac{\bar{p}}{\bar{\rho}} \quad (2.31)$$

Using the definition of mass-average and rearranging,

$$\bar{\rho}\bar{\varepsilon} = \bar{\rho}\bar{H} - \bar{p} \quad (2.32)$$

Applying equation (2.32) to equation (2.29) and using the approximation $\overline{u_i''(\tau_{ij} - \frac{1}{2}u_i''u_j'')} = 0$ discussed above,

$$\frac{\partial}{\partial t}(\bar{\rho}\bar{\varepsilon}) + \frac{\partial}{\partial x_j} [\bar{\rho}\tilde{u}_j\bar{\varepsilon} + \tilde{u}_j\bar{p} + \overline{\rho u_j'' h''} + \bar{q}_j - \tilde{u}_i(\bar{\tau}_{ij} - \overline{\rho u_i'' u_j''})] = 0 \quad (2.33)$$

Finally, letting $\tilde{\mathcal{E}}$ denote the total internal energy per unit volume, $\tilde{\mathcal{E}} = \bar{\rho}\bar{\varepsilon}$,

$$\frac{\partial}{\partial t}(\tilde{\mathcal{E}}) + \frac{\partial}{\partial x_j} [(\tilde{\mathcal{E}} + \bar{p})\tilde{u}_j + \overline{\rho u_j'' h''} + \bar{q}_j - \tilde{u}_i(\bar{\tau}_{ij} - \overline{\rho u_i'' u_j''})] = 0 \quad (2.34)$$

2.5 Closure Problem

The mass-averaged momentum equation (2.18) looks very much like the instantaneous momentum equation (2.2) with the additional term $-\overline{\rho u_i'' u_j''}$. This term, the Reynolds stress, represents the rate of momentum transfer due to turbulent velocity fluctuations. Unfortunately, its value is unknown, and the set of equations is no longer closed. One's first inclination might be to derive transport equations for the Reynolds stresses. Unfortunately, these equations for second-order moments (averages of products of two fluctuating quantities) contain third-order moments, which

are also unknown. Indeed, transport equations for any moments will contain terms with higher-order moments. This is the infamous “closure problem.”

In addition to the Reynolds stresses, there is an additional unknown quantity in the energy equation (2.34), $\overline{\rho u_j'' h''}$. This term represents the transport of energy by turbulent velocity fluctuations.

Both of the unknowns will be computed from a turbulence model, thereby re-establishing a closed set of equations.

3. $k - \epsilon$ MODEL

3.1 Introduction

The first task at hand is to model the Reynolds stress term. A coefficient of turbulent diffusion may be defined based on the assumption that the turbulent shear stresses are proportional to the mean strain rate, in analogy with molecular diffusion. An additional term is required to account for the turbulent normal stresses. The resulting equation, the Boussinesq approximation, is given by (Anderson, Tannehill, and Pletcher 1984)

$$-\overline{\rho u_i'' u_j''} = \mu_t \left(\frac{\partial \tilde{u}_i}{\partial x_j} + \frac{\partial \tilde{u}_j}{\partial x_i} - \frac{2}{3} \delta_{ij} \frac{\partial \tilde{u}_k}{\partial x_k} \right) - \frac{2}{3} \delta_{ij} \bar{\rho} \tilde{k} \quad (3.1)$$

where k , the turbulent kinetic energy per unit mass, is defined by

$$k \equiv \frac{1}{2} u_i'' u_i'' \quad (3.2)$$

The last term on the right hand side is not included by some authors. Without it, however, the turbulent kinetic energy would be identically equal to zero for incompressible flow. This may be seen by contracting the indices ($i = j$).

The unknown Reynolds stress tensor has now been replaced with a function of dependent variables from the Navier-Stokes equations as well as two additional unknown scalars, the turbulent viscosity μ_t and the turbulent kinetic energy \tilde{k} .

It is now assumed that μ_t is proportional to the product of a velocity scale and a length scale of the large-scale turbulent motion. It is convenient to work with ν_t , which is defined as $\nu_t = \mu_t/\bar{\rho}$, rather than μ_t .

$$\nu_t \propto \vartheta l \tag{3.3}$$

Both scales may vary with space and time. The velocity scale will be taken to be equal to the square root of the turbulent kinetic energy,

$$\vartheta = \sqrt{\tilde{k}} \tag{3.4}$$

and the length scale will be defined by

$$l = \frac{\tilde{k}^{3/2}}{\tilde{\epsilon}} \tag{3.5}$$

where $\tilde{\epsilon}$ is the rate of dissipation of turbulent kinetic energy. Combining equations (3.3), (3.4), and (3.5), and defining c_μ to be the proportionality constant,

$$\nu_t = c_\mu \frac{\tilde{k}^2}{\tilde{\epsilon}} \tag{3.6}$$

Assuming that the constant c_μ can be determined empirically, knowledge of \tilde{k} and $\tilde{\epsilon}$ would result in knowledge of the Reynolds stresses.

There is an additional unknown in the energy equation (2.34), $\overline{\rho u_j'' h''}$, which also requires some attention. In analogy with the kinematic viscosity, Hinze (1987) defines a coefficient of turbulent convective transport for a passive scalar,

$$-\overline{u_i' \phi'} = \nu_\phi \frac{\partial \bar{\phi}}{\partial x_i} \tag{3.7}$$

Note that the sign is different on each side of the equation. For mass-averaged quantities, it is convenient to define a turbulent diffusion coefficient analogous to the

molecular viscosity. For static enthalpy, this coefficient is given by

$$-\overline{\rho u_j'' h''} = \mu_h \frac{\partial \tilde{h}}{\partial x_j} \quad (3.8)$$

A turbulent Prandtl number will be defined to relate μ_h to μ_t ,

$$\mu_h = \frac{\mu_t}{Pr_t} \quad (3.9)$$

The turbulent Prandtl number is known to vary with space, but a functional relationship has not been well established (Anderson, Tannehill, and Pletcher 1984). Most algebraic turbulence models give good results if the turbulent Prandtl number is assumed to be a constant (Anderson, Tannehill, and Pletcher 1984), and this assumption is also usually made for more complex turbulence models. The commonly-used value of $Pr_t = 0.9$ will be adopted here.

The static enthalpy will now be expressed in terms of the speed of sound a . For a perfect gas,

$$\tilde{h} = c_p \tilde{T} \quad (3.10)$$

$$= \frac{c_p}{\gamma R} \tilde{a}^2 \quad (3.11)$$

$$= \frac{\tilde{a}^2}{\gamma - 1} \quad (3.12)$$

Combining equations (3.8), (3.9), and (3.12) yields the final form,

$$-\overline{\rho u_i'' h''} = \frac{\mu_t}{Pr_t(\gamma - 1)} \frac{\partial \tilde{a}^2}{\partial x_i} \quad (3.13)$$

The point has now been reached such that the equation set will be closed if the \tilde{k} and $\tilde{\epsilon}$ fields are known. Transport equations for \tilde{k} and $\tilde{\epsilon}$ will now be written to effect this closure.

3.2 Turbulent Kinetic Energy Transport Equation

The momentum equation (2.2) may be rewritten, replacing the subscript i with k :

$$\frac{\partial}{\partial t}(\rho u_k) + \frac{\partial}{\partial x_j}(\rho u_k u_j + \delta_{kj} p - \tau_{kj}) = 0 \quad (3.14)$$

Now, multiplying equation (2.2) by u_k , equation (3.14) by u_i , adding the results, applying the continuity equation (2.1), and simplifying, yields the moment of momentum equation:

$$\frac{\partial}{\partial t}(\rho u_i u_k) + \frac{\partial}{\partial x_j}(\rho u_i u_j u_k) + u_k \frac{\partial p}{\partial x_i} - u_k \frac{\partial \tau_{jk}}{\partial x_j} + u_i \frac{\partial p}{\partial x_k} - u_i \frac{\partial \tau_{jk}}{\partial x_j} = 0 \quad (3.15)$$

This equation will now be averaged.

$$\begin{aligned} & \frac{\partial}{\partial t} \left[\overline{\rho (\tilde{u}_k + u_k'') (\tilde{u}_i + u_i'')} \right] + \frac{\partial}{\partial x_j} \left[\overline{\rho (\tilde{u}_i + u_i'') (\tilde{u}_k + u_k'') (\tilde{u}_j + u_j'')} \right] \\ & + \overline{(\tilde{u}_k + u_k'') \frac{\partial p}{\partial x_i}} + \overline{(\tilde{u}_i + u_i'') \frac{\partial p}{\partial x_k}} - \overline{(\tilde{u}_k + u_k'') \frac{\partial \tau_{ij}}{\partial x_j}} - \overline{(\tilde{u}_i + u_i'') \frac{\partial \tau_{kj}}{\partial x_j}} = 0 \end{aligned} \quad (3.16)$$

Rearranging, and applying equation (2.14), yields

$$\begin{aligned} & \frac{\partial}{\partial t} (\overline{\rho \tilde{u}_i \tilde{u}_k}) + \frac{\partial}{\partial x_j} (\overline{\rho \tilde{u}_i \tilde{u}_j \tilde{u}_k}) + \tilde{u}_k \frac{\partial \bar{p}}{\partial x_i} + \tilde{u}_i \frac{\partial \bar{p}}{\partial x_k} - \tilde{u}_k \frac{\partial \bar{\tau}_{ij}}{\partial x_j} - \tilde{u}_i \frac{\partial \bar{\tau}_{kj}}{\partial x_j} \\ & + \frac{\partial}{\partial t} (\overline{\rho u_i'' u_k''}) + \frac{\partial}{\partial x_j} (\overline{\rho u_j'' u_k'' \tilde{u}_i} + \overline{\rho u_i'' u_k'' \tilde{u}_j} + \overline{\rho u_i'' u_j'' \tilde{u}_k} + \overline{\rho u_i'' u_j'' u_k''}) \\ & + \overline{u_k'' \frac{\partial p}{\partial x_i}} + \overline{u_i'' \frac{\partial p}{\partial x_k}} - \overline{u_k'' \frac{\partial \tau_{ij}}{\partial x_j}} - \overline{u_i'' \frac{\partial \tau_{kj}}{\partial x_j}} = 0 \end{aligned} \quad (3.17)$$

The ‘‘moment of mean momentum’’ equation is also needed. This equation may be derived in exactly the same way as equation (3.15), but starting with the mean momentum equation (2.18), and multiplying by \tilde{u}_k and \tilde{u}_i rather than u_k and u_i .

The result is

$$\begin{aligned} \frac{\partial}{\partial t} (\overline{\rho \tilde{u}_i \tilde{u}_k}) + \frac{\partial}{\partial x_j} (\overline{\rho \tilde{u}_i \tilde{u}_j \tilde{u}_k}) + \tilde{u}_k \frac{\partial \overline{p}}{\partial x_i} + \tilde{u}_i \frac{\partial \overline{p}}{\partial x_k} \\ - \tilde{u}_k \frac{\partial \overline{\tau_{ij}}}{\partial x_j} - \tilde{u}_i \frac{\partial \overline{\tau_{kj}}}{\partial x_j} + \tilde{u}_k \frac{\partial}{\partial x_j} (\overline{\rho u_i'' u_j''}) + \tilde{u}_i \frac{\partial}{\partial x_j} (\overline{\rho u_j'' u_k''}) = 0 \end{aligned} \quad (3.18)$$

Now, subtracting equation (3.18) from (3.17) yields a transport equation for the Reynolds stresses:

$$\begin{aligned} \frac{\partial}{\partial t} (\overline{\rho u_i'' u_k''}) + \frac{\partial}{\partial x_j} (\tilde{u}_j \overline{\rho u_i'' u_k''}) \\ = -\overline{u_k'' \frac{\partial p}{\partial x_i}} - \overline{u_i'' \frac{\partial p}{\partial x_k}} + \overline{u_k'' \frac{\partial \tau_{ij}}{\partial x_j}} + \overline{u_i'' \frac{\partial \tau_{kj}}{\partial x_j}} \\ - \overline{\rho u_j'' u_k'' \frac{\partial \tilde{u}_i}{\partial x_j}} - \overline{\rho u_i'' u_j'' \frac{\partial \tilde{u}_k}{\partial x_j}} - \frac{\partial}{\partial x_j} (\overline{\rho u_i'' u_j'' u_k''}) \end{aligned} \quad (3.19)$$

Contracting equation (3.19) ($k = i$) and dividing the resulting equation by 2 yields

$$\begin{aligned} \frac{\partial}{\partial t} \left(\frac{1}{2} \overline{\rho u_i'' u_i''} \right) + \frac{\partial}{\partial x_j} \left(\frac{1}{2} \tilde{u}_j \overline{\rho u_i'' u_i''} \right) \\ = -\overline{u_i'' \frac{\partial p}{\partial x_i}} + \overline{u_i'' \frac{\partial \tau_{ij}}{\partial x_j}} \\ - \overline{\rho u_i'' u_j'' \frac{\partial \tilde{u}_i}{\partial x_j}} - \frac{\partial}{\partial x_j} \left(\frac{1}{2} \overline{\rho u_i'' u_i'' u_j''} \right) \end{aligned} \quad (3.20)$$

The turbulent kinetic energy per unit mass was defined by equation (3.2). With the aid of equation (2.10), its average is given by

$$\bar{k} = \frac{1}{\bar{\rho}} \frac{1}{2} \overline{\rho u_i'' u_i''} \quad (3.21)$$

Finally, substituting equation (3.21) into (3.20) yields the equation for the transport of turbulent kinetic energy,

$$\begin{aligned}
& \frac{\partial}{\partial t} (\overline{\rho \tilde{k}}) + \frac{\partial}{\partial x_j} (\tilde{u}_j \overline{\rho \tilde{k}}) \\
& = -\overline{u_i'' \frac{\partial p}{\partial x_i}} + \overline{u_i'' \frac{\partial \tau_{ij}}{\partial x_j}} - \overline{\rho u_i'' u_j''} \frac{\partial \tilde{u}_i}{\partial x_j} - \frac{\partial}{\partial x_j} (\overline{\rho u_j'' \tilde{k}})
\end{aligned} \tag{3.22}$$

3.3 Modeled Turbulent Kinetic Energy Equation

The turbulent kinetic energy equation (3.22) contains unknown correlations on the right hand side, so these quantities must be modeled. The first term on the right hand side may be expressed as

$$-\overline{u_i'' \frac{\partial p}{\partial x_i}} = -\frac{\partial \overline{u_i'' p}}{\partial x_i} + p \frac{\partial \overline{u_i''}}{\partial x_i} \tag{3.23}$$

The second term on the right hand side of the above equation is equal to zero for incompressible flow and is expected to be small for compressible flow, so it is common practice to neglect it. We now have

$$\begin{aligned}
& \frac{\partial}{\partial t} (\overline{\rho \tilde{k}}) + \frac{\partial}{\partial x_j} (\tilde{u}_j \overline{\rho \tilde{k}}) \\
& = -\frac{\partial}{\partial x_j} (\overline{u_i'' p} + \overline{\rho u_j'' \tilde{k}}) + \overline{u_i'' \frac{\partial \tau_{ij}}{\partial x_j}} - \overline{\rho u_i'' u_j''} \frac{\partial \tilde{u}_i}{\partial x_j}
\end{aligned} \tag{3.24}$$

The first term on the right hand side of equation (3.24) will be modeled using an analogy to equation (3.8). The diffusion coefficient is defined to be $\mu + (\mu_t / \sigma_k)$, where σ_k is a Prandtl number for the diffusion of \tilde{k} .

$$-\frac{\partial}{\partial x_j} (\overline{u_i'' p} + \overline{\rho u_j'' \tilde{k}}) = \frac{\partial}{\partial x_j} \left[\left(\mu + \frac{\mu_t}{\sigma_k} \right) \frac{\partial \tilde{k}}{\partial x_j} \right] \tag{3.25}$$

The third term on the right hand side of equation (3.22) has already effectively been modeled by equation (3.1). The final term to be modeled is therefore the second

term on the right hand side, the dissipation term. This term will first be split into two parts,

$$\overline{u_i'' \frac{\partial \tau_{ij}}{\partial x_j}} = \frac{\partial}{\partial x_j} \left(\overline{u_i'' \tau_{ij}} \right) - \overline{\tau_{ij} \frac{\partial u_i''}{\partial x_j}} \quad (3.26)$$

Applying equation (2.4) yields

$$\begin{aligned} \overline{u_i'' \frac{\partial \tau_{ij}}{\partial x_j}} &= \frac{\partial}{\partial x_j} \left(\overline{\mu u_i'' \frac{\partial \tilde{u}_i}{\partial x_j}} \right) + \frac{\partial}{\partial x_j} \left(\overline{\mu u_i'' \frac{\partial \tilde{u}_j}{\partial x_i}} \right) - \frac{2}{3} \delta_{ij} \frac{\partial}{\partial x_j} \left(\overline{\mu u_i'' \frac{\partial \tilde{u}_k}{\partial x_k}} \right) \\ &+ \frac{\partial}{\partial x_j} \left(\overline{\mu u_i'' \frac{\partial u_i''}{\partial x_j}} \right) + \frac{\partial}{\partial x_j} \left(\overline{\mu u_i'' \frac{\partial u_j''}{\partial x_i}} \right) - \frac{2}{3} \delta_{ij} \frac{\partial}{\partial x_j} \left(\overline{\mu u_i'' \frac{\partial u_k''}{\partial x_k}} \right) \\ &- \mu \frac{\partial u_i''}{\partial x_j} \frac{\partial \tilde{u}_i}{\partial x_j} - \mu \frac{\partial u_i''}{\partial x_j} \frac{\partial \tilde{u}_j}{\partial x_i} + \frac{2}{3} \delta_{ij} \mu \frac{\partial u_i''}{\partial x_j} \frac{\partial \tilde{u}_k}{\partial x_k} \\ &- \mu \frac{\partial u_i''}{\partial x_j} \frac{\partial u_i''}{\partial x_j} - \mu \frac{\partial u_i''}{\partial x_j} \frac{\partial u_j''}{\partial x_i} + \frac{2}{3} \delta_{ij} \mu \frac{\partial u_i''}{\partial x_j} \frac{\partial u_k''}{\partial x_k} \end{aligned} \quad (3.27)$$

It is generally assumed that compressibility does not affect the dissipation rate. For incompressible flow, noting that viscosity fluctuations are equal to zero, the above equation reduces to

$$\begin{aligned} \overline{u_i'' \frac{\partial \tau_{ij}}{\partial x_j}} &= \bar{\mu} \frac{\partial}{\partial x_j} \left(\overline{u_i'' \frac{\partial u_i''}{\partial x_j}} \right) + \bar{\mu} \frac{\partial}{\partial x_j} \left(\overline{u_i'' \frac{\partial u_j''}{\partial x_i}} \right) \\ &- \bar{\mu} \frac{\partial u_i''}{\partial x_j} \frac{\partial u_i''}{\partial x_j} - \bar{\mu} \frac{\partial u_i''}{\partial x_j} \frac{\partial u_j''}{\partial x_i} \end{aligned} \quad (3.28)$$

Assuming homogeneity, the first two terms on the right hand side are equal to zero (since spacial derivatives of averages of fluctuating quantities are equal to zero).

Rearranging the remaining terms, and replacing $\bar{\mu}$ with the equivalent $\bar{\rho} \bar{\nu}$ yields

$$\overline{u_i'' \frac{\partial \tau_{ij}}{\partial x_j}} = -\bar{\rho} \bar{\nu} \left(\frac{\partial u_i''}{\partial x_j} + \frac{\partial u_j''}{\partial x_i} \right) \frac{\partial u_i''}{\partial x_j} \quad (3.29)$$

This is the mean density times the dissipation rate,

$$\overline{u_i'' \frac{\partial \tau_{ij}}{\partial x_j}} = -\bar{\rho} \bar{\epsilon} \quad (3.30)$$

Finally, applying equations (3.1), (3.25), and (3.30) to equation (3.22) yields the modeled turbulent kinetic energy equation:

$$\begin{aligned} \frac{\partial}{\partial t} (\bar{\rho k}) + \frac{\partial}{\partial x_j} (\tilde{u}_j \bar{\rho k}) &= \frac{\partial}{\partial x_j} \left[\left(\mu + \frac{\mu_t}{\sigma_k} \right) \frac{\partial \tilde{k}}{\partial x_j} \right] \\ + \left[\mu_t \left(\frac{\partial \tilde{u}_i}{\partial x_j} + \frac{\partial \tilde{u}_j}{\partial x_i} - \frac{2}{3} \delta_{ij} \frac{\partial \tilde{u}_k}{\partial x_k} \right) - \frac{2}{3} \delta_{ij} \bar{\rho k} \right] \frac{\partial \tilde{u}_i}{\partial x_j} &- \bar{\rho \epsilon} \end{aligned} \quad (3.31)$$

The terms on the left hand side represent the total rate of change and rate of convection of turbulent kinetic energy per unit volume. On the right hand side are the rate of diffusion, rate of production, and rate of dissipation of turbulent kinetic energy per unit volume.

3.4 Modeled Dissipation Rate Equation

An exact equation for the dissipation rate of turbulent kinetic energy may be derived from the momentum equations. This is most commonly carried out by assuming incompressible flow (e.g. Harlow and Nakayama 1968), although it has also been done for compressible flow (El Tahry 1983). An order-of-magnitude analysis of the incompressible equation reveals that two terms are of much greater order of magnitude than the others, even though the difference between these two terms is expected to be small (Launder 1984). This situation makes it extremely difficult to solve the equation numerically. To make matters worse, both terms consist of unmeasurable quantities, so even if they could be computed accurately, it would be impossible to compare the results with test data. Rather than try to model the exact equation, a more heuristic equation is normally used, which mimics the form of the turbulent kinetic energy transport equation. This equation, including the compressible terms,

is (Coakley 1983)

$$\begin{aligned} \frac{\partial}{\partial t} (\bar{\rho}\tilde{\epsilon}) + \frac{\partial}{\partial x_j} (\tilde{u}_j \bar{\rho}\tilde{\epsilon}) &= \frac{\partial}{\partial x_j} \left[\left(\mu + \frac{\mu_t}{\sigma_\epsilon} \right) \frac{\partial \tilde{\epsilon}}{\partial x_j} \right] \\ &+ C_1 \frac{\tilde{\epsilon}}{\bar{k}} \left[\mu_t \left(\frac{\partial \tilde{u}_i}{\partial x_j} + \frac{\partial \tilde{u}_j}{\partial x_i} - \frac{2}{3} \delta_{ij} \frac{\partial \tilde{u}_k}{\partial x_k} \right) - \frac{2}{3} \delta_{ij} \bar{\rho} \bar{k} \right] \frac{\partial \tilde{u}_i}{\partial x_j} - C_2 \bar{\rho} \frac{\tilde{\epsilon}^2}{\bar{k}} \end{aligned} \quad (3.32)$$

C_1 and C_2 are empirically determined constants.



4. WALL FUNCTIONS

4.1 Background

The symbol ϵ represents the dissipation rate of turbulent kinetic energy at the smallest scales, where the turbulence is nearly isotropic. Near walls, where the turbulent Reynolds number is low, the turbulence not isotropic, and the dissipation rate must be modified accordingly.

A number of approaches have been used to generalize the model for wall-bounded flows. Jones and Launder (1972) created a "low-Reynolds-number" form of the $k - \epsilon$ model by adding terms to account for the effect of the wall on the dissipation rate. This approach has been followed by others, the model of Chien (1982) being notably popular. Disadvantages of the low-Reynolds-number models are the additional stiffness of the equations (Viegas and Rubesin 1983) and the need for fine grid resolution near the wall. Also, results from these models are often disappointing when compared to experimental data (Chieng and Launder 1980; Patel, Rodi, and Scheuerer 1985; Bernard 1986).

Another approach is to use the high-Reynolds-number version of the $k - \epsilon$ model away from the wall, and to patch in a different model near the wall. Various models may be used in the wall region, such as mixing length models (Lewis and Pletcher 1986) and one-equation models (Lewis and Pletcher 1986; Rodi 1991). This alleviates

the stiffness problem encountered with the low-Reynolds-number models, and for some flows yields good results. However, since simpler models are used near the wall, the concomitant disadvantages of these models, such as the need to specify a length scale, are encountered. They also require relatively fine grid resolution.

A third approach, the one to be further developed here, is the use of wall functions. Wall functions are based on the idea that the basic structure of turbulent boundary layers has been well established. Before discussing this structure, some definitions are required. In the equations throughout the remainder of the present work, all tildes and overbars are dropped except for those indicating correlations between fluctuating quantities. An appropriate velocity scale for flow in the near-wall region is the friction velocity, defined by

$$u_* \equiv \sqrt{\frac{\tau_w}{\rho_w}} \quad (4.1)$$

where τ_w is the wall shear stress and ρ_w is the density at the wall. Using this velocity scale, a nondimensional velocity and a nondimensional length are defined by

$$u^+ \equiv \frac{u}{u_*} \quad (4.2)$$

and

$$y^+ \equiv \frac{u_* y}{\nu} \quad (4.3)$$

where u is the velocity component parallel to the wall, y is the distance normal to the wall, and ν is the kinematic viscosity. A typical turbulent boundary layer velocity profile, similar to that shown in Anderson, Tannehill, and Pletcher (1984), is shown in Figure 4.1. The equation which describes the velocity profile in the log region is

$$u^+ = \frac{1}{\kappa} \ln(y^+) + B \quad (4.4)$$

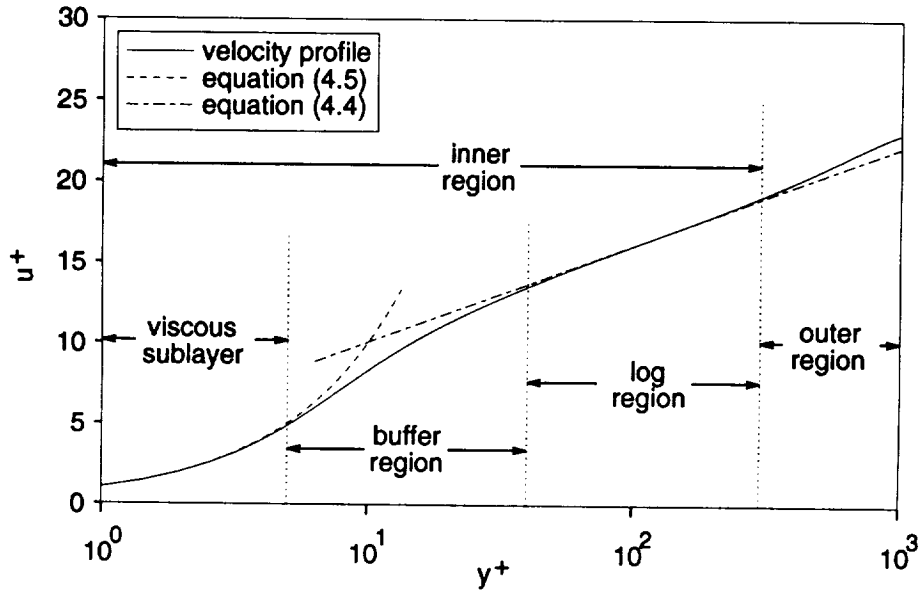


Figure 4.1: Typical turbulent boundary layer velocity profile

where κ is the von Karman constant and B is an additional constant. Values of κ and B have been empirically determined to fall in the ranges 0.40-0.41 and 4.9-5.5 respectively (Cebeci and Smith 1974). In the computations in the present study, the values of 0.41 and 5.0 are used for κ and B . These values were not chosen through tuning of results, but simply because they are a frequently chosen pair, and are, in the words of Coles and Hirst (1969), “satisfactory and non-controversial.” In the viscous sublayer,

$$u^+ = y^+ \quad (4.5)$$

The equations describing the velocity profile in the inner region are collectively called the “law of the wall.”

Knowledge of the structure shown in Figure 4.1 may be applied in such a way that the entire boundary layer need not be resolved numerically. The grid point

adjacent to the wall may be placed well away from the wall, and the shear stress inferred from the velocity at that point.

The use of wall functions has several advantages. The other techniques mentioned above require that the entire boundary layer be resolved. The grid point adjacent to the wall must therefore be located in the viscous sublayer, typically at a y^+ of less than five. For wall functions, the first grid point is normally located in the lower part of the log region, at a y^+ of approximately 40 to 100. Given that the rate at which the grid may stretch away from the wall is limited by most numerical solution schemes, wall functions result in a large saving in the number of grid points and the amount of computer memory required. Viegas and Rubesin (1983) found that approximately half as many grid points were required when using wall functions as compared to low-Reynolds-number models. Since the minimum grid spacing is much larger for the wall function case, a larger time step may be used for a given Courant number (for steady state computations), resulting in further saving in CPU time. The reduced memory and CPU required when using wall functions can be extremely important for the computation of complex three-dimensional flowfields.

One disadvantage of wall functions is that the log equation is not accurate for some flowfields, such as those with regions of separated flow. Also, the standard wall function formulation requires the assumption that the turbulence is in equilibrium at the first grid point away from the wall, which is not always the case. Even with these limitations, wall functions have been shown to yield results comparable, and often superior, to those obtained with low-Reynolds-number models, including computations of some complex flowfields (Chieng and Launder 1980; Viegas and Rubesin 1983; Viegas, Rubesin, and Horstman 1985; Chen and Patel 1987; Avva, Smith, and

Singhal 1990).

Given the advantages and disadvantages of each method described above, wall functions will be pursued in greater detail.

4.2 Detailed Formulation

4.2.1 Introduction

The first step in applying wall functions is to compute the friction velocity and the wall shear stress. The friction velocity is then used to set the boundary conditions for k and ϵ at the grid point adjacent to the wall. Finally, the wall shear stress is used in the computation of the diffusion term in the Navier-Stokes equations at the grid point adjacent to the wall. Development of a general method for applying the wall shear stress to the Navier-Stokes equations in generalized curvilinear coordinates with nonorthogonal grids is the primary contribution of the present work.

4.2.2 Friction velocity

Substituting equations (4.2) and (4.3) into (4.4) and (4.5) gives

$$\frac{u}{u_*} = \frac{1}{\kappa} \ln \left(\frac{u_* y}{\nu} \right) + B \quad (4.6)$$

for the log region and

$$\frac{u}{u_*} = \frac{u_* y}{\nu} \quad (4.7)$$

for the viscous sublayer.

Using u and ν from the previous time step, the friction velocity u_* can be calculated from equation (4.6) or (4.7). If the grid point adjacent to the wall falls in the log region, equation (4.6) is solved using an iterative scheme such as Newton's

method. If the point falls in the viscous sublayer, u_* is calculated directly from equation (4.7). The appropriate equation is determined as follows. Referring to Figure 4.1, equations (4.7) and (4.6) may be seen to intersect at a single value of y^+ , which will be called y_c^+ . Neglecting the buffer region as is often done for engineering calculations (Tennekes and Lumley 1972), y_c^+ delimits the viscous sublayer and the log region. From equations (4.5) and (4.4),

$$y_c^+ = \frac{1}{\kappa} \ln(y_c^+) + B \quad (4.8)$$

This equation is solved for y_c^+ using Newton iteration. It is temporarily assumed that the point in question is in the viscous sublayer. Using the velocity and viscosity from the previous time step, equation (4.7) is solved for u_* , and y^+ is calculated from equation (4.3). If y^+ is less than y_c^+ , the assumption that the point is in the viscous sublayer was correct. Otherwise, the point is actually in the log region, and u_* must be recomputed using equation (4.6). The wall shear stress may then be computed from equation (4.1).

4.2.3 Boundary conditions for k and ϵ

The values of k and ϵ require some special attention near the wall. Both quantities vary rapidly near the wall, and this region of the flowfield is not resolved due to the relatively coarse grid spacing. If k and ϵ can be estimated at the grid point adjacent to the wall, these values may serve as boundary conditions for the turbulence transport equations, and these equations do not have to be integrated all the way to the wall.

For points in the log region, production and dissipation of turbulent kinetic

energy are approximately equal,

$$P = \rho\epsilon \quad (4.9)$$

For a simple two-dimensional boundary layer, letting the y direction be normal to the wall, the production term may be written

$$P = -\overline{\rho u''v''} \frac{du}{dy} \quad (4.10)$$

or

$$P = \tau_t \frac{du}{dy} \quad (4.11)$$

Combining equations (4.10) and (4.11),

$$\tau_t \frac{du}{dy} = \rho\epsilon \quad (4.12)$$

From equations (3.1) and (3.6), the turbulent shear stress may be expressed as

$$\begin{aligned} \tau_t &= \mu_t \frac{du}{dy} \\ &= c_\mu \rho \frac{k^2}{\epsilon} \frac{du}{dy} \end{aligned} \quad (4.13)$$

Solving this equation for ϵ , substituting the result into equation (4.12), and applying the definition of friction velocity (4.1) gives the desired expression for the equilibrium turbulent kinetic energy,

$$k = \frac{u_*^2}{\sqrt{c_\mu}} \quad (4.14)$$

To arrive at an expression for the equilibrium ϵ , equation (4.12) will first be rearranged,

$$\epsilon = \frac{\tau_t}{\rho} \frac{du}{dy} \quad (4.15)$$

From equation (4.6),

$$\frac{du}{dy} = \frac{u_*}{\kappa y} \quad (4.16)$$

Substituting equation (4.16) and the definition of friction velocity (4.1) into equation (4.15) yields the final result

$$\epsilon = \frac{u_*^3}{\kappa y} \quad (4.17)$$

If the grid point adjacent to the wall was found to be in the viscous sublayer, the assumption that production equals dissipation is not valid. A different method must therefore be employed to calculate k and ϵ boundary conditions. The near-wall behavior of k may be examined by expanding fluctuating velocity components in Taylor series normal to the wall (e.g., Launder 1984). Taking the y direction to be normal to the wall,

$$u'' = u''_w + y \left(\frac{\partial u''}{\partial y} \right)_w + \mathcal{O}(y^2) \quad (4.18)$$

$$v'' = v''_w + y \left(\frac{\partial v''}{\partial y} \right)_w + \mathcal{O}(y^2) \quad (4.19)$$

$$w'' = w''_w + y \left(\frac{\partial w''}{\partial y} \right)_w + \mathcal{O}(y^2) \quad (4.20)$$

where the w subscript refers to the value at the wall. From the no-slip condition,

$$u''_w = v''_w = w''_w = 0 \quad (4.21)$$

Very close to the wall, the flow may be considered incompressible for moderate freestream velocities. From the incompressible continuity equation,

$$\left(\frac{\partial v''}{\partial y} \right)_w = 0 \quad (4.22)$$

since $(\partial u''/\partial x)_w$ and $(\partial w''/\partial z)_w$ are equal to zero from the no-slip condition. Substituting equations (4.21) and (4.22) into (4.18)–(4.20),

$$u'' = y \left(\frac{\partial u''}{\partial y} \right)_w + \mathcal{O}(y^2) \quad (4.23)$$

$$v'' = \mathcal{O}(y^2) \quad (4.24)$$

$$w'' = y \left(\frac{\partial w''}{\partial y} \right)_w + \mathcal{O}(y^2) \quad (4.25)$$

Substituting these equations into the definition of k , equation (3.2), yields

$$k = \frac{1}{2} \left\{ y^2 \left[\left(\frac{\partial u''}{\partial y} \right)_w^2 + \left(\frac{\partial w''}{\partial y} \right)_w^2 \right] + \mathcal{O}(y^3) \right\} \quad (4.26)$$

or

$$k \propto y^2 \quad (4.27)$$

near the wall. The value of k is known at $y = y_c^+$ from equation (4.14), and is equal to zero at the wall due to the no-slip condition. Equation (4.27) therefore becomes

$$k = \frac{u_*^2}{\sqrt{c_\mu}} \left(\frac{y^+}{y_c^+} \right)^2 \quad (4.28)$$

This equation must be used with caution. It has been assumed that the asymptotic analysis is applicable throughout the viscous sublayer, and this assumption is questionable. It should be considered an improvement over the assumption that production equals dissipation for points in the viscous sublayer, but is not a definitive expression for the turbulent kinetic energy distribution in this region.

The idea of fitting a parabola to compute k in the viscous sublayer, such as equation (4.28), was proposed by Gorski (1986). Rather than fit the parabola up to y_c^+ as done above, Gorski fixed the value of the turbulent Reynolds number ($Re_t = \sqrt{k}y/\nu = 20$) at the edge of the viscous sublayer, and computed a viscous sublayer thickness based on this value. The assumption that $Re_t = 20$ at the edge of the viscous sublayer is common practice in finite volume wall function formulations, such as that of Chieng and Launder (1980).

An expression for ϵ is still needed for points in the viscous sublayer. Following Rodi (1991), the length scale equation of Norris and Reynolds (1975) will be used,

$$l_\epsilon = \frac{c_l y}{1 + 5.3/Re_t} \quad (4.29)$$

where

$$c_l = \kappa c_\mu^{-3/4} \quad (4.30)$$

Now that k and l_ϵ are known, ϵ is simply

$$\epsilon = \frac{k^{3/2}}{l_\epsilon} \quad (4.31)$$

In summary, if the point adjacent to the wall is in the log region, k and ϵ are computed from equations (4.14) and (4.17). If it is in the viscous sublayer, k and ϵ are computed from equations (4.28) and (4.31).

4.2.4 Application of τ_w to the Navier-Stokes equations

Having computed the friction velocity from equation (4.6) or (4.7), the wall shear stress can be computed from equation (4.1) using the density from the previous time step. The remaining task is to substitute the wall shear stress into the momentum and energy equations.

The law of the wall was originally developed for two-dimensional boundary layers. For three-dimensional boundary layers, if the boundary layer is not highly skewed, the wall shear stress calculated above may be divided vectorially into components in the two coordinate directions parallel to the wall, proportional to the velocity components. If the boundary layer is skewed, a method of approximating the components at the wall, such as extrapolating the velocities, could be employed. Skewness will not be considered in the following development.

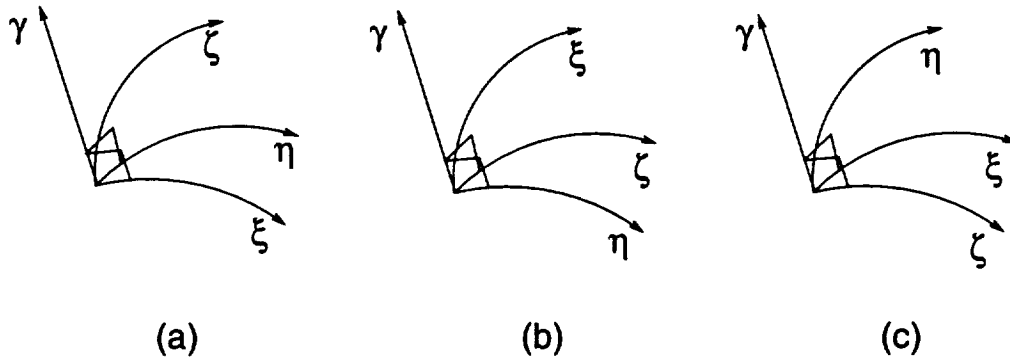


Figure 4.2: Definition of γ coordinate direction

For generalized curvilinear coordinates, the application of the shear stress deduced from the law of the wall to the momentum and energy equations becomes rather complicated. This is due to the fact that the shear stress components in the cartesian coordinate system do not necessarily act parallel to the walls. Another difficulty is encountered when there is no grid line perpendicular to the wall (i.e. the grid is skewed at the wall). The shear stress calculated from the law of the wall acts parallel to the wall, in a plane perpendicular to the wall, but this plane is not necessarily defined by coordinate directions. A new coordinate direction, called “ γ ,” is defined to be perpendicular to the wall. This is shown in Figure 4.2 for the three possible coordinate orientations.

First, metrics must be established in the new coordinate system. The covariant base vectors, which are the base vectors tangent to the coordinate directions, are

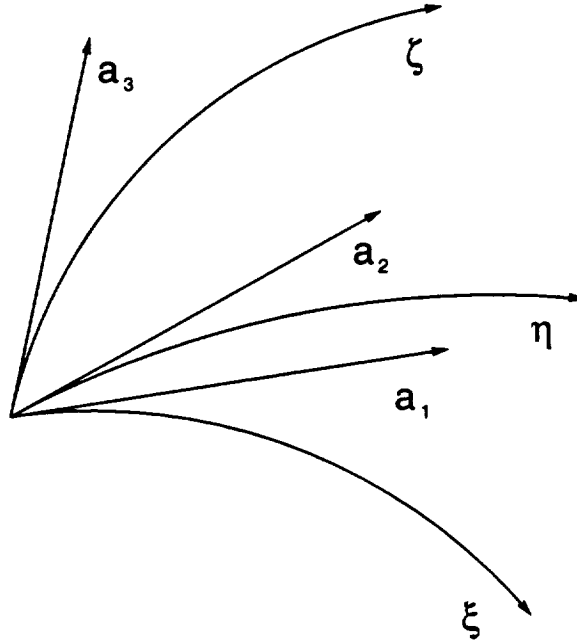


Figure 4.3: Covariant base vectors

given by

$$\mathbf{a}_i = \frac{\partial \mathbf{r}}{\partial \xi^i} \quad (4.32)$$

where \mathbf{r} is a position vector. These are shown in Figure 4.3. \mathbf{a}_1 represents the base vector with components $\frac{\partial x}{\partial \xi}$, $\frac{\partial y}{\partial \xi}$, and $\frac{\partial z}{\partial \xi}$, with similar definitions for the other two coordinate directions. Unit covariant base vectors will also be needed, and are given by

$$\mathbf{e}_i = \frac{\mathbf{a}_i}{|\mathbf{a}_i|} \quad (\text{no } \sum_i) \quad (4.33)$$

The contravariant base vectors are defined by (e.g., Sokolnikoff 1964)

$$\mathbf{a}^1 = \frac{\mathbf{a}_2 \times \mathbf{a}_3}{\mathbf{a}_1 \cdot \mathbf{a}_2 \times \mathbf{a}_3} \quad (4.34)$$

$$\mathbf{a}^2 = \frac{\mathbf{a}_3 \times \mathbf{a}_1}{\mathbf{a}_1 \cdot \mathbf{a}_2 \times \mathbf{a}_3} \quad (4.35)$$

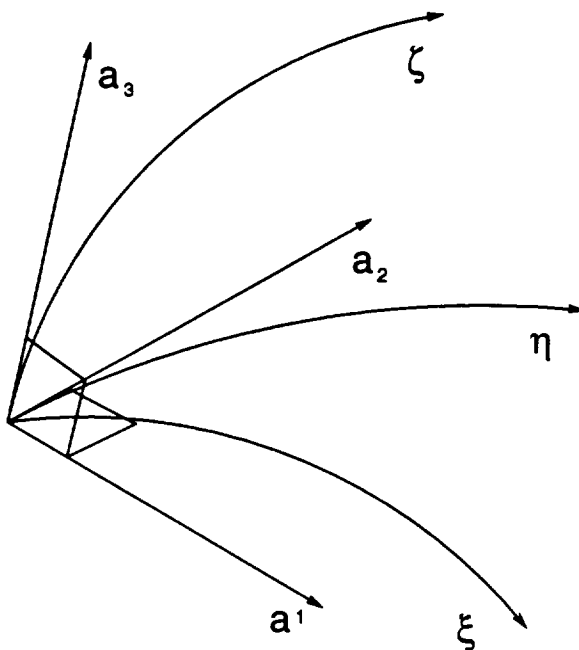


Figure 4.4: Example contravariant base vector

and

$$\mathbf{a}^3 = \frac{\mathbf{a}_1 \times \mathbf{a}_2}{\mathbf{a}_1 \cdot \mathbf{a}_2 \times \mathbf{a}_3} \quad (4.36)$$

An example contravariant base vector is shown in Figure 4.4. It is sometimes useful to express equations (4.34) – (4.36) in vector notation. In (ξ, η, ζ) coordinates, they may be represented as

$$\nabla \xi = \frac{\mathbf{r}_\eta \times \mathbf{r}_\zeta}{\mathbf{r}_\xi \cdot \mathbf{r}_\eta \times \mathbf{r}_\zeta} \quad (4.37)$$

$$\nabla \eta = \frac{\mathbf{r}_\zeta \times \mathbf{r}_\xi}{\mathbf{r}_\xi \cdot \mathbf{r}_\eta \times \mathbf{r}_\zeta} \quad (4.38)$$

and

$$\nabla \zeta = \frac{\mathbf{r}_\xi \times \mathbf{r}_\eta}{\mathbf{r}_\xi \cdot \mathbf{r}_\eta \times \mathbf{r}_\zeta} \quad (4.39)$$

where \mathbf{r} is a position vector, and subscripts indicate partial derivatives. In a computational grid, the denominator of equations (4.34) – (4.39) represents the volume of

the grid cell, or the reciprocal of the Jacobian of the coordinate transformation, J^{-1} .

The γ direction has been defined to be perpendicular to the wall. As an example, refer to Figure 4.2a. In this coordinate system, the γ direction is perpendicular to both the ξ and η directions. From equation (4.39), it may be seen that $\nabla\zeta$ is also perpendicular to the ξ and η directions. Since the covariant γ base vector,

$$\mathbf{a}_\gamma = \left(\frac{\partial x}{\partial \gamma}, \frac{\partial y}{\partial \gamma}, \frac{\partial z}{\partial \gamma} \right) \quad (4.40)$$

is also in the γ direction, $\nabla\zeta$ and \mathbf{a}_γ are proportional to one another. Denoting the proportionality factor as b ,

$$\frac{\partial x}{\partial \gamma} = b \frac{\partial \zeta}{\partial x}, \quad (4.41)$$

$$\frac{\partial y}{\partial \gamma} = b \frac{\partial \zeta}{\partial y}, \quad (4.42)$$

and

$$\frac{\partial z}{\partial \gamma} = b \frac{\partial \zeta}{\partial z}, \quad (4.43)$$

The γ direction is now defined, but magnitudes of the γ metrics still have to be established. In the example coordinate system of Figure 4.2a, an equation may be written analogous to equation (4.39),

$$\nabla\gamma = \frac{\mathbf{r}_\xi \times \mathbf{r}_\eta}{\mathbf{r}_\xi \cdot \mathbf{r}_\eta \times \mathbf{r}_\gamma} \quad (4.44)$$

Recall that the denominator of this equation is equal to J^{-1} . Since the values of the Jacobians will normally be available in (ξ, η, ζ) coordinates, the Jacobians in the (ξ, η, γ) coordinate system will be chosen to be equal to those in the old system. This is simply a convenience, so the computation of new Jacobians is not required. Comparing equations (4.39) and (4.44), it may be seen that by setting the old and

new Jacobians equal, the contravariant base vectors in the γ and ζ directions are also equal,

$$\gamma_x = \zeta_x \quad (4.45)$$

$$\gamma_y = \zeta_y \quad (4.46)$$

and

$$\gamma_z = \zeta_z \quad (4.47)$$

J^{-1} is defined by

$$J^{-1} = \mathbf{a}_1 \cdot \mathbf{a}_2 \times \mathbf{a}_3 \quad (4.48)$$

or in the coordinate system of the present example,

$$J^{-1} = \mathbf{r}_\xi \cdot \mathbf{r}_\eta \times \mathbf{r}_\gamma \quad (4.49)$$

Carrying out the vector operations,

$$J^{-1} = x_\xi(y_\eta z_\gamma - y_\gamma z_\eta) + y_\xi(x_\gamma z_\eta - x_\eta z_\gamma) + z_\xi(x_\eta y_\gamma - x_\gamma y_\eta) \quad (4.50)$$

Substituting equations (4.41), (4.42), and (4.43), and solving for b gives

$$b = \frac{J^{-1}}{x_\xi(y_\eta \zeta_z - \zeta_y z_\eta) + y_\xi(\zeta_x z_\eta - x_\eta \zeta_z) + z_\xi(x_\eta \zeta_y - \zeta_x y_\eta)} \quad (4.51)$$

The metrics x_γ , y_γ , and z_γ may now be calculated from equations (4.41), (4.42), and (4.43). The contravariant base vectors may be calculated from equations (4.34), (4.35), and (4.36). In our present example coordinate system, these are

$$\nabla\xi = \frac{\mathbf{r}_\eta \times \mathbf{r}_\gamma}{\mathbf{r}_\xi \cdot \mathbf{r}_\eta \times \mathbf{r}_\gamma} \quad (4.52)$$

and

$$\nabla\eta = \frac{\mathbf{r}_\gamma \times \mathbf{r}_\xi}{\mathbf{r}_\xi \cdot \mathbf{r}_\eta \times \mathbf{r}_\gamma} \quad (4.53)$$

The calculation of all the metric quantities that are needed for the coordinate transformation is now complete.

Keep in mind that the whole idea of the present procedure is to replace the shear stresses in the Navier-Stokes equations with those from the wall functions. For finite difference schemes, this means that the shear stresses are required at a point between the wall and the point adjacent to the wall (i.e. point $1\frac{1}{2}$). In the absence of a streamwise pressure gradient, the momentum equation evaluated at the wall shows that the normal gradient of the shear stress is zero at the wall. This means that the shear stress at point $1\frac{1}{2}$ is approximately the same as the shear stress at the wall. For cases with streamwise pressure gradients, this is not the case. However, it will be assumed here that the wall function shear stress is applicable at point $1\frac{1}{2}$. This is consistent with the use of the log equation (4.6), which technically is not valid for flows with streamwise pressure gradients. It is common practice to use the log equation for flows with moderate streamwise pressure gradients, since it gives reasonable results for these cases (Launder 1984). Using the pressure gradient from the previous time step, a better approximation for the shear stress at point $1\frac{1}{2}$ could be obtained from the momentum equation if desired.

The next step is to calculate the shear stresses in physical (x, y, z) coordinates (e.g., τ^{xy}) at point $1\frac{1}{2}$ using the equation

$$\tau^{ij} = (\mu + \mu_t) \left(\frac{\partial u_i}{\partial x_j} + \frac{\partial u_j}{\partial x_i} - \frac{2}{3} \delta_{ij} \frac{\partial u_k}{\partial x_k} \right) \quad (4.54)$$

These should be calculated in the same way that they are calculated in the discretized Navier-Stokes equations, i.e. the same averaging procedure should be used to obtain values at point $1\frac{1}{2}$. The stresses are then transformed to the generalized coordinate

system using the standard tensor transformation

$$\check{\tau}^{\alpha\beta} = \frac{\partial\gamma^\alpha}{\partial x^i} \frac{\partial\gamma^\beta}{\partial x^j} \tau^{ij} \quad (4.55)$$

(e.g., Sokolnikoff 1964). Here, the $\check{}$ symbol represents quantities in the generalized coordinate system. For clarity, Greek letters are used for tensor indices in generalized coordinates, and Roman letters are used for physical coordinates. The tensor x^i represents the physical coordinate x , y , or z , and γ^α represents the generalized coordinate ξ , η , or γ .

The stresses $\check{\tau}^{\alpha\beta}$ do not represent physical quantities. In order to obtain the physical components of the shear stresses in the generalized coordinate directions, the following equation (Aris 1962) is employed,

$$\check{\tau}(\alpha\beta) = \sqrt{\frac{\check{g}_{\alpha\alpha}}{\check{g}_{\beta\beta}}} \check{g}_{\beta\gamma} \check{\tau}^{\alpha\gamma} \quad (\text{no } \sum_{\alpha,\beta}) \quad (4.56)$$

where $\check{\tau}(\alpha\beta)$ represents the physical components of the tensor. $\check{g}_{\alpha\beta}$ is the metric tensor,

$$\check{g}_{\alpha\beta} = \frac{\partial x^i}{\partial \gamma^\alpha} \frac{\partial x^i}{\partial \gamma^\beta} \quad (4.57)$$

The physical velocity components in the generalized coordinate directions will also be needed:

$$\check{u}(\alpha) = \check{U}^\alpha \sqrt{\check{g}_{\alpha\alpha}} \quad (\text{no } \sum_\alpha) \quad (4.58)$$

where \check{U}^α represents the contravariant velocity components,

$$\check{U}^\alpha = \frac{\partial\gamma^\alpha}{\partial x^i} u^i \quad (4.59)$$

Capital U is used for the contravariant velocity components and small u is used for the physical velocity components in the physical coordinate directions to be consistent with standard CFD notation.

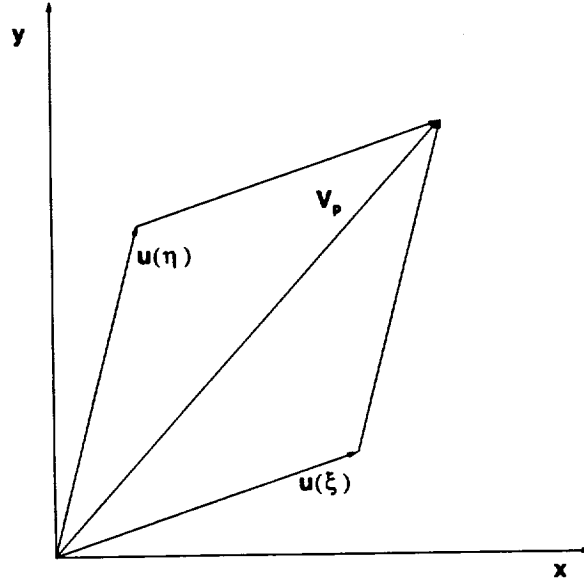


Figure 4.5: Physical velocity components parallel to wall

As mentioned above, 3D boundary layer skewness will not be addressed here. The shear stresses will therefore be scaled with the physical velocity components. In the example coordinate system, the physical velocity component parallel to the wall is given by

$$V_p = \sqrt{[\check{u}(\xi)\mathbf{e}_{\xi_i} + \check{u}(\eta)\mathbf{e}_{\eta_i}]^2} \quad (4.60)$$

Here, \mathbf{e}_{ξ_i} represents the x , y , and z components (corresponding to $i = 1, 2, 3$) of the covariant unit base vector in the ξ direction. Figure 4.5 shows V_p for a two-dimensional coordinate system (A two-dimensional coordinate system was chosen for clarity). Scaling the shear stress components with the velocity components gives

$$\check{\tau}(\xi\gamma) = \frac{\check{u}(\xi)}{V_p} \tau_{[w]} \quad (4.61)$$

and

$$\check{\tau}(\eta\gamma) = \frac{\check{u}(\eta)}{V_p} \check{\tau}_{[w]} \quad (4.62)$$

where $\check{\tau}_{[w]}$ is the wall shear stress from the wall functions. Brackets are used in the notation of $\check{\tau}_{[w]}$ so that w is not confused with a tensor index. The symbol $\check{\tau}$ is used to indicate physical shear stress components which were deduced from the wall function equations, as opposed to those computed from equation (4.56). The physical shear stress tensor computed from equation (4.56) is now modified to reflect the wall function values. In the present example, $\check{\tau}(\xi\gamma)$ and $\check{\tau}(\eta\gamma)$ calculated in equation (4.56) are replaced by the values from equations (4.61) and (4.62).

The above procedure will now be reversed to transform the new physical stresses in the generalized coordinate system to physical stresses in physical coordinates. First, an equation is required to calculate tensor components from physical components, i.e. the inverse of equation (4.56). It is convenient here to work in matrix notation rather than with tensors. In order to express equation (4.56) in matrix notation, matrices will be defined as follows:

$$\mathbf{P} \equiv \begin{bmatrix} \tau(11) & \tau(12) & \tau(13) \\ \tau(21) & \tau(22) & \tau(23) \\ \tau(31) & \tau(32) & \tau(33) \end{bmatrix} \quad (4.63)$$

$$\mathbf{T} \equiv \begin{bmatrix} \tau^{11} & \tau^{12} & \tau^{13} \\ \tau^{21} & \tau^{22} & \tau^{23} \\ \tau^{31} & \tau^{32} & \tau^{33} \end{bmatrix} \quad (4.64)$$

$$\mathbf{G} \equiv \begin{bmatrix} g_{11} & g_{12} & g_{13} \\ g_{21} & g_{22} & g_{23} \\ g_{31} & g_{32} & g_{33} \end{bmatrix} \quad (4.65)$$

$$\mathbf{S} \equiv \begin{bmatrix} \sqrt{g_{11}} & 0 & 0 \\ 0 & \sqrt{g_{22}} & 0 \\ 0 & 0 & \sqrt{g_{33}} \end{bmatrix} \quad (4.66)$$

The \checkmark notation has been dropped, since these definitions hold for any coordinate system. Noting that the matrix \mathbf{G} is symmetric, equation (4.56) may be written in matrix notation as

$$\mathbf{P} = \mathbf{S}\mathbf{T}(\mathbf{S}^{-1}\mathbf{G})^{\mathbf{T}} \quad (4.67)$$

Solving for \mathbf{T} ,

$$\mathbf{T} = \mathbf{S}^{-1}\mathbf{P}[(\mathbf{S}^{-1}\mathbf{G})^{\mathbf{T}}]^{-1} \quad (4.68)$$

In the present example the new stress tensor may be computed from equation (4.68),

$$\check{\check{\mathbf{T}}} = \check{\check{\mathbf{S}}}^{-1}\check{\check{\mathbf{P}}}[(\check{\check{\mathbf{S}}}^{-1}\check{\check{\mathbf{G}}})^{\mathbf{T}}]^{-1} \quad (4.69)$$

where $\check{\check{\mathbf{P}}}$ is

$$\check{\check{\mathbf{P}}} = \begin{bmatrix} \check{\check{\tau}}(11) & \check{\check{\tau}}(12) & \check{\check{\tau}}(13) \\ \check{\check{\tau}}(21) & \check{\check{\tau}}(22) & \check{\check{\tau}}(23) \\ \check{\check{\tau}}(31) & \check{\check{\tau}}(32) & \check{\check{\tau}}(33) \end{bmatrix} \quad (4.70)$$

Note that the stress components from equations (4.61) and (4.62) have been substituted into the $\check{\check{\mathbf{P}}}$ matrix. Finally, returning to tensor notation ($\check{\check{\mathbf{T}}} = \check{\check{\tau}}^{\alpha\beta}$), the new stress tensor must be transformed to physical coordinates,

$$\check{\check{\tau}}^{ij} = \frac{\partial x^i}{\partial \gamma^\alpha} \frac{\partial x^j}{\partial \gamma^\beta} \check{\check{\tau}}^{\alpha\beta} \quad (4.71)$$

$\check{\check{\tau}}^{ij}$ is the new shear stress tensor which is applied to the Navier-Stokes equations. A summary of the procedure described above is shown in Table 4.1.

The application of the new stress tensor to the Navier-Stokes equations is straightforward. The central difference operator $\bar{\delta}\phi = \phi_{j+1/2} - \phi_{j-1/2}$ is typically used for the

Table 4.1: Summary of shear stress transformations

Step	Action	Variable	Equation
1	Compute shear stresses in physical coordinates	τ^{ij}	(4.54)
2	Transform stresses to generalized coordinates	$\check{\tau}^{\alpha\beta}$	(4.55)
3	Compute physical components of stresses in generalized coordinate directions	$\check{\tau}(\alpha\beta)$	(4.55)
4	Split wall shear stress into components parallel to the wall	$\check{\check{\tau}}(\xi\gamma), \check{\check{\tau}}(\eta\gamma)$	(4.61), (4.62)
5	Substitute new shear stress components into physical stress matrix	$\check{\check{\mathbf{P}}}$	(4.70)
6	Compute stresses in generalized coordinates from physical components	$\check{\check{\mathbf{T}}}$	(4.69)
7	Compute new stresses in physical coordinates	$\check{\check{\tau}}^{ij}$	(4.71)

diffusion terms. Letting the j direction be normal to the wall, consider the diffusion term $\frac{\partial \tau_{xy}}{\partial y}$ in the momentum equation (2.18). Here, τ_{xy} represents the total viscous and turbulent shear stress. For unit grid spacing, the discretized diffusion term is

$$\frac{\partial \tau_{xy}}{\partial y} \approx \tau_{xy_{j+1/2}} - \tau_{xy_{j-1/2}} \quad (4.72)$$

At the point adjacent to the wall (i.e. $j = 2$), the value of τ_{xy} from the wall function calculation is substituted for $\tau_{xy_{j-1/2}}$ in the above equation. Other stress terms are handled in a similar manner. When the equations are transformed to generalized coordinates, the shear stresses are still expressed in physical coordinates, so the same method applies. For example, the term analogous to equation (4.72) in generalized coordinates is

$$\frac{\partial}{\partial \xi} (J^{-1} \xi_y \tau_{xy}) \approx (J^{-1} \xi_y \tau_{xy})_{j+1/2} - (J^{-1} \xi_y \tau_{xy})_{j-1/2} \quad (4.73)$$

In this equation, τ_{xy} from the wall function calculation is substituted for $\tau_{xy_{j-1/2}}$, just as in equation (4.72).

5. OTHER TURBULENCE MODELS

5.1 Introduction

In computing wall-bounded turbulent flows, there are many alternatives to the $k - \epsilon$ model with wall functions. Two common approaches are low-Reynolds-number $k - \epsilon$ models and algebraic models. It is therefore desirable to compare their performance to the present wall function formulation. The low-Reynolds-number model of Chien (1982) and the algebraic model of Baldwin and Lomax (1978) are quite popular and well-tested, and have therefore been chosen for comparison with the present formulation.

5.2 Chien Low-Reynolds-Number Model

In the standard high-Reynolds-number $k - \epsilon$ model, dissipation of turbulent kinetic energy is assumed to occur at small scales where the turbulence is nearly isotropic. This is reasonable for free shear flows, but is not the case in the vicinity of walls. In low-Reynolds-number models, terms are typically added to the standard k and ϵ transport equations (Jones and Launder 1972; Chien 1982; Patel, Rodi, and Scheuerer 1984; Mansour, Kim, and Moin 1989; Shih and Mansour 1990; Shih and Hsu 1991; Michelassi and Shih 1991). The magnitudes of these additional terms drop off rapidly away from the wall, resulting in the standard model.

In the Chien model, the dissipation rate is divided into an isotropic part and an anisotropic part. The ϵ which appears in the dissipation rate transport equation is considered to be the isotropic part of the dissipation rate only. Using asymptotic analysis, an expression for dissipation rate near the wall is determined, which is intended to account for anisotropy. This expression is then added to the dissipation rate appearing in the k transport equation. Also, damping functions are applied to the turbulent viscosity and the “destruction of dissipation” term in the ϵ transport equation. The resulting equations are

$$\begin{aligned} \frac{\partial}{\partial t}(\rho k) + \frac{\partial}{\partial x_j}(u_j \rho k) &= Re^{-1} \frac{\partial}{\partial x_j} \left[\left(\mu + \frac{\mu_t}{\sigma_k} \right) \frac{\partial k}{\partial x_j} \right] \\ &+ Re^{-1} \left[\mu_t \left(\frac{\partial u_i}{\partial x_j} + \frac{\partial u_j}{\partial x_i} - \frac{2}{3} \delta_{ij} \frac{\partial u_k}{\partial x_k} \right) \right] \frac{\partial u_i}{\partial x_j} \\ &- \frac{2}{3} \rho k \frac{\partial u_k}{\partial x_k} - \rho \epsilon \boxed{-Re^{-1} \frac{2\nu \rho k}{n^2}} \end{aligned} \quad (5.1)$$

and

$$\begin{aligned} \frac{\partial}{\partial t}(\rho \epsilon) + \frac{\partial}{\partial x_j}(u_j \rho \epsilon) &= Re^{-1} \frac{\partial}{\partial x_j} \left[\left(\mu + \frac{\mu_t}{\sigma_\epsilon} \right) \frac{\partial \epsilon}{\partial x_j} \right] \\ &+ Re^{-1} C_1 \frac{\epsilon}{k} \left[\mu_t \left(\frac{\partial u_i}{\partial x_j} + \frac{\partial u_j}{\partial x_i} - \frac{2}{3} \delta_{ij} \frac{\partial u_k}{\partial x_k} \right) \right] \frac{\partial u_i}{\partial x_j} \\ &- \frac{2}{3} C_1 \delta_{ij} \rho \epsilon \frac{\partial u_k}{\partial x_k} - C_2 f \rho \frac{\epsilon^2}{k} \boxed{-Re^{-1} \frac{2\nu \rho \epsilon}{n^2} e^{-C_4 n^+}} \end{aligned} \quad (5.2)$$

where

$$n^+ = \frac{u_* n}{\nu} \quad (5.3)$$

$$f = 1 \boxed{-\frac{0.4}{1.8} e^{-\left(\frac{k^2}{6\nu\epsilon}\right)^2}} \quad (5.4)$$

$$\mu_t = C_\mu \rho \frac{k^2}{\epsilon} \left(1 \boxed{-e^{-C_3 n^+}} \right) \quad (5.5)$$

Here, n is the normal distance from the wall. The terms in boxes are those which do not appear in the standard high-Reynolds-number $k - \epsilon$ model.

5.3 Baldwin-Lomax Algebraic Model

In the Baldwin-Lomax model, the velocity profiles are divided into an inner region and an outer region. Each region has its own algebraic expression for the turbulent viscosity. The model is given as follows.

$$\mu_t = \begin{cases} (\mu_t)_{\text{inner}} & n \leq n_{\text{crossover}} \\ (\mu_t)_{\text{outer}} & n > n_{\text{crossover}} \end{cases} \quad (5.6)$$

where n is the normal distance from the wall, and $n_{\text{crossover}}$ is the point at which the inner and outer turbulent viscosities are equal.

The inner formulation is given by

$$(\mu_t)_{\text{inner}} = \rho l^2 |\omega| \quad (5.7)$$

where ω is the vorticity. The length scale l is

$$l = \kappa n \left[1 - e^{(-n^+/A^+)} \right] \quad (5.8)$$

where $A^+ = 26$ and n^+ is defined by equation (5.3).

The outer formulation is given by

$$(\mu_t)_{\text{outer}} = K_c C_{cp} \rho F_{\text{wake}} F_{\text{kleb}} \quad (5.9)$$

where the Clauser constant $K_c = 0.02688$, and $C_{cp} = 1.6$. Before defining F_{wake} , an additional function is required,

$$F = \frac{l|\omega|}{\kappa} \quad (5.10)$$

F_{max} is defined as the maximum value of F in the profile, and n_{max} is the normal

distance from the wall at which F_{\max} occurs. F_{wake} is given by

$$F_{\text{wake}} = \text{minimum of } \begin{cases} n_{\max} F_{\max} \\ C_{wk} n_{\max} (u_{\text{dif}})^2 / F_{\max} \end{cases} \quad (5.11)$$

u_{dif} is the difference between the minimum and the maximum magnitude of velocity in the profile, and $C_{wk} = 0.25$.

Finally, F_{kleb} is the Klebanoff intermittancy factor,

$$F_{\text{kleb}} = \left[1 + 5.5 \left(\frac{C_{\text{kleb}} n}{n_{\max}} \right)^6 \right]^{-1} \quad (5.12)$$

where $C_{\text{kleb}} = 0.3$.

6. NUMERICAL METHOD

6.1 Nondimensional Equations

For purposes of nondimensionalization, the following reference quantities are used: velocity, a_∞ ; density, ρ_∞ ; temperature, γT_∞ ; length, L_{ref} ; time, L_{ref}/a_∞ ; and viscosity, μ_∞ . Using boldface type for dimensional quantities, variables in the Navier-Stokes and $k - \epsilon$ equations are nondimensionalized as follows:

$$\begin{aligned} \rho &= \frac{\rho}{\rho_\infty} & u &= \frac{u}{a_\infty} & p &= \frac{p}{\rho_\infty a_\infty^2} & e &= \frac{e}{a_\infty^2} \\ h &= \frac{h}{a_\infty^2} & \mathcal{E} &= \frac{\mathcal{E}}{\rho_\infty a_\infty^2} & H &= \frac{H}{a_\infty^2} & x &= \frac{x}{L_{ref}} \\ t &= \frac{t}{L_{ref}/a_\infty} & T &= \frac{T}{\gamma T_\infty} & \tau &= \frac{\tau}{\mu_\infty a_\infty / L_{ref}} & q &= \frac{q}{\mu_\infty a_\infty^2 / L_{ref}} \\ k &= \frac{k}{a_\infty^2} & \epsilon &= \frac{\epsilon}{a_\infty^3 / L_{ref}} \end{aligned}$$

Applying these definitions to the continuity, momentum, and energy equations (2.16), (2.18), and (2.34), and retaining average symbols only in terms containing fluctuating quantities,

$$\frac{\partial}{\partial t} \rho + \frac{\partial}{\partial x_j} (\rho u_j) = 0 \quad (6.1)$$

$$\frac{\partial}{\partial t} (\rho u_i) + \frac{\partial}{\partial x_j} \left[\rho u_i u_j + \delta_{ij} p - Re^{-1} (\tau_{ij} - Re \overline{\rho u_i'' u_j''}) \right] = 0 \quad (6.2)$$

$$\frac{\partial}{\partial t} (\mathcal{E}) + \frac{\partial}{\partial x_j} \left\{ (\mathcal{E} + p) u_j + Re^{-1} \left[q_j + Re \overline{\rho u_j'' h''} - u_i (\tau_{ij} - Re \overline{\rho u_i'' u_j''}) \right] \right\} = 0 \quad (6.3)$$

where the Reynolds number Re is defined by

$$Re \equiv \frac{\rho_\infty \mathbf{a}_\infty \mathbf{L}_{ref}}{\mu_\infty} \quad (6.4)$$

Similarly, the turbulence transport equations (3.31) and (3.32) become

$$\begin{aligned} \frac{\partial}{\partial t} (\rho k) + \frac{\partial}{\partial x_j} (u_j \rho k) &= Re^{-1} \frac{\partial}{\partial x_j} \left[\left(\mu + \frac{\mu_t}{\sigma_k} \right) \frac{\partial k}{\partial x_j} \right] \\ &+ Re^{-1} \left[\mu_t \left(\frac{\partial u_i}{\partial x_j} + \frac{\partial u_j}{\partial x_i} - \frac{2}{3} \delta_{ij} \frac{\partial u_k}{\partial x_k} \right) \right] \frac{\partial u_i}{\partial x_j} - \frac{2}{3} \rho k \frac{\partial u_k}{\partial x_k} - \rho \epsilon \end{aligned} \quad (6.5)$$

and

$$\begin{aligned} \frac{\partial}{\partial t} (\rho \epsilon) + \frac{\partial}{\partial x_j} (u_j \rho \epsilon) &= Re^{-1} \frac{\partial}{\partial x_j} \left[\left(\mu + \frac{\mu_t}{\sigma_\epsilon} \right) \frac{\partial \epsilon}{\partial x_j} \right] \\ &+ Re^{-1} C_1 \frac{\epsilon}{k} \left[\mu_t \left(\frac{\partial u_i}{\partial x_j} + \frac{\partial u_j}{\partial x_i} - \frac{2}{3} \delta_{ij} \frac{\partial u_k}{\partial x_k} \right) \right] \frac{\partial u_i}{\partial x_j} - \frac{2}{3} C_1 \rho \epsilon \frac{\partial u_k}{\partial x_k} - C_2 \rho \frac{\epsilon^2}{k} \end{aligned} \quad (6.6)$$

The nondimensional turbulent viscosity is given by

$$\nu_t = Re c_\mu \frac{k^2}{\epsilon} \quad (6.7)$$

6.2 Vector Form of Equations

The transport equations for conservation of mass, momentum, and energy are usually written in vector form. Let x , y , and z be the three spatial coordinates and u , v , and w the respective velocity components. The flux vectors are divided into inviscid parts E , F , and G and viscous parts E_v , F_v , and G_v . Equations (6.1), (6.2), and (6.3) may then be written

$$\frac{\partial Q}{\partial t} + \frac{\partial E}{\partial x} + \frac{\partial F}{\partial y} + \frac{\partial G}{\partial z} - Re^{-1} \left(\frac{\partial E_v}{\partial x} + \frac{\partial F_v}{\partial y} + \frac{\partial G_v}{\partial z} \right) = 0 \quad (6.8)$$

where the dependent variable vector is

$$Q = \begin{bmatrix} \rho \\ \rho u \\ \rho v \\ \rho w \\ \mathcal{E} \end{bmatrix} \quad (6.9)$$

and the flux vectors are

$$E = \begin{bmatrix} \rho u \\ \rho u^2 + p \\ \rho uv \\ \rho uw \\ (\mathcal{E} + p)u \end{bmatrix} \quad F = \begin{bmatrix} \rho v \\ \rho uv \\ \rho v^2 + p \\ \rho vw \\ (\mathcal{E} + p)v \end{bmatrix} \quad G = \begin{bmatrix} \rho w \\ \rho uw \\ \rho vw \\ \rho w^2 + p \\ (\mathcal{E} + p)w \end{bmatrix} \quad (6.10)$$

$$E_v = \begin{bmatrix} 0 \\ \tau_{xx} \\ \tau_{xy} \\ \tau_{xz} \\ e_5^v \end{bmatrix} \quad F_v = \begin{bmatrix} 0 \\ \tau_{xy} \\ \tau_{yy} \\ \tau_{yz} \\ f_5^v \end{bmatrix} \quad G_v = \begin{bmatrix} 0 \\ \tau_{xz} \\ \tau_{yz} \\ \tau_{zz} \\ g_5^v \end{bmatrix} \quad (6.11)$$

where, utilizing the Boussinesq approximation (equation (3.1)) and the model for turbulent energy diffusion (equations (3.8) and (3.9)), and employing subscript notation to indicate partial differentiation,

$$\tau_{xx} = (\mu + \mu_t) \left[\frac{4}{3} u_x - \frac{2}{3} (v_y + w_z) \right] - Re \frac{2}{3} \rho k \quad (6.12)$$

$$\tau_{xy} = (\mu + \mu_t) (u_y + v_x) \quad (6.13)$$

$$\tau_{xz} = (\mu + \mu_t) (u_z + w_x) \quad (6.14)$$

$$\tau_{yy} = (\mu + \mu_t) \left[\frac{4}{3} v_y - \frac{2}{3} (u_x + w_z) \right] - Re \frac{2}{3} \rho k \quad (6.15)$$

$$\tau_{yz} = (\mu + \mu_t) (v_z + w_y) \quad (6.16)$$

$$\tau_{zz} = (\mu + \mu_t) \left[\frac{4}{3} w_z - \frac{2}{3} (u_x + v_y) \right] - Re \frac{2}{3} \rho k \quad (6.17)$$

$$e_5^v = u\tau_{xx} + v\tau_{xy} + w\tau_{xz} + \left[\frac{1}{(\gamma - 1)} \left(\frac{\mu}{Pr} + \frac{\mu_t}{Pr_t} \right) (a^2)_x \right] \quad (6.18)$$

$$f_5^v = u\tau_{xy} + v\tau_{yy} + w\tau_{zy} + \left[\frac{1}{(\gamma - 1)} \left(\frac{\mu}{Pr} + \frac{\mu_t}{Pr_t} \right) (a^2)_y \right] \quad (6.19)$$

$$g_5^v = u\tau_{xz} + v\tau_{yz} + w\tau_{zz} + \left[\frac{1}{(\gamma - 1)} \left(\frac{\mu}{Pr} + \frac{\mu_t}{Pr_t} \right) (a^2)_z \right] \quad (6.20)$$

The turbulence transport equations may be put in a similar form,

$$\frac{\partial Q_t}{\partial t} + \frac{\partial E_t}{\partial x} + \frac{\partial F_t}{\partial y} + \frac{\partial G_t}{\partial z} - Re^{-1} \left(\frac{\partial E_{tv}}{\partial x} + \frac{\partial F_{tv}}{\partial y} + \frac{\partial G_{tv}}{\partial z} \right) = H_t \quad (6.21)$$

where the dependent variable vector is

$$Q_t = \begin{bmatrix} \rho k \\ \rho \epsilon \end{bmatrix} \quad (6.22)$$

The flux vectors are

$$E_t = \begin{bmatrix} u\rho k \\ u\rho \epsilon \end{bmatrix} \quad F_t = \begin{bmatrix} v\rho k \\ v\rho \epsilon \end{bmatrix} \quad G_t = \begin{bmatrix} w\rho k \\ w\rho \epsilon \end{bmatrix} \quad (6.23)$$

$$E_{tv} = \begin{bmatrix} \frac{1}{\rho} \left(\mu + \frac{\mu_t}{\sigma_k} \right) \frac{\partial \rho k}{\partial x} \\ \frac{1}{\rho} \left(\mu + \frac{\mu_t}{\sigma_\epsilon} \right) \frac{\partial \rho \epsilon}{\partial x} \end{bmatrix} \quad (6.24)$$

$$F_{tv} = \begin{bmatrix} \frac{1}{\rho} \left(\mu + \frac{\mu_t}{\sigma_k} \right) \frac{\partial \rho k}{\partial y} \\ \frac{1}{\rho} \left(\mu + \frac{\mu_t}{\sigma_\epsilon} \right) \frac{\partial \rho \epsilon}{\partial y} \end{bmatrix} \quad (6.25)$$

$$G_{tv} = \begin{bmatrix} \frac{1}{\rho} \left(\mu + \frac{\mu_t}{\sigma_k} \right) \frac{\partial \rho k}{\partial z} \\ \frac{1}{\rho} \left(\mu + \frac{\mu_t}{\sigma_\epsilon} \right) \frac{\partial \rho \epsilon}{\partial z} \end{bmatrix} \quad (6.26)$$

Before writing the source term H_t in vector form, it is useful to define a symbol for a term which is proportional to the production of turbulent kinetic energy, \mathcal{P} ,

$$\mathcal{P} = Re^{-1} \left[\mu_t \left(\frac{\partial u_i}{\partial x_j} + \frac{\partial u_j}{\partial x_i} - \frac{2}{3} \delta_{ij} \frac{\partial u_k}{\partial x_k} \right) \right] \frac{\partial u_i}{\partial x_j} - \frac{2}{3} \rho k \frac{\partial u_k}{\partial x_k} \quad (6.27)$$

Now H_t may be written as

$$H_t = \begin{bmatrix} \mathcal{P} - \rho \epsilon \\ C_1 \frac{\epsilon}{k} \mathcal{P} - C_2 \frac{\rho \epsilon^2}{k} \end{bmatrix} \quad (6.28)$$

6.3 Coordinate Transformation

The standard transformation to generalized curvilinear coordinates (e.g. Anderson, Tannehill and Pletcher 1984) will be employed here. Transformed time is identical with physical time, and transformed spatial coordinates are general functions of physical spatial coordinates and time,

$$\tau = t \quad (6.29)$$

$$\xi = \xi(x, y, z, t) \quad (6.30)$$

$$\eta = \eta(x, y, z, t) \quad (6.31)$$

$$\zeta = \zeta(x, y, z, t) \quad (6.32)$$

The Jacobian of the transformation is

$$J = \frac{\partial(\xi, \eta, \zeta)}{\partial(x, y, z)} \quad (6.33)$$

Partial derivatives of quantities with respect to physical coordinates may be expressed in terms of transformed coordinates through the chain rule. Letting ϕ represent a

variable to be differentiated,

$$\phi_t = \phi_\tau + \xi_t \phi_\xi + \eta_t \phi_\eta + \zeta_t \phi_\zeta \quad (6.34)$$

$$\phi_x = \xi_x \phi_\xi + \eta_x \phi_\eta + \zeta_x \phi_\zeta \quad (6.35)$$

$$\phi_y = \xi_y \phi_\xi + \eta_y \phi_\eta + \zeta_y \phi_\zeta \quad (6.36)$$

$$\phi_z = \xi_z \phi_\xi + \eta_z \phi_\eta + \zeta_z \phi_\zeta \quad (6.37)$$

Applying the chain rule to equation (6.32), dividing by the Jacobian, and rearranging and cancelling terms results in the transformed set of equations.

$$\frac{\partial \hat{Q}}{\partial \tau} + \frac{\partial \hat{E}}{\partial \xi} + \frac{\partial \hat{F}}{\partial \eta} + \frac{\partial \hat{G}}{\partial \zeta} - Re^{-1} \left(\frac{\partial \hat{E}_v}{\partial \xi} + \frac{\partial \hat{F}_v}{\partial \eta} + \frac{\partial \hat{G}_v}{\partial \zeta} \right) = 0 \quad (6.38)$$

where

$$\hat{Q} = J^{-1} \begin{bmatrix} \rho \\ \rho u \\ \rho v \\ \rho w \\ \mathcal{E} \end{bmatrix} \quad (6.39)$$

$$\hat{E} = J^{-1} \begin{bmatrix} \rho U \\ \rho u U + \xi_x p \\ \rho v U + \xi_y p \\ \rho w U + \xi_z p \\ (\mathcal{E} + p)U - \xi_t p \end{bmatrix} \quad (6.40)$$

$$\hat{F} = J^{-1} \begin{bmatrix} \rho V \\ \rho u V + \eta_x p \\ \rho v V + \eta_y p \\ \rho w V + \eta_z p \\ (\mathcal{E} + p)U - \eta_t p \end{bmatrix} \quad (6.41)$$

$$\hat{G} = J^{-1} \begin{bmatrix} \rho W \\ \rho u W + \zeta_x p \\ \rho v W + \zeta_y p \\ \rho w W + \zeta_z p \\ (\mathcal{E} + p)U - \zeta_t p \end{bmatrix} \quad (6.42)$$

$$\hat{E}_v = J^{-1} \begin{bmatrix} 0 \\ \xi_x \tau_{xx} + \xi_y \tau_{xy} + \xi_z \tau_{xz} \\ \xi_x \tau_{xy} + \xi_y \tau_{yy} + \xi_z \tau_{yz} \\ \xi_x \tau_{xz} + \xi_y \tau_{yz} + \xi_z \tau_{zz} \\ \xi_x e_5^v + \xi_y f_5^v + \xi_z g_5^v \end{bmatrix} \quad (6.43)$$

$$\hat{F}_v = J^{-1} \begin{bmatrix} 0 \\ \eta_x \tau_{xx} + \eta_y \tau_{xy} + \eta_z \tau_{xz} \\ \eta_x \tau_{xy} + \eta_y \tau_{yy} + \eta_z \tau_{yz} \\ \eta_x \tau_{xz} + \eta_y \tau_{yz} + \eta_z \tau_{zz} \\ \eta_x e_5^v + \eta_y f_5^v + \eta_z g_5^v \end{bmatrix} \quad (6.44)$$

$$\hat{G}_v = J^{-1} \begin{bmatrix} 0 \\ \zeta_x \tau_{xx} + \zeta_y \tau_{xy} + \zeta_z \tau_{xz} \\ \zeta_x \tau_{xy} + \zeta_y \tau_{yy} + \zeta_z \tau_{yz} \\ \zeta_x \tau_{xz} + \zeta_y \tau_{yz} + \zeta_z \tau_{zz} \\ \zeta_x e_5^v + \zeta_y f_5^v + \zeta_z g_5^v \end{bmatrix} \quad (6.45)$$

where

$$\begin{aligned} \tau_{xx} = & (\mu + \mu_t) \left\{ \frac{4}{3} (\xi_x u_\xi + \eta_x u_\eta + \zeta_x u_\zeta) \right. \\ & \left. - \frac{2}{3} [(\xi_y v_\xi + \eta_y v_\eta + \zeta_y v_\zeta) + (\xi_z w_\xi + \eta_z w_\eta + \zeta_z w_\zeta)] \right\} \\ & - Re \frac{2}{3} \rho k \end{aligned} \quad (6.46)$$

$$\tau_{xy} = (\mu + \mu_t) [(\xi_y u_\xi + \eta_y u_\eta + \zeta_y u_\zeta) + (\xi_x v_\xi + \eta_x v_\eta + \zeta_x v_\zeta)] \quad (6.47)$$

$$\tau_{xz} = (\mu + \mu_t) [(\xi_z u_\xi + \eta_z u_\eta + \zeta_z u_\zeta) + (\xi_x w_\xi + \eta_x w_\eta + \zeta_x w_\zeta)] \quad (6.48)$$

$$\begin{aligned} \tau_{yy} = & (\mu + \mu_t) \left\{ \frac{4}{3} (\xi_y v_\xi + \eta_y v_\eta + \zeta_y v_\zeta) \right. \\ & \left. - \frac{2}{3} [(\xi_x u_\xi + \eta_x u_\eta + \zeta_x u_\zeta) + (\xi_z w_\xi + \eta_z w_\eta + \zeta_z w_\zeta)] \right\} \\ & - Re \frac{2}{3} \rho k \end{aligned} \quad (6.49)$$

$$\tau_{yz} = (\mu + \mu_t) [(\xi_z v_\xi + \eta_z v_\eta + \zeta_z v_\zeta) + (\xi_y w_\xi + \eta_y w_\eta + \zeta_y w_\zeta)] \quad (6.50)$$

$$\begin{aligned} \tau_{zz} = & (\mu + \mu_t) \left\{ \frac{4}{3} (\xi_z w_\xi + \eta_z w_\eta + \zeta_z w_\zeta) \right. \\ & \left. - \frac{2}{3} [(\xi_x u_\xi + \eta_x u_\eta + \zeta_x u_\zeta) + (\xi_y v_\xi + \eta_y v_\eta + \zeta_y v_\zeta)] \right\} \\ & - Re \frac{2}{3} \rho k \end{aligned} \quad (6.51)$$

$$\begin{aligned} e_5^v = & u \tau_{xx} + v \tau_{xy} + w \tau_{xz} \\ & + \frac{1}{(\gamma - 1)} \left(\frac{\mu}{Pr} + \frac{\mu_t}{Pr_t} \right) \left[\xi_x (a^2)_\xi + \eta_x (a^2)_\eta + \zeta_x (a^2)_\zeta \right] \end{aligned} \quad (6.52)$$

$$f_5^v = u\tau_{xy} + v\tau_{yy} + w\tau_{zy} + \frac{1}{(\gamma-1)} \left(\frac{\mu}{Pr} + \frac{\mu_t}{Pr_t} \right) \left[\xi_y(a^2)_\xi + \eta_y(a^2)_\eta + \zeta_y(a^2)_\zeta \right] \quad (6.53)$$

$$g_5^v = u\tau_{xz} + v\tau_{yz} + w\tau_{zz} + \frac{1}{(\gamma-1)} \left(\frac{\mu}{Pr} + \frac{\mu_t}{Pr_t} \right) \left[\xi_z(a^2)_\xi + \eta_z(a^2)_\eta + \zeta_z(a^2)_\zeta \right] \quad (6.54)$$

and the contravariant velocities are

$$U = \xi_t + \xi_x u + \xi_y v + \xi_z w \quad (6.55)$$

$$V = \eta_t + \eta_x u + \eta_y v + \eta_z w \quad (6.56)$$

$$W = \zeta_t + \zeta_x u + \zeta_y v + \zeta_z w \quad (6.57)$$

The transformed turbulence transport equations are

$$\frac{\partial \hat{Q}_t}{\partial \tau} + \frac{\partial \hat{E}_t}{\partial \xi} + \frac{\partial \hat{F}_t}{\partial \eta} + \frac{\partial \hat{G}_t}{\partial \zeta} - Re^{-1} \left(\frac{\partial \hat{E}_{tv}}{\partial \xi} + \frac{\partial \hat{F}_{tv}}{\partial \eta} + \frac{\partial \hat{G}_{tv}}{\partial \zeta} \right) = \hat{H}_t \quad (6.58)$$

where the dependent variable vector is

$$\hat{Q}_t = J^{-1} \begin{bmatrix} \rho k \\ \rho \epsilon \end{bmatrix} \quad (6.59)$$

The flux vectors are

$$\hat{E}_t = J^{-1} \begin{bmatrix} U \rho k \\ U \rho \epsilon \end{bmatrix} \quad (6.60)$$

$$\hat{F}_t = J^{-1} \begin{bmatrix} V \rho k \\ V \rho \epsilon \end{bmatrix} \quad (6.61)$$

$$\hat{G}_t = J^{-1} \begin{bmatrix} W \rho k \\ W \rho \epsilon \end{bmatrix} \quad (6.62)$$

$$\hat{E}_{tv} = J^{-1} \begin{bmatrix} \frac{1}{\rho} \left(\mu + \frac{\mu_t}{\sigma_k} \right) \left[(\xi_x^2 + \xi_y^2 + \xi_z^2) \frac{\partial \rho k}{\partial \xi} \right. \\ \left. + (\xi_x \eta_x + \xi_y \eta_y + \xi_z \eta_z) \frac{\partial \rho k}{\partial \eta} + (\xi_x \zeta_x + \xi_y \zeta_y + \xi_z \zeta_z) \frac{\partial \rho k}{\partial \zeta} \right] \\ \frac{1}{\rho} \left(\mu + \frac{\mu_t}{\sigma_\epsilon} \right) \left[(\xi_x^2 + \xi_y^2 + \xi_z^2) \frac{\partial \rho \epsilon}{\partial \xi} \right. \\ \left. + (\xi_x \eta_x + \xi_y \eta_y + \xi_z \eta_z) \frac{\partial \rho \epsilon}{\partial \eta} + (\xi_x \zeta_x + \xi_y \zeta_y + \xi_z \zeta_z) \frac{\partial \rho \epsilon}{\partial \zeta} \right] \end{bmatrix} \quad (6.63)$$

$$\hat{F}_{tv} = J^{-1} \begin{bmatrix} \frac{1}{\rho} \left(\mu + \frac{\mu_t}{\sigma_k} \right) \left[(\xi_x \eta_x + \xi_y \eta_y + \xi_z \eta_z) \frac{\partial \rho k}{\partial \xi} \right. \\ \left. + (\eta_x^2 + \eta_y^2 + \eta_z^2) \frac{\partial \rho k}{\partial \eta} + (\eta_x \zeta_x + \eta_y \zeta_y + \eta_z \zeta_z) \frac{\partial \rho k}{\partial \zeta} \right] \\ \frac{1}{\rho} \left(\mu + \frac{\mu_t}{\sigma_\epsilon} \right) \left[(\xi_x \eta_x + \xi_y \eta_y + \xi_z \eta_z) \frac{\partial \rho \epsilon}{\partial \xi} \right. \\ \left. + (\eta_x^2 + \eta_y^2 + \eta_z^2) \frac{\partial \rho \epsilon}{\partial \eta} + (\eta_x \zeta_x + \eta_y \zeta_y + \eta_z \zeta_z) \frac{\partial \rho \epsilon}{\partial \zeta} \right] \end{bmatrix} \quad (6.64)$$

$$\hat{G}_{tv} = J^{-1} \begin{bmatrix} \frac{1}{\rho} \left(\mu + \frac{\mu_t}{\sigma_k} \right) \left[(\xi_x \zeta_x + \xi_y \zeta_y + \xi_z \zeta_z) \frac{\partial \rho k}{\partial \xi} \right. \\ \left. + (\eta_x \zeta_x + \eta_y \zeta_y + \eta_z \zeta_z) \frac{\partial \rho k}{\partial \eta} + (\zeta_x^2 + \zeta_y^2 + \zeta_z^2) \frac{\partial \rho k}{\partial \zeta} \right] \\ \frac{1}{\rho} \left(\mu + \frac{\mu_t}{\sigma_\epsilon} \right) \left[(\xi_x \zeta_x + \xi_y \zeta_y + \xi_z \zeta_z) \frac{\partial \rho \epsilon}{\partial \xi} \right. \\ \left. + (\eta_x \zeta_x + \eta_y \zeta_y + \eta_z \zeta_z) \frac{\partial \rho \epsilon}{\partial \eta} + (\zeta_x^2 + \zeta_y^2 + \zeta_z^2) \frac{\partial \rho \epsilon}{\partial \zeta} \right] \end{bmatrix} \quad (6.65)$$

and the source term vector is

$$\hat{H}_t = J^{-1} \begin{bmatrix} \mathcal{P} - \rho \epsilon \\ C_1 \frac{\xi}{k} \mathcal{P} - C_2 \frac{\rho \epsilon^2}{k} \end{bmatrix} \quad (6.66)$$

6.4 Navier-Stokes Solver

Equation (6.38) will first be semi-discretized in time. Using first order forward differencing,

$$\begin{aligned} \hat{Q}^{n+1} - \hat{Q}^n + \Delta t \left[\frac{\partial \hat{E}^{n+1}}{\partial \xi} + \frac{\partial \hat{F}^{n+1}}{\partial \eta} + \frac{\partial \hat{G}^{n+1}}{\partial \zeta} \right. \\ \left. - Re^{-1} \left(\frac{\partial \hat{E}_v^{n+1}}{\partial \xi} + \frac{\partial \hat{F}_v^{n+1}}{\partial \eta} + \frac{\partial \hat{G}_v^{n+1}}{\partial \zeta} \right) \right] = 0 \end{aligned} \quad (6.67)$$

where superscripts refer to time level. The flux terms must now be linearized. Expanding \hat{E}^{n+1} in a Taylor series,

$$\hat{E}^{n+1} = \hat{E}^n + \Delta t \left(\frac{\partial \hat{E}}{\partial t} \right)^n + \mathcal{O} [(\Delta t)^2] \quad (6.68)$$

Using the chain rule,

$$\left(\frac{\partial \hat{E}}{\partial t} \right)^n = \left(\frac{\partial \hat{E}}{\partial \hat{Q}} \right)^n \left(\frac{\partial \hat{Q}}{\partial t} \right)^n \quad (6.69)$$

Substituting equation (6.69) into (6.68) and discretizing $(\partial \hat{Q} / \partial t)^n$ yields

$$\hat{E}^{n+1} = \hat{E}^n + \hat{A}^n \Delta \hat{Q}^n + \mathcal{O} [(\Delta t)^2] \quad (6.70)$$

where

$$\Delta \hat{Q}^n \equiv \hat{Q}^{n+1} - \hat{Q}^n \quad (6.71)$$

and

$$\hat{A}^n \equiv \left(\frac{\partial \hat{E}}{\partial \hat{Q}} \right)^n \quad (6.72)$$

Jacobian matrices may also be defined for the other inviscid fluxes, $\hat{B}^n \equiv (\partial \hat{F} / \partial \hat{Q})^n$ and $\hat{C}^n \equiv (\partial \hat{G} / \partial \hat{Q})^n$, and similarly for the viscous fluxes. Analytical expressions for the inviscid and viscous flux Jacobians are given in Appendix A.

Applying equation (6.70) to equation (6.67) results in the delta form of the equation,

$$\begin{aligned} & \left\{ I + \Delta t \left[(\partial_\xi \hat{A}^n + \partial_\eta \hat{B}^n + \partial_\zeta \hat{C}^n) - Re^{-1} (\partial_\xi \hat{A}_v^n + \partial_\eta \hat{B}_v^n + \partial_\zeta \hat{C}_v^n) \right] \right\} \Delta \hat{Q} \\ & = -\Delta t \left[(\partial_\xi \hat{E}^n + \partial_\eta \hat{F}^n + \partial_\zeta \hat{G}^n) - Re^{-1} (\partial_\xi \hat{E}_v^n + \partial_\eta \hat{F}_v^n + \partial_\zeta \hat{G}_v^n) \right] \end{aligned} \quad (6.73)$$

where operator notation is now being used for the partial derivatives. Equation (6.73) is solved using an implicit, partially flux-split, two-factor approximate factorization algorithm (Ying et al. 1986). In the original algorithm, all cross-derivative terms

were neglected, and viscous terms were retained only in the direction normal to the wall (thin-layer assumption). Here, viscous terms are retained in all three directions, with all cross-derivative terms neglected. In the flux-split direction (ξ), the viscous terms cannot be linearized if a tri-diagonal solver is to be employed, so they are included only on the right hand side.

The flux vector splitting method of Steger and Warming (1981) is used for convection terms in the ξ direction. The ξ direction inviscid Jacobian \hat{A} is therefore split as follows,

$$\hat{A} = \hat{A}^+ + \hat{A}^- \quad (6.74)$$

where

$$\hat{A}^+ = \hat{T} \hat{\Lambda}^+ \hat{T}^{-1} \quad (6.75)$$

and

$$\hat{A}^- = \hat{T} \hat{\Lambda}^- \hat{T}^{-1} \quad (6.76)$$

$\hat{\Lambda}^+$ is a diagonal matrix containing the positive eigenvalues of \hat{A}_i , and $\hat{\Lambda}^-$ contains the negative eigenvalues. The columns of \hat{T} are the right eigenvectors of \hat{A}_i .

Substituting difference operators, adding smoothing, and applying approximate factorization to equation (6.73),

$$\begin{aligned} & \left\{ I + \Delta t \left[\nabla_{\xi} (\hat{A}^+)^n + \delta_{\zeta} \hat{C}^n - Re^{-1} \bar{\delta}_{\zeta} \hat{C}_v^n - \mathcal{D}_{\text{imp}\zeta} \right] \right\} \\ \times & \left\{ I + \Delta t \left[\Delta_{\xi} (\hat{A}^-)^n + \delta_{\eta} \hat{B}^n - Re^{-1} \bar{\delta}_{\eta} \hat{B}_v^n - \mathcal{D}_{\text{imp}\eta} \right] \right\} \Delta \hat{Q} \\ = & \Delta t \left[\nabla_{\xi} (\hat{E}^+)^n + \Delta_{\xi} (\hat{E}^-)^n + \delta_{\eta} \hat{F}^n + \delta_{\zeta} \hat{G}^n \right. \\ & \left. - Re^{-1} (\bar{\delta}_{\xi} \hat{E}_v^n + \bar{\delta}_{\eta} \hat{F}_v^n + \bar{\delta}_{\zeta} \hat{G}_v^n) - (\mathcal{D}_{\text{exp}\eta} + \mathcal{D}_{\text{exp}\zeta}) \hat{Q}^n \right] \quad (6.77) \end{aligned}$$

The difference operators are defined by

$$\nabla_{\xi} \phi \equiv \phi_j - \phi_{j-1}$$

$$\begin{aligned}
\Delta_\zeta \phi &\equiv \phi_{j+1} - \phi_j \\
\delta_\zeta \phi &\equiv \frac{1}{2}(\phi_{j+1} - \phi_{j-1}) \\
\bar{\delta}_\zeta \phi &\equiv \phi_{j+1/2} - \phi_{j-1/2}
\end{aligned} \tag{6.78}$$

Similar definitions hold for the other two coordinate directions. Smoothing is required for the central-differenced directions to ensure stability. The smoothing operators are given by

$$\mathcal{D}_{\text{imp}\zeta} = J^{-1} \left[\epsilon_2 \bar{\delta}_\zeta s_\zeta \beta \bar{\delta}_\zeta + 2.5 \epsilon_4 \bar{\delta}_\zeta \left(\frac{s_\zeta}{1 + \beta} \right) \bar{\delta}_\zeta \right] J \tag{6.79}$$

$$\mathcal{D}_{\text{exp}\zeta} = J^{-1} \left[\epsilon_2 \bar{\delta}_\zeta s_\zeta \beta \bar{\delta}_\zeta + \epsilon_4 \bar{\delta}_\zeta \left(\frac{s_\zeta}{1 + \beta} \right) \bar{\delta}_\zeta^3 \right] J \tag{6.80}$$

where

$$\beta = \frac{|\bar{\delta}^2 p|}{\left| \left(1 + \frac{\bar{\delta}^2}{4} \right) p \right|} \tag{6.81}$$

ϵ_2 and ϵ_4 are the second and fourth order smoothing coefficients, and s_ζ is the spectral radius of the inviscid flux Jacobian matrix. The factor of 2.5 in the implicit smoothing operator is included to ensure stability, given the fourth order explicit smoothing. The β function is designed to switch from fourth order to second order smoothing in regions of rapid spatial variation in pressure, such as at a shock wave. The spectral radius scaling is included to emulate the numerical dissipation inherent in upwind difference schemes (Pulliam 1985). The η direction smoothing operators are similar to equations (6.79) and (6.80), with all occurrences of the symbol ζ replaced by η .

6.5 $k - \epsilon$ Solver

The $k - \epsilon$ equations are solved uncoupled from the Navier-Stokes equations. The linearized equations are simpler in form than the Navier-Stokes equations because

they are coupled only through the source terms if the functional dependence of μ_t on k and ϵ is neglected in the viscous terms. Flux Jacobians for the convection terms are simply diagonal matrices containing the contravariant velocities. The linearized equations in delta form are

$$\begin{aligned}
& \{I [1 + \Delta t (\partial_\xi U + \partial_\eta V + \partial_\zeta W)] \\
& - \Delta t Re^{-1} [\partial_\xi (J^{-1} \mathcal{N} \beta_1 \partial_\xi J) + \partial_\eta (J^{-1} \mathcal{N} \beta_4 \partial_\eta J) + \partial_\zeta (J^{-1} \mathcal{N} \beta_6 \partial_\zeta J)] \\
& - \Delta t \hat{D}_t^n \} \Delta \hat{Q}_t = -\Delta t [(\partial_\xi \hat{E}_t^n + \partial_\eta \hat{F}_t^n + \partial_\zeta \hat{G}_t^n) \\
& - Re^{-1} (\partial_\xi \hat{E}_{tv}^n + \partial_\eta \hat{F}_{tv}^n + \partial_\zeta \hat{G}_{tv}^n) - \hat{H}_t^n] \tag{6.82}
\end{aligned}$$

where

$$\mathcal{N} = \begin{bmatrix} \frac{1}{\rho} \left(\mu + \frac{\mu_t}{\sigma_k} \right) & 0 \\ 0 & \frac{1}{\rho} \left(\mu + \frac{\mu_t}{\sigma_\epsilon} \right) \end{bmatrix} \tag{6.83}$$

and

$$\beta_1 = \xi_x^2 + \xi_y^2 + \xi_z^2 \tag{6.84}$$

$$\beta_4 = \eta_x^2 + \eta_y^2 + \eta_z^2 \tag{6.85}$$

$$\beta_6 = \zeta_x^2 + \zeta_y^2 + \zeta_z^2 \tag{6.86}$$

An analytical expression for \hat{D}_t^n , the turbulent source term Jacobian, is given in Appendix A.

Equation (6.82) is solved using a conventional three-factor approximate factorization scheme with flux vector splitting and first-order differences for the convection terms in all three directions. Central differences are used for all diffusion terms. Several methods of handling the source terms are available. Here, they have been placed in a single factor, since this method is both simple to implement and is also

computationally efficient (Shih and Chyu 1991). The resulting equation is

$$\begin{aligned}
& \left\{ I \left[1 + \Delta t \left(\nabla_{\xi} U^+ + \Delta_{\xi} U^- \right)^n \right] - \Delta t Re^{-1} \left[\bar{\delta}_{\xi} \left(J^{-1} \mathcal{N} \beta_1 \bar{\delta}_{\xi} J \right) \right] \right\} \\
& \times \left\{ I \left[1 + \Delta t \left(\nabla_{\eta} V^+ + \Delta_{\eta} V^- \right)^n \right] - \Delta t Re^{-1} \left[\bar{\delta}_{\eta} \left(J^{-1} \mathcal{N} \beta_4 \bar{\delta}_{\eta} J \right) \right] \right\} \\
& \times \left\{ I \left[1 + \Delta t \left(\nabla_{\zeta} W^+ + \Delta_{\zeta} W^- \right)^n \right] - \Delta t Re^{-1} \left[\bar{\delta}_{\zeta} \left(J^{-1} \mathcal{N} \beta_6 \bar{\delta}_{\zeta} J \right) \right] \right\} \\
& - \Delta t \hat{D}_t^n \} \Delta \hat{Q}_t \\
& = -\Delta t \left\{ \left[\nabla_{\xi} \left(\hat{E}_t^+ \right)^n + \Delta_{\xi} \left(\hat{E}_t^- \right)^n + \nabla_{\eta} \left(\hat{F}_t^+ \right)^n + \Delta_{\eta} \left(\hat{F}_t^- \right)^n \right. \right. \\
& \left. \left. + \nabla_{\zeta} \left(\hat{G}_t^+ \right)^n + \Delta_{\zeta} \left(\hat{G}_t^- \right)^n \right] - Re^{-1} \left(\bar{\delta}_{\xi} \hat{E}_{tv}^n + \bar{\delta}_{\eta} \hat{F}_{tv}^n + \bar{\delta}_{\zeta} \hat{G}_{tv}^n \right) - \hat{H}_t^n \right\} \quad (6.87)
\end{aligned}$$

The ξ and η direction factors require solution of uncoupled equations, since there is no source term Jacobian present. A specialized solver was therefore written for banded tridiagonal matrices to enhance computation speed. In the ζ direction, a block solver is required due to the source terms. Since two-by-two blocks may be inverted algebraically, a second specialized solver was written for the ζ direction. Details of both of these solvers are given in Appendix B.

An additional consideration in the solution of these equations is the possibility of obtaining negative values for k and ϵ . Negative values are physically impossible, but are admitted by the modeled transport equations. Lower limiters are therefore used for both equations. After each step, any values of ρk or $\rho \epsilon$ that are below the specified limit are bumped up to that limit. The freestream values of ρk and $\rho \epsilon$ are used for the limiters, since the physical (as opposed to numerical) values are not expected to fall below those in the freestream. One run was started from scratch (all dependent variables set to freestream values) with the limiters turned off, and it was unstable. Addition of the limiters solved the problem. After the solution had partly converged, the limiters were again turned off, and the solution remained stable. The

starting transient had caused the unphysical values in the first case, and once the solution settled down, the limiters were unnecessary.

7. RESULTS

7.1 Introduction

A formulation designed for general geometries and skewed grids must also work on simple geometries and orthogonal grids. The ubiquitous flat plate has therefore been chosen for the first set of test cases. First, turbulent flow over a semi-infinite flat plate was computed on an orthogonal grid. The next step was to verify that the formulation is effective when the grid is skewed at the wall, so the same flat plate was solved with a skewed grid.

The tensor transformations in the present formulation contain functions of all of the metrics. When any of the generalized coordinate directions are orthogonal to physical coordinate directions, some of the metrics will be identically equal to zero. One final flat plate test case was run with the entire domain at a thirty degree angle with the physical coordinate system (at zero angle of attack) to bring additional metrics into play and further test the method.

One additional flat plate test case was run to verify the coding of the Chien (1982) low-Reynolds-number model.

After having verified the present formulation for flat surfaces, the next step was to solve a well-behaved (non-separated) flow over a curved surface. Ramaprian, Patel, and Choi (1978, 1980) took measurements of the turbulent flowfield around a

body of revolution at both zero and fifteen degree angles of attack. The zero degree (axisymmetric) flowfield was computed using the present wall function formulation as well as the Chien (1982) low-Reynolds-number model and the Baldwin-Lomax (1978) algebraic model, and the results compared to the measurements. Each computation was carried out using grids with three different wall spacings to determine the grid sensitivity of each model.

Finally, the present wall function formulation was tested on a complex three-dimensional flowfield. Separated flow over a prolate spheroid at ten degrees angle of attack was computed, and the results compared to the measurements of Kreplin, Vollmers, and Meier (1982).

7.2 Flat plate

The first test case is the computation of incompressible, turbulent flow over a semi-infinite flat plate with zero pressure gradient. The freestream Mach number was set to 0.2 to minimize compressibility effects without getting too close to the incompressible limit of the solver. The Reynolds number based on freestream velocity was 1×10^6 at the upstream boundary, and 8×10^6 at the outflow boundary. The reference length was defined such that the distance from the virtual origin of the boundary layer to the upstream boundary was one unit of length. All lengths were normalized by this distance.

The streamwise and normal coordinate directions are x and z in physical coordinates and η and ζ in transformed coordinates. Wall functions are expected to give the most accurate results when the grid point adjacent to the wall falls in the log region. The distance from the wall to the grid point adjacent to the wall, which will

be referred to as the “wall spacing,” was chosen to equal 0.0035 (nondimensionalized by the reference length described above) so that $\Delta z_w^+ \approx 140$, which is well into the log region. Δz_w^+ is the wall spacing in wall coordinates. The domain extended from 1 to 8 in the streamwise direction, and 0 to 1.5 in the normal direction. The location of the outer edge was chosen to exceed ten times the estimated boundary layer thickness at the downstream boundary. The 101×61 (streamwise \times normal) orthogonal grid is shown in Figure 7.1.

An upstream streamwise velocity profile was specified using the law of the wake (Coles 1956),

$$u^+ = \frac{1}{\kappa} \ln(y^+) + B + \frac{\Pi}{\kappa} W\left(\frac{y}{\delta}\right) \quad (7.1)$$

where

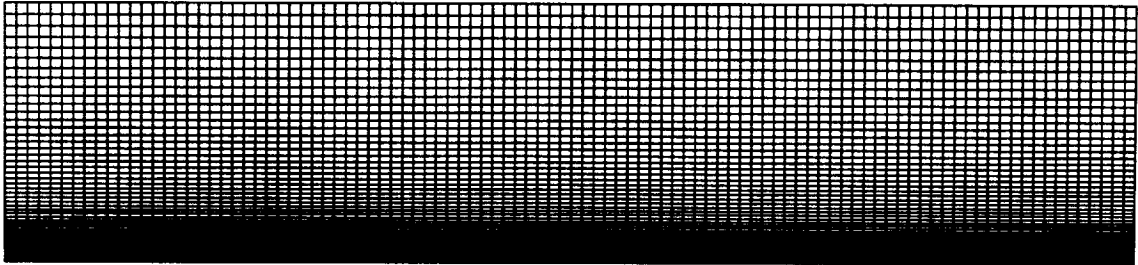
$$W\left(\frac{y}{\delta}\right) \approx 2 \sin^2\left(\frac{\pi y}{2\delta}\right) \quad (7.2)$$

Π is a function of the streamwise pressure gradient, and is approximately equal to 0.5 for pressure gradients of zero. The boundary layer thickness, δ , was estimated from the equation (White 1974)

$$\frac{\delta}{x} \approx 0.37 Re_x^{-1/5} \quad (7.3)$$

At the inflow boundary, the normal velocity component was set to zero, the density was fixed at the freestream value, and the pressures were set by extrapolation ($p_{\eta=1} = p_{\eta=2}$). At the outflow boundary, pressure was fixed at the freestream value, and density and both components of momentum were extrapolated. At the outer edge, density, both components of momentum, and pressure were extrapolated. At the wall, velocities were set to zero, and density and pressure were extrapolated.

The upstream turbulence quantities were more difficult to estimate. A detailed



(a) Complete grid



(b) Close-up of upstream boundary

Figure 7.1: Orthogonal flat plate grid

turbulent kinetic energy profile was measured for incompressible flow over a flat plate with zero streamwise pressure gradient by Klebanoff (1955), but at a Reynolds number of 4.2×10^6 . These data were used to estimate the distribution at the present $Re = 1 \times 10^6$.

The friction coefficient was first calculated using the equation (White 1974)

$$C_f \approx \frac{0.455}{\ln^2(0.06Re_x)} \quad (7.4)$$

Combining the definition of friction velocity, equation (4.1), and the definition of friction coefficient,

$$C_f = \frac{\tau_w}{\frac{1}{2}\rho_\infty u_\infty^2} \quad (7.5)$$

the friction velocity can be expressed as a function of friction coefficient,

$$u_* = \sqrt{\frac{\frac{1}{2}\rho_\infty u_\infty^2 C_f}{\rho_w}} \quad (7.6)$$

Since the grid spacing at the wall was chosen such that the first grid point away from the wall was in the log region, k at that point was calculated from equation (4.14).

The next step was to interpolate the Klebanoff k distribution onto the present grid using a cubic spline (Hornbeck 1975). As was expected, the value of k at the point adjacent to the wall did not match the value calculated from equation (4.14). The whole k distribution was multiplied by the ratio of the two values to force the correct value at the given point. Finally, freestream values were cut off at $k/U_\infty^2 = 0.0002$, Klebanoff's approximate freestream k .

The upstream ϵ distribution was estimated using a method described by Launder et al. (1972). The ratio of turbulent shear stress to turbulent kinetic energy was estimated to equal the constant 0.3. Since the k distribution was estimated above,

the turbulent shear stress distribution was also “known.” Finally, the ϵ distribution was computed from equation (4.13).

At the outflow boundary and the outer edge, k and ϵ were extrapolated. Values of k or ϵ are not required at the wall when using wall functions.

The friction velocity was computed at each point along the plate from either equation (4.6) or (4.7). Since the friction coefficient is easily deduced from the friction velocity, comparison with experimental friction coefficients is a good check on the effectiveness of a wall function formulation. The friction coefficient distribution for incompressible turbulent flow over a flat plate with zero pressure gradient is well established. An accurate and well-tested equation for the friction coefficient distribution is given by (White 1974)

$$Re_x = \frac{1}{12}\lambda^4 + \frac{e^{\kappa B}}{\kappa^3} \left[e^Z (Z^2 - 4Z + 6) - 6 - 2Z - \frac{Z^4}{12} - \frac{Z^5}{20} \right] \quad (7.7)$$

where

$$\lambda = \sqrt{2/C_f} \quad (7.8)$$

and

$$Z = \kappa\lambda \quad (7.9)$$

The computed results are within $1\frac{1}{2}\%$ of the values from the equation. The computed friction coefficients are compared with equation (7.7) in Figure 7.2. The computed results are within $1\frac{1}{2}\%$ of the values from the equation.

A sample velocity profile is compared with test data in Figure 7.3, where δ is the boundary layer thickness and U_{inf} is the freestream velocity. The measurements were taken by Klebanoff (1955) at a Reynolds number of 4.2×10^6 based on freestream velocity and distance from the virtual origin of the plate. The computed profile

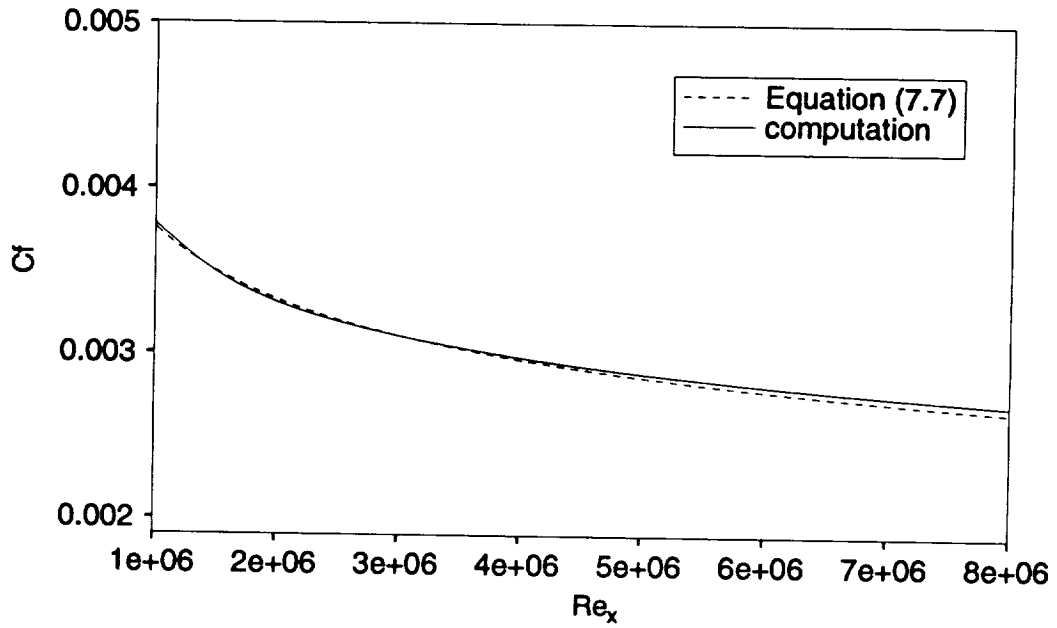


Figure 7.2: Friction coefficient, flat plate, orthogonal grid

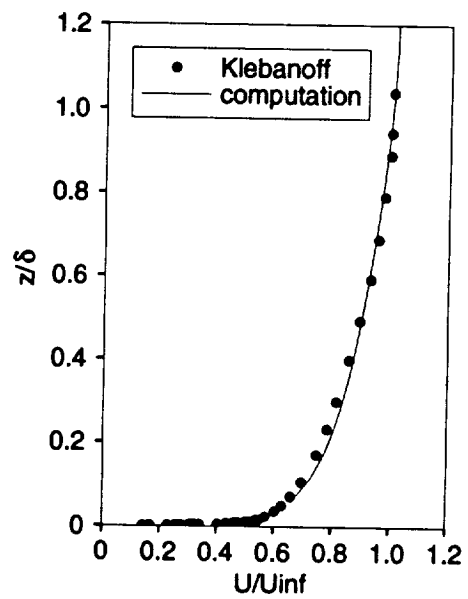


Figure 7.3: Velocity profile, flat plate, orthogonal grid

is at the same Reynolds number assuming that the virtual origin is at $x = 0$. The boundary layer thickness for the test data was taken to equal the “nominal thickness” of three inches quoted in Klebanoff’s paper. For the computation, the boundary layer thickness was taken at the point at which the velocity reached 99% of the freestream velocity.

At the grid point adjacent to the wall, the computed velocity is slightly higher than the test data. Since this grid point falls in the log region, the computed friction coefficient must also be larger than the value corresponding to the test data. It would be more accurate to compare velocity profiles at the same momentum thickness Reynolds number rather than Reynolds number based on distance from the virtual origin of the plate, since it is difficult to locate the virtual origin precisely. For the present computation, however, it is also difficult to compute the momentum thickness accurately due to the coarse grid spacing at the wall. Since the boundary layer is not resolved near the wall, the numerical integration required to compute the momentum thickness would also be inaccurate.

7.2.1 Skewed grid

In the present wall function formulation, a new coordinate direction is defined normal to the wall, and physical shear stresses are computed using this new direction. A simple test case with a grid that is nonorthogonal at the wall was desired to check this part of the procedure. A case similar to that computed above was chosen, but using a grid which is skewed near the wall. The grid lines parallel to the plate (constant ζ) are identical to those in the orthogonal grid. The grid is orthogonal to the plate at the upstream boundary. Moving downstream, the grid lines gradually become

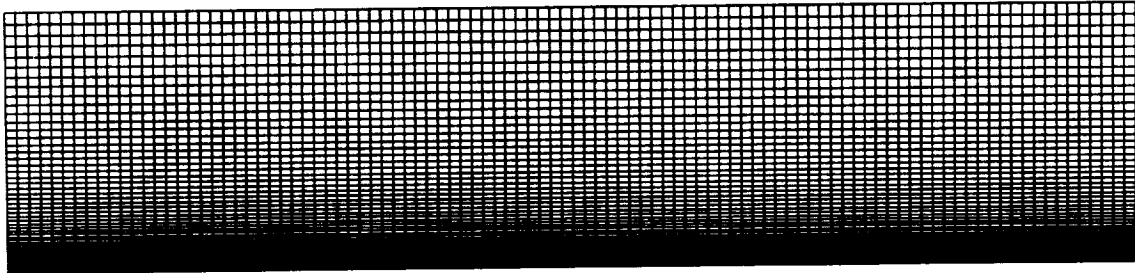
more and more skewed, until they reach an angle of sixty degrees with respect to the plate. They then remain at this angle for the rest of the domain. This configuration was chosen for two reasons. First, the upstream boundary definition was identical to that for the orthogonal grid case, and it was therefore easy to implement. Also, some of the metrics (e.g. $\partial\zeta/\partial x$) are changing along the transformed coordinate directions, so additional terms are brought into play in the computation. The grid is shown in Figure 7.4. The freestream conditions and boundary conditions are identical to those for the orthogonal grid case.

The resulting friction coefficient distribution is shown in Figure 7.5. It is identical to that for the orthogonal grid, verifying that the shear stresses are being computed correctly in the new coordinate system.

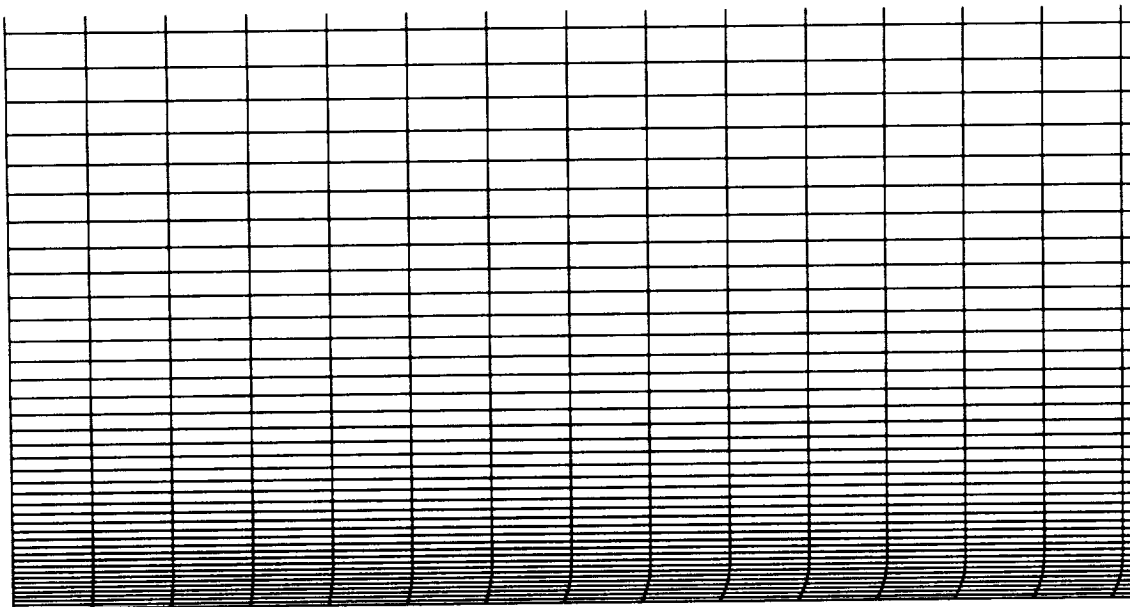
The velocity profile at a Reynolds number of 4.2×10^6 is shown in Figure 7.6. It, too, is identical to that in the orthogonal grid test case (Figure 7.3).

7.2.2 Angled domain

Since the geometry of the flat plate test cases is simple, many metric terms used in the transformation of the shear stresses are identically equal to zero (for example $\partial\gamma/\partial x$). The flat plate test case with the orthogonal grid was therefore repeated, but the entire domain was angled thirty degrees with respect to the physical coordinates. The plate was still at zero degrees angle of attack. In this computation, none of the physical coordinates were orthogonal to the transformed coordinates, so it was a more general test of the wall function formulation. This case was run at the same freestream conditions as the previous cases. The resulting friction coefficients are shown in Figure 7.7. The angled domain has not affected the results, verifying that

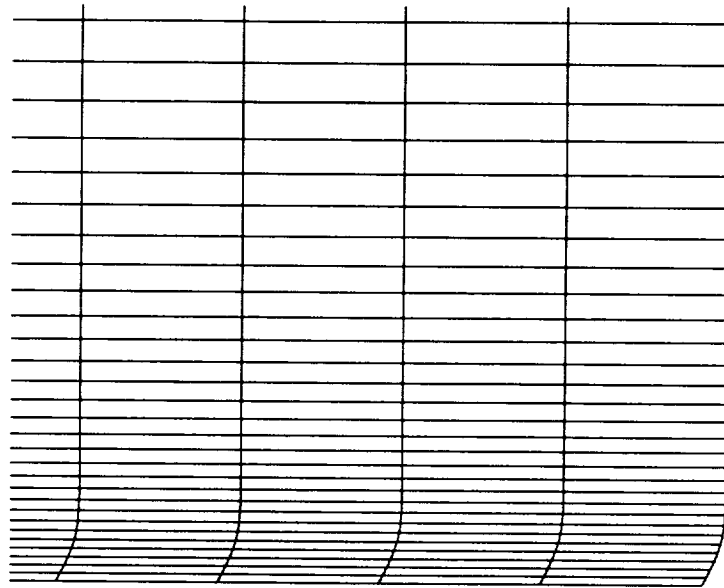


(a) Complete grid



(b) Close-up of region of changing skewness

Figure 7.4: Skewed flat plate grid



(c) Close-up of downstream boundary

Figure 7.4 (Continued)

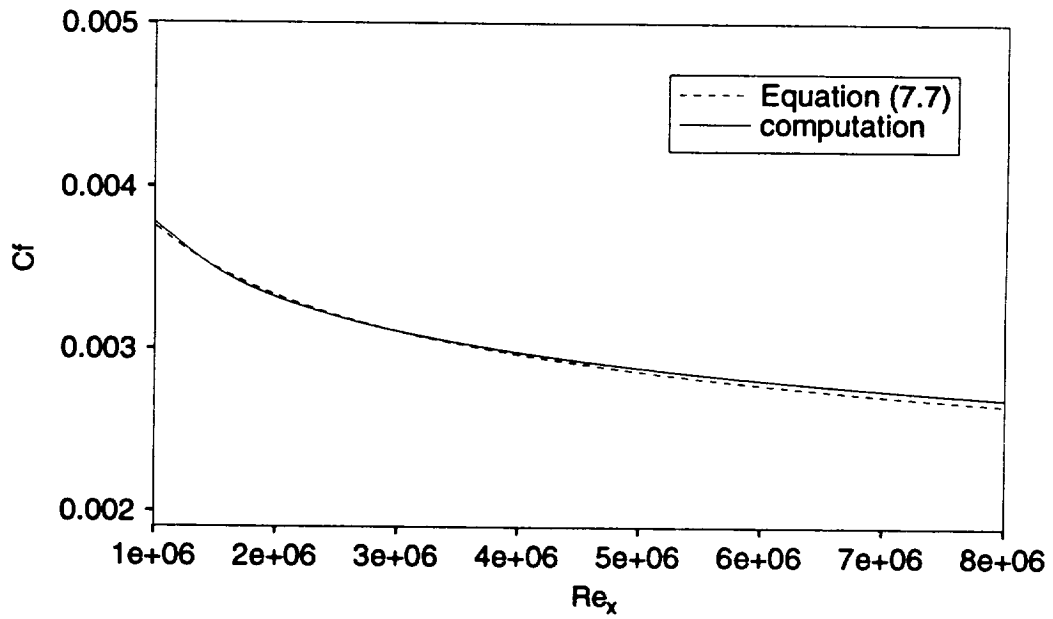


Figure 7.5: Friction coefficient, flat plate, skewed grid

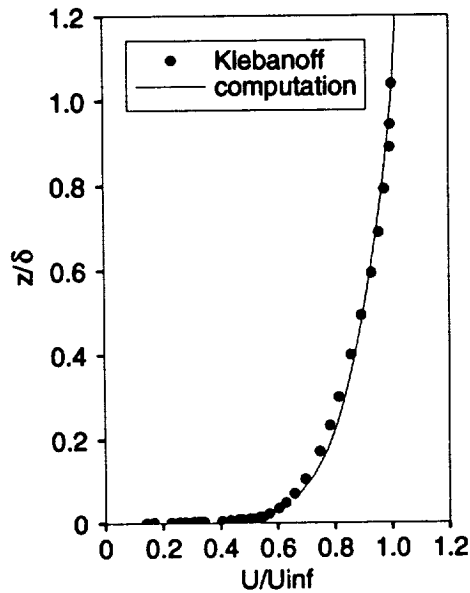


Figure 7.6: Velocity profile, flat plate, skewed grid

the shear stress transformations are working correctly for this case.

The velocity profile at a Reynolds number of 4.2×10^6 is shown in Figure 7.8. It is identical to those in the previous two test cases.

7.2.3 Low-Reynolds-number model test case

In addition to the flat plate test cases for wall functions, a test case was run to check the coding of the Chien (1982) low-Reynolds-number model. For this model, a fine grid is required at the wall in order to resolve the buffer region and the viscous sublayer. In these regions of the flowfield, which are not resolved when using wall functions, k and ϵ vary rapidly, and the method used to estimate the upstream k and ϵ distribution in the previous test cases becomes questionable. In order to simplify specification of the upstream boundary conditions, a semi-infinite flat plate with the

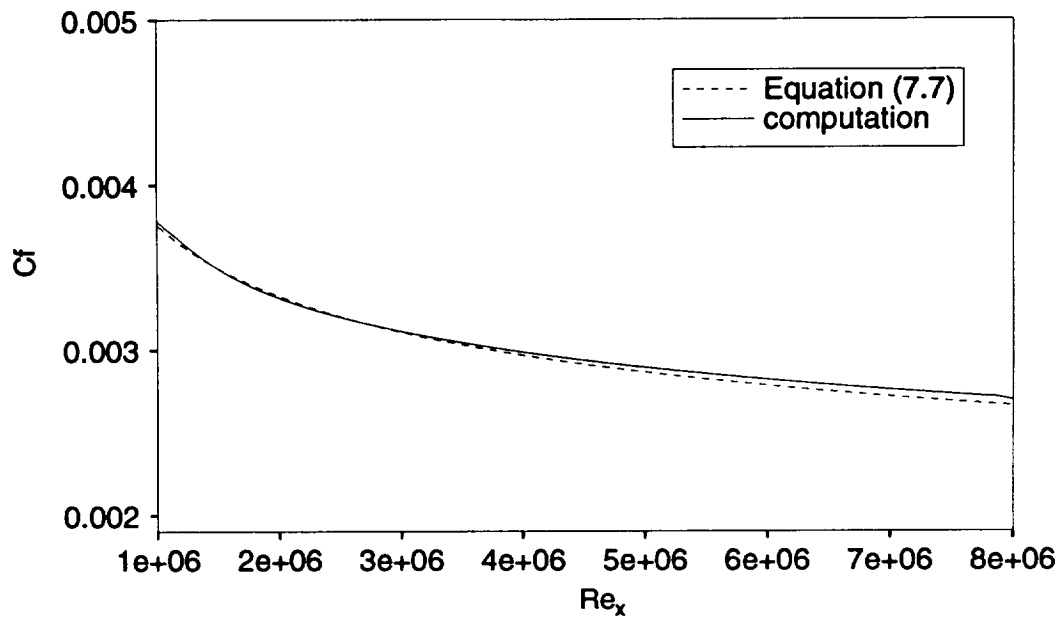


Figure 7.7: Friction coefficient, flat plate, angled domain

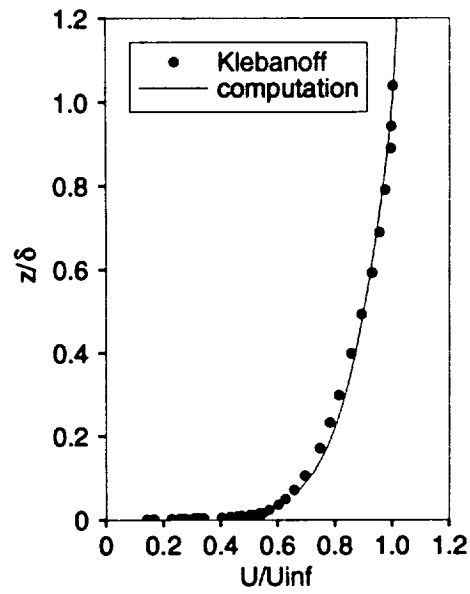


Figure 7.8: Velocity profile, flat plate, angled domain

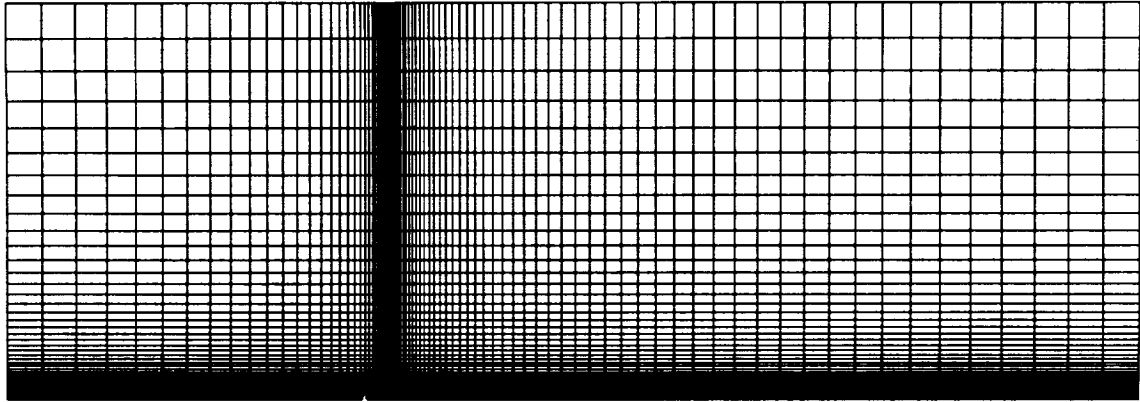
leading edge immersed in the freestream was used. The 91×91 grid is shown in Figure 7.9. For this grid, the reference length was the distance from the leading edge to the downstream boundary. The grid spacing at the wall was 1×10^{-5} based on the reference length. The domain extended from $x = -0.5$ to $x = 1.0$ in the streamwise direction and $z = 0$ to $z = 0.5$ normal to the plate, with the leading edge at $x = 0$. The Reynolds number (based on freestream velocity) was 9×10^6 at the downstream boundary, and the freestream Mach number was 0.2.

At the upstream boundary, the freestream density and momentum were fixed and the pressure was extrapolated. As in the previous cases, the freestream turbulent kinetic energy was fixed at $k/U_\infty^2 = 0.0002$. The freestream dissipation rate was computed based on an assumed nondimensional freestream turbulent viscosity of 1. At the stagnation streamline, all quantities were extrapolated. Specification of the wall, edge, and downstream boundary conditions were the same as in the previous test cases.

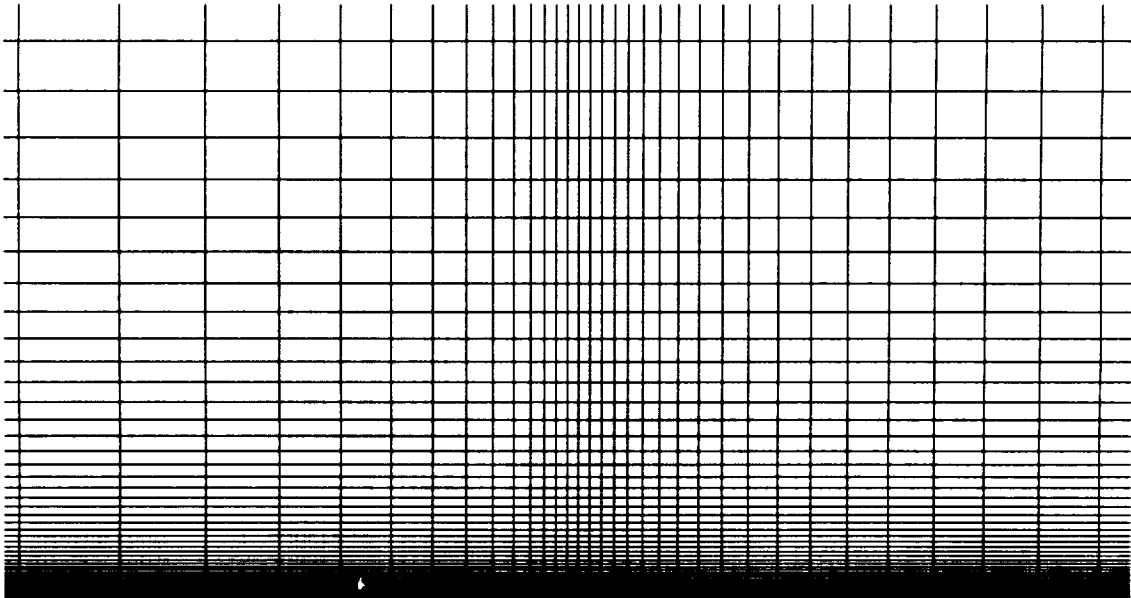
It is preferable to plot friction coefficient versus Re_θ (momentum thickness Reynolds number) rather than Re_x (Reynolds number based on distance from the leading edge) in order to avoid difficulties in locating the virtual origin of the plate. This was not possible in the previous test cases due to the coarse grids, but was appropriate here. A semi-empirical equation for the friction coefficient distribution is given by White (1974),

$$Re_\theta = \left(3.75 - \frac{2.75}{\lambda} \right) e^{0.4(\lambda-8)} \quad (7.10)$$

where λ is defined in equation (7.8). The computed friction coefficient distribution is compared to the values from equation (7.10) in Figure 7.10. Simpson's rule was used for the numerical integrations to calculate the momentum thicknesses. The

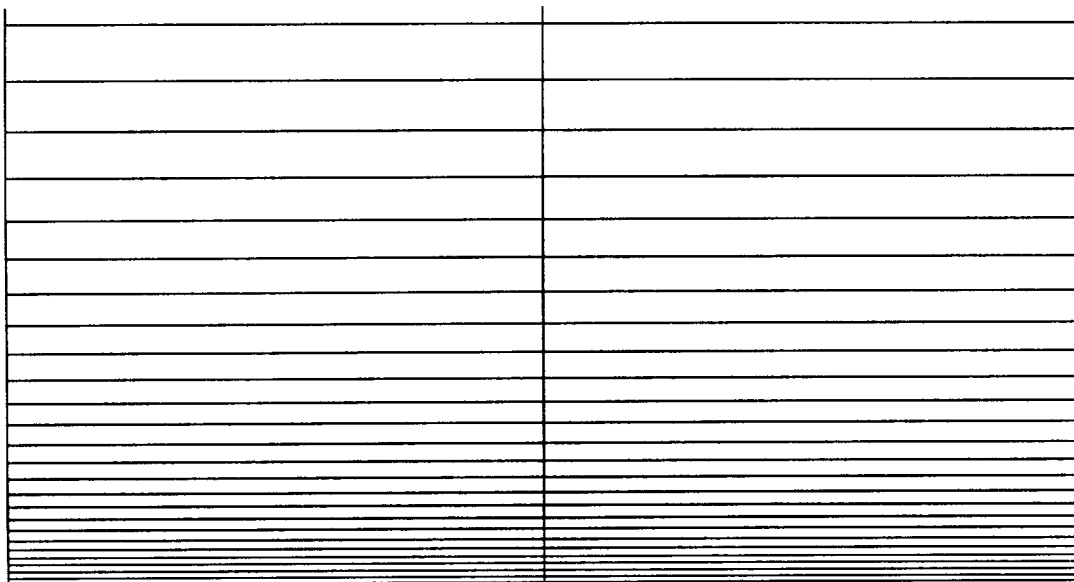


(a) Complete grid



(b) Close-up of leading edge region

Figure 7.9: Flat plate grid, low-Reynolds-number model test case



(c) Magnified close-up of leading edge region

Figure 7.9 (Continued)

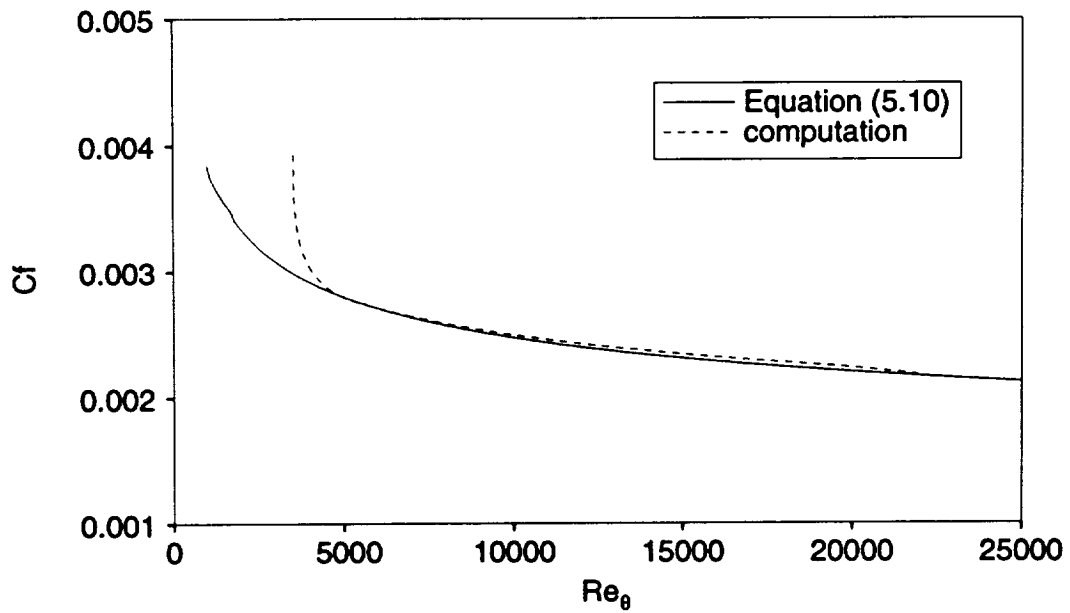


Figure 7.10: Friction coefficient, flat plate, low-Reynolds-number model test case

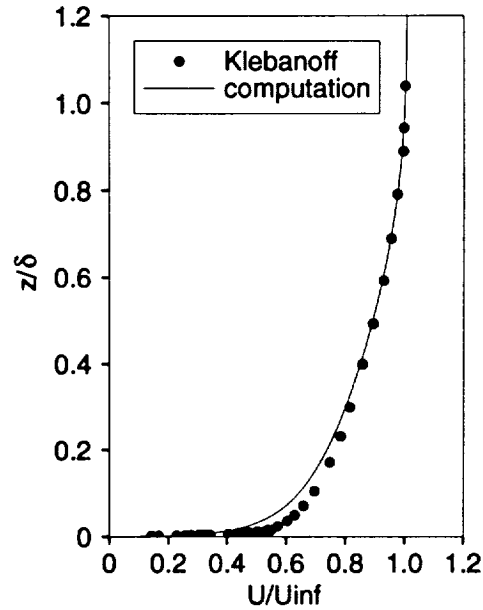


Figure 7.11: Velocity profile, flat plate, low-Reynolds-number model test case

agreement is good except near the the leading edge, where the boundary layer is too thin to resolve.

The boundary layer profile is compared to the Klebanoff (1955) data in Figure 7.11. The momentum thickness Reynolds number of the Klebanoff profile was calculated, and a profile was chosen from the computation at approximately the same momentum thickness Reynolds number. Figure 7.11 shows that the computed velocities are somewhat low near the “corner” of the profile, and that the match is good toward the outer edge. At first glance it appears that the momentum thicknesses cannot be equal for both curves. All of the computations exhibited a slight overshoot at the edge of the boundary layer, so this is probably the cause of the discrepancy.

7.3 Body of Revolution

7.3.1 Introduction

The next step was to test the wall function formulation on a curved surface. A well-behaved (i.e., non-separated) flowfield was desirable, since the purpose was to check the stress tensor transformations, and not yet to deal with the issue of the effectiveness of wall functions (in general terms) for separated flows.

Ramaprian, Patel, and Choi (1978, 1980) measured surface pressures, friction coefficients, and velocity profiles for incompressible flow over a body of revolution at zero and ten degrees angle of attack. The body consisted of half of a prolate spheroid with a hemispherical nose cap. The zero degree angle of attack case was computed here using the $k - \epsilon$ model with the present wall function formulation as well as the Baldwin-Lomax (1978) algebraic turbulence model and the Chien (1982) low-Reynolds-number $k - \epsilon$ model. Each model was run using three different grids to demonstrate the advantage of wall functions for this type of flowfield.

The experimental Reynolds number based on freestream velocity was 2×10^6 , and the freestream Mach number was approximately 0.06. The computations were run at the test Reynolds number, but the freestream Mach number was raised to 0.10 to avoid the incompressible limit of the code while still maintaining essentially incompressible flow. In the experiment, the boundary layer was tripped near the nose ($x = 0.04$), so that the computations were run completely turbulent.

Since the problem was symmetric about the centerline of the body, only half of the domain was solved. All grids were generated using the hyperbolic scheme of Chan and Steger (1991). Initially, an elliptic scheme was tried, but it proved impossible to

maintain the desired wall spacing. The hyperbolic scheme permitted excellent control over wall spacing, ran extremely fast, and was easy to use.

All distances in this section are normalized by the length of the body.

7.3.2 Fine grid

For the first grid, a wall spacing was desired that would provide adequate resolution for the Baldwin-Lomax and Chien models without requiring an excessive number of grid points. A wall spacing of $\Delta z_w^+ \approx 4$ was chosen to provide at least one point in the viscous sublayer, giving a spacing at the wall of 5×10^{-5} in units of body length. The grid is stretched geometrically normal to the body using a stretching ratio of 1.11. This relatively conservative value was chosen to minimize numerical errors due to grid stretching.

Although the location of the outer edge of the domain cannot be precisely specified when using hyperbolic grid generation, the desired value can be approximated. A value of twenty body lengths was chosen to minimize boundary proximity effects. A relationship between wall spacing, domain size, number of grid points, and geometric stretching ratio is given by Lewis and Pletcher (1986),

$$\Delta z_w = \frac{(K - 1)z_{max}}{K^{n-1} - 1} \quad (7.11)$$

where Δz_w is the wall spacing, z_{max} is the domain size, n is the number of grid points, and K is the stretching ratio. Solving for n ,

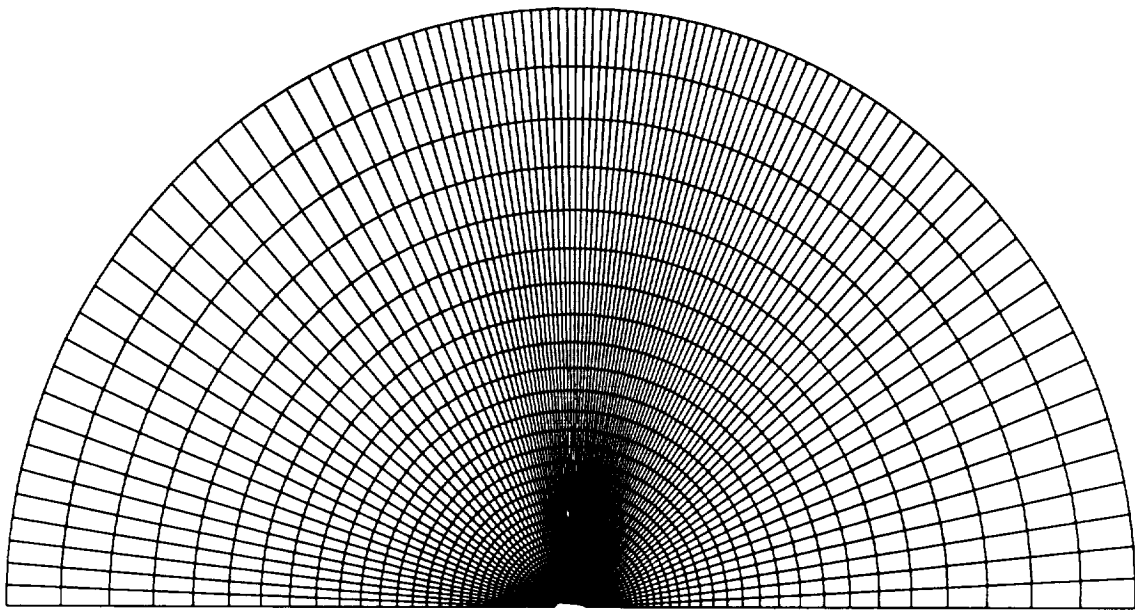
$$n = 1 + \frac{\log \left[1 + \frac{z_{max}}{\Delta z_w} (K - 1) \right]}{\log(K)} \quad (7.12)$$

For the present case, this equation yields $n = 104$. In the streamwise direction, 101 grid points were deemed sufficient for reasonable resolution. The body in the

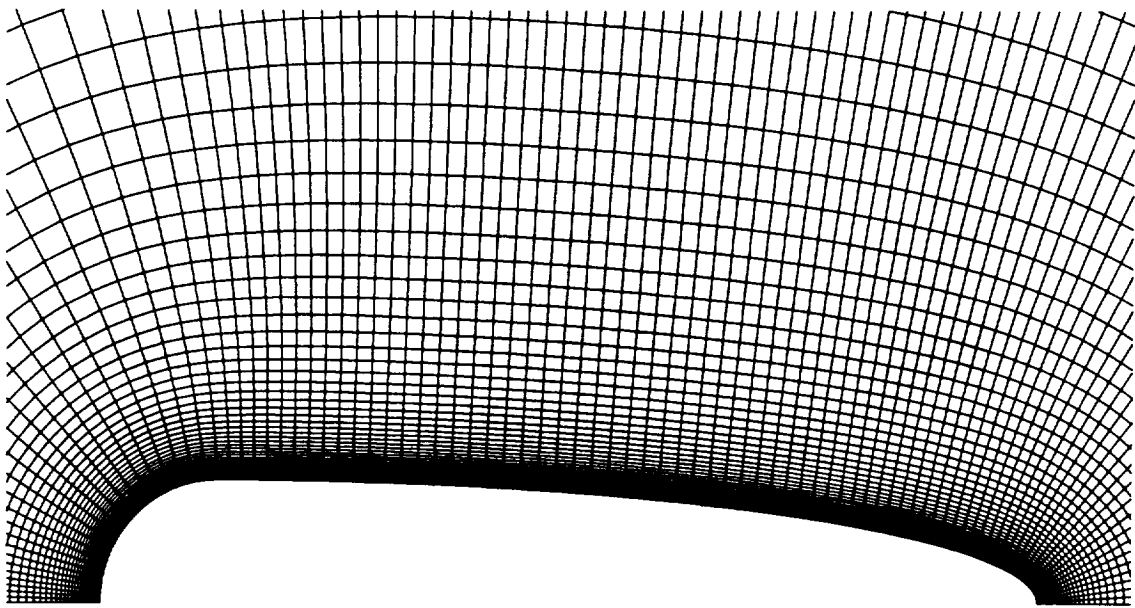
experiment was suspended by wires and therefore had no sting, so an o-grid was the natural choice for the grid configuration. The outer boundary shape, which was determined by the hyperbolic grid generator, was close to a semicircle. The grid is shown in Figure 7.12, and the coordinate system is shown in Figure 7.13. At the leading edge $x = 0$ and at the trailing edge $x = 1$. $z = 0$ at the centerline of the body.

At the outer edge of the domain, it is not clear (a priori) which points require an “inflow” boundary condition and which require an “outflow” boundary condition. This must be ascertained from the solution at each time step. At each boundary point, the inner product of the velocity vector and an outward normal vector to the boundary was computed. A value that is less than or equal to zero indicates an inflow point, and a value that is greater than zero indicates an outflow point. At inflow points, density and momentum components were fixed and pressure was extrapolated. At outflow points, pressure was fixed, and density and momentum components were extrapolated. At the axis, density and x-momentum were extrapolated. The z-momentum was set to zero due to symmetry. Flow along the axis streamline was irrotational, so Bernoulli’s equation was used to compute pressure. At the body surface, density and pressure were extrapolated, and momentum was set to zero.

The procedure for testing for inflow or outflow was also used for the $k - \epsilon$ equations. At inflow points both variables were specified, and at outflow points they were both extrapolated. At the axis, they were both also extrapolated. At the body surface the boundary conditions are part of the wall function formulation. For the Chien model, k and ϵ are set to zero at the wall. Since the tunnel turbulence level was not measured in the experiment, a value of 1/2% ($k/U_\infty^2 = 0.005$) was

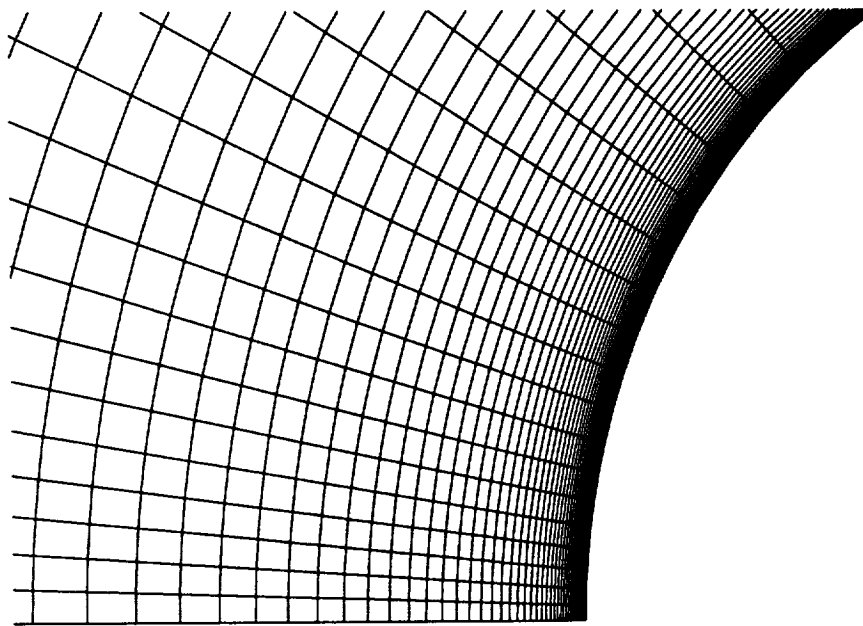


(a) Complete grid

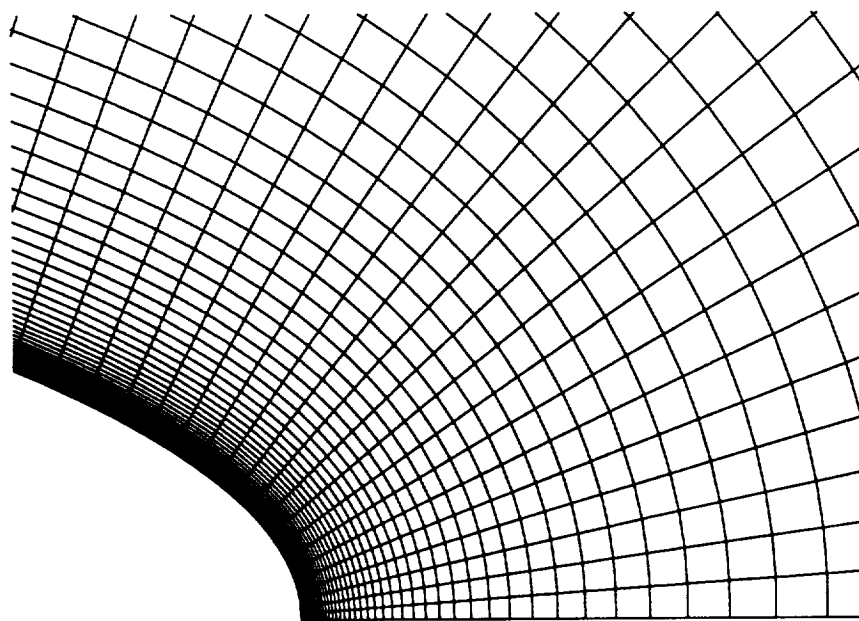


(b) Closeup of body

Figure 7.12: Body of revolution, 101×104 grid



(c) Closeup of leading edge



(d) Closeup of trailing edge

Figure 7.12 (Continued)

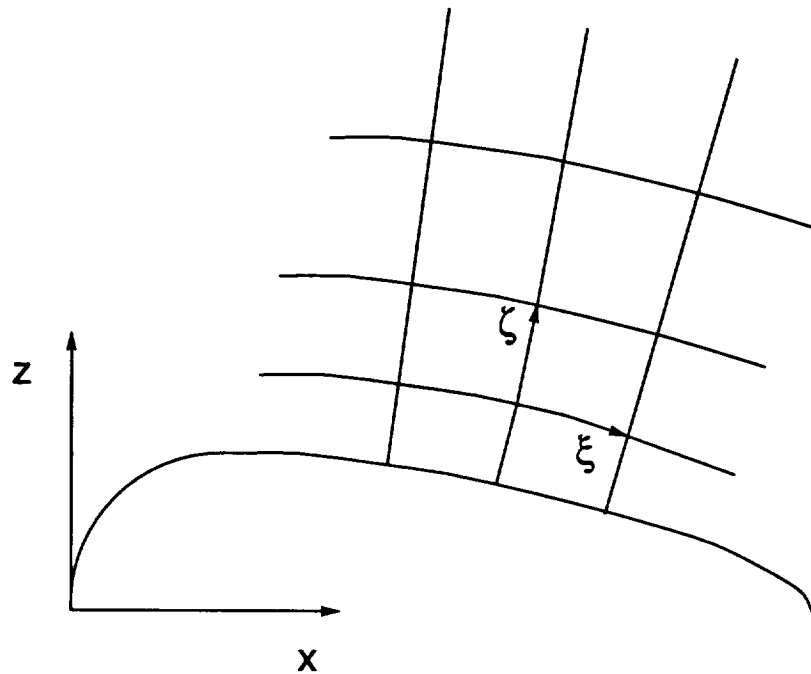


Figure 7.13: Body of revolution coordinate system

assumed. A freestream turbulent viscosity of 0.1 (nondimensional) was assumed, and freestream ϵ was calculated from equation (3.6).

Computed boundary-layer profiles are often affected adversely by even modest amounts of smoothing (Kaynak and Flores 1987). Since the physical shear stresses become large near walls, smoothing may be decreased in this region without causing the computation to become unstable. Various techniques of rolling off smoothing were tried, but the best solution was to simply turn the smoothing off at the seven grid points adjacent to the wall.

The computed pressure coefficient distribution is compared with the experimental data in Figure 7.14. All three turbulence models give good results, with a small discrepancy near $x = 0.1$. The discrepancy could be alleviated by increasing the grid

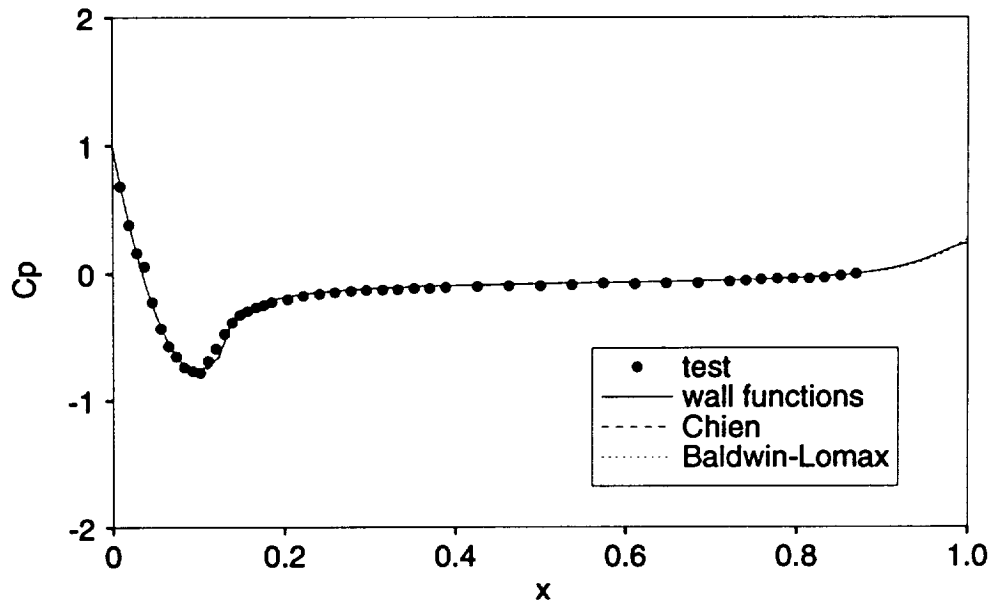


Figure 7.14: Pressure coefficient, body of revolution, 101×104 grid

resolution in that region, but since it is small, the present grid was deemed adequate.

Friction coefficients are shown in Figure 7.15. For the wall function case, the friction coefficient is calculated directly from equation (4.1). For the other two models, equation (7.5) is used, with $\tau_w \approx \mu \partial V / \partial n$, where V is the velocity magnitude and n is the normal distance from the wall. The measurements from all three models compare well with the test data with the exception of the first measurement station, where the Baldwin-Lomax model gave values slightly below the others. The first measurement station is located in a region of adverse pressure gradient immediately after the flow accelerated over the nose in a strongly favorable pressure gradient. This is a difficult situation to simulate accurately, and, as will be seen in subsequent plots, none of the models reproduce the character of the velocity distribution very well at this point.

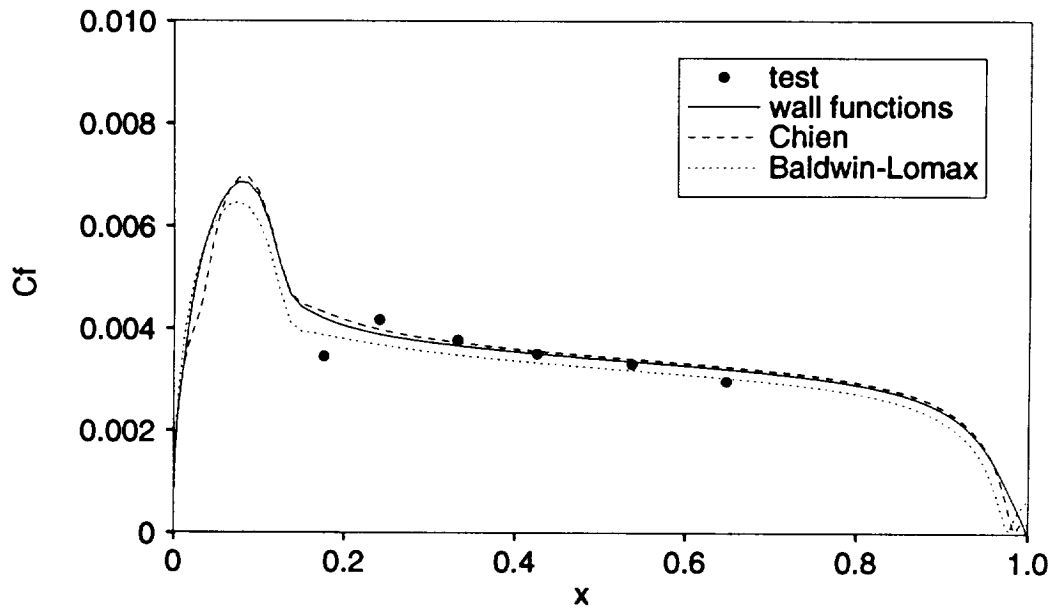


Figure 7.15: Friction coefficient, body of revolution, 101×104 grid

The velocity distributions are shown in Figure 7.16. All models compare reasonably well with the test data. More importantly, the wall function solution is very close to the the solution from the other two models. It should be kept in mind that the grid point adjacent to the wall lies in or near the viscous sublayer, and not in the log region. In this respect, it may be thought of as a “worst case” test for the wall functions.

7.3.3 Medium grid

Another grid was generated with $y_w^+ \approx 16$, with a wall spacing of 20×10^{-5} . This was outside the optimum range for all three models, since the Baldwin-Lomax and Chien models should have points in the viscous sublayer, and wall functions are

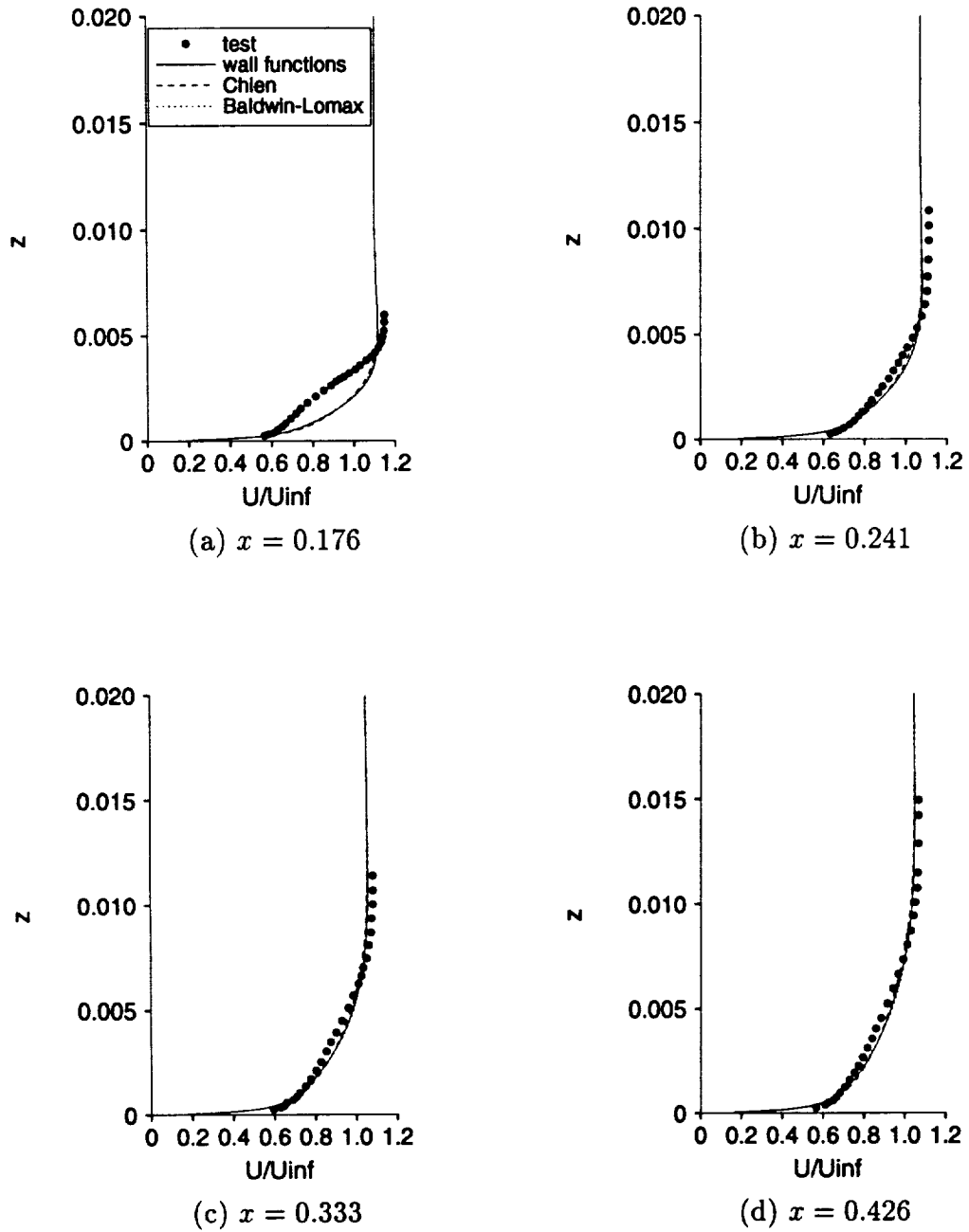


Figure 7.16: Velocity profiles, body of revolution, 101×104 grid

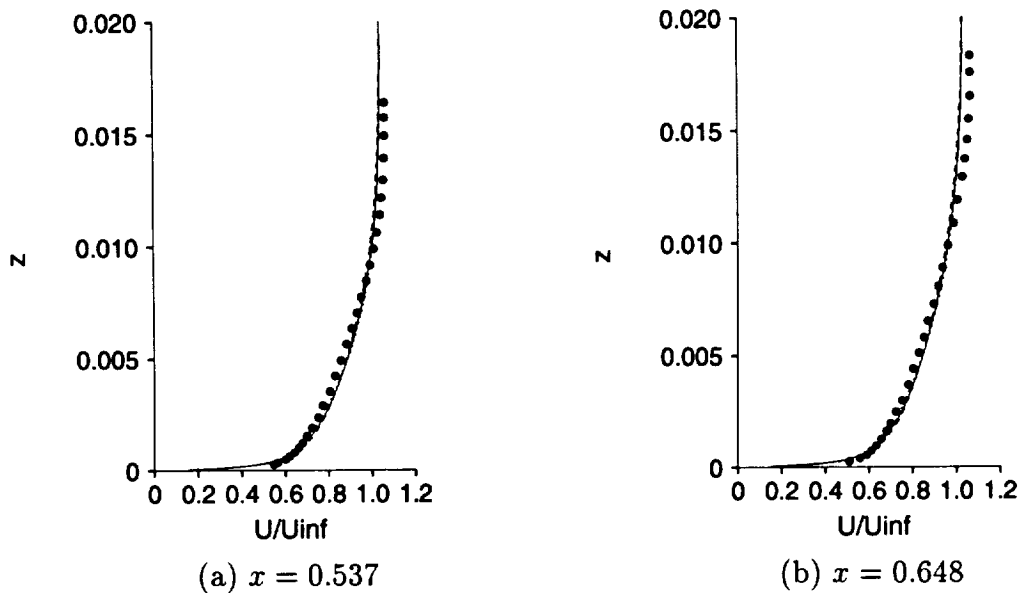


Figure 7.16 (Continued)

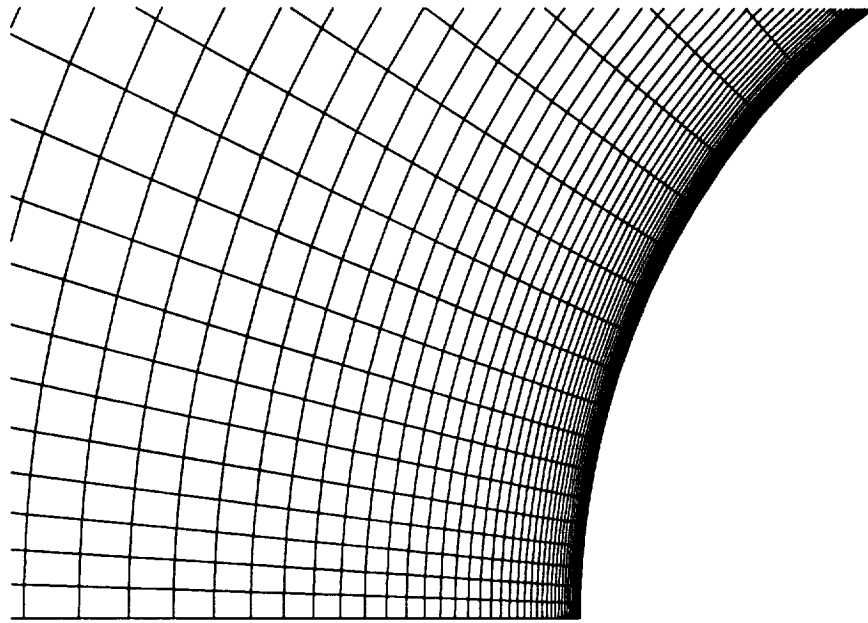
expected to work best when the point adjacent to the wall is in the log region.

The ζ grid lines are identical to those of the previous grid. The same domain size and stretching ratio were also used. Using equation (7.12), 91 grid lines are required in the normal direction. Closeups of the leading and trailing edge regions of this grid (101×91) are shown in Figure 7.17.

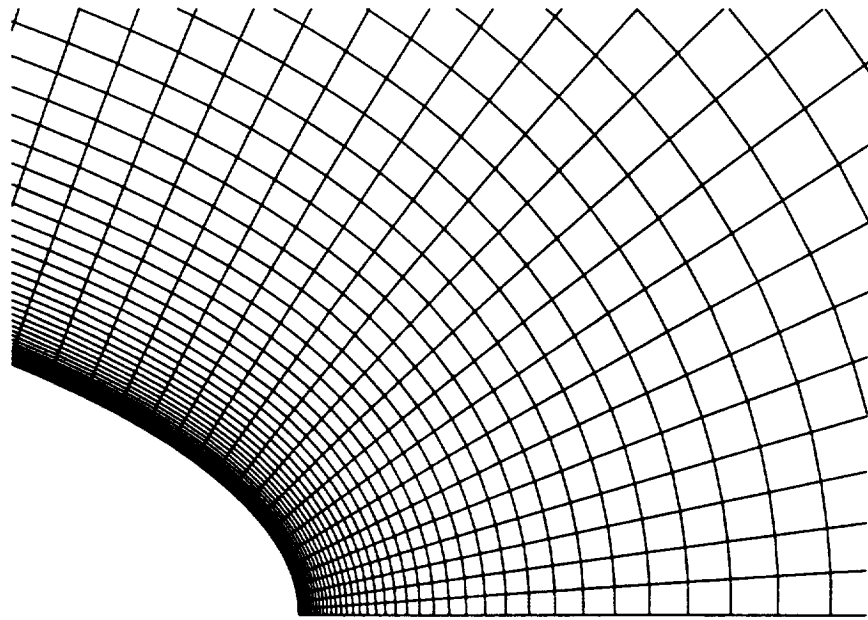
Pressure coefficients are shown in Figure 7.18. They are nearly identical to those for the fine grid.

Not all of the friction coefficients, shown in Figure 7.19, fare as well. The wall function solution still matches the test data well, but the other models cannot cope with this coarser wall spacing.

The velocity profiles, shown in Figure 7.20, exhibit a similar trend, though not as pronounced. The Baldwin-Lomax and Chien solutions are reasonable, but are clearly



(a) Closeup of leading edge



(b) Closeup of trailing edge

Figure 7.17: Body of revolution, 101×91 grid

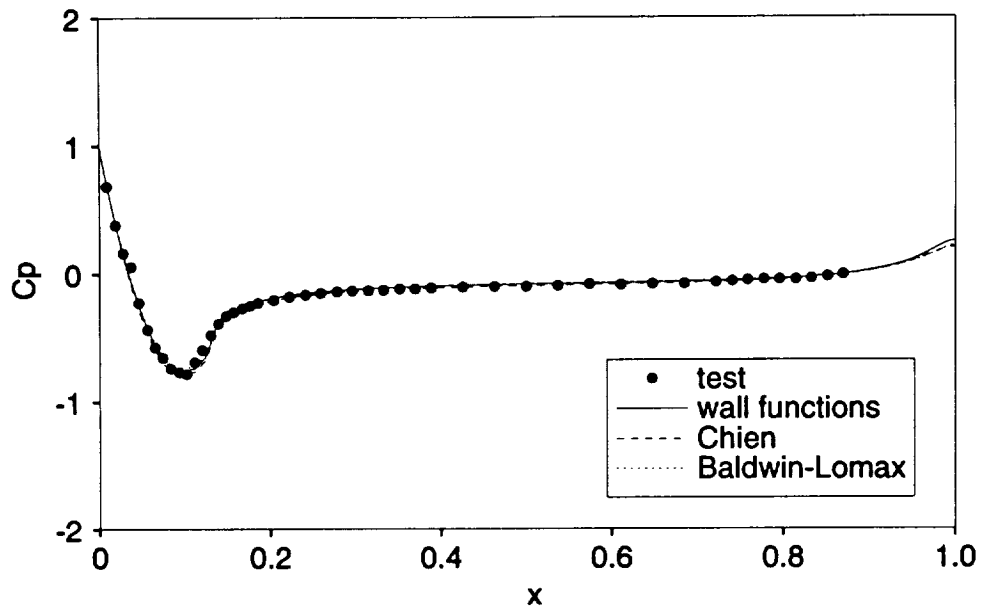


Figure 7.18: Pressure coefficient, body of revolution, 101×91 grid

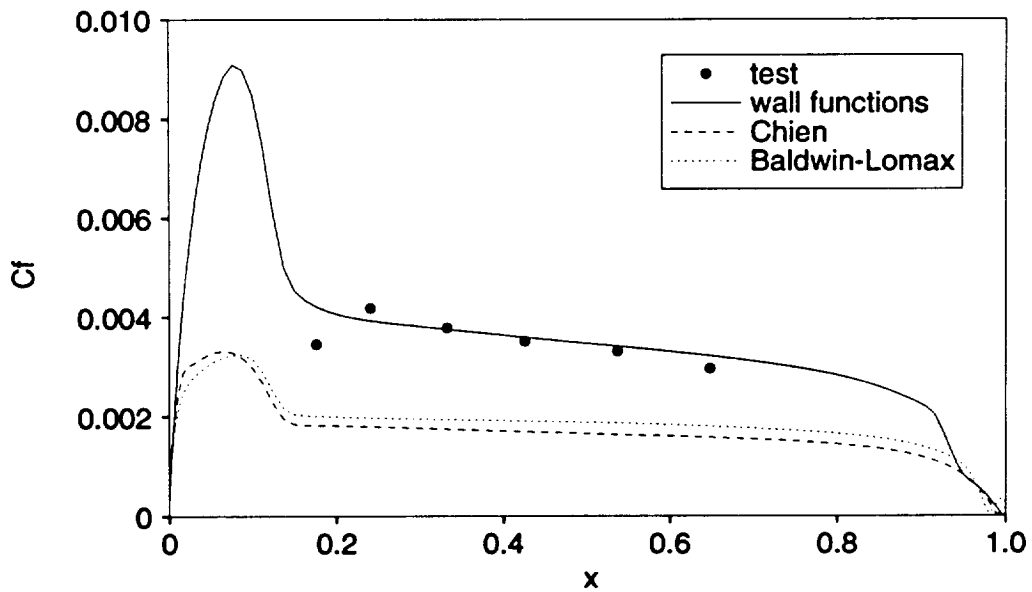


Figure 7.19: Friction coefficient, body of revolution, 101×91 grid

deficient as compared to the previous solution, while the wall function solution still looks good.

7.3.4 Coarse grid

A final grid was generated with $\Delta z_w^+ \approx 48$, or 60×10^{-5} in physical coordinates. Closeups of the leading and trailing edge regions of this grid (101×80) are shown in Figure 7.21. The results for this grid are shown in Figures 7.22, 7.23, and 7.24.

The 101×80 grid is clearly too coarse for the Chien and Baldwin-Lomax models, while the wall function solution still looks good. It should be noted that the wall function solutions for the different grids show some small differences. In the 101×80 grid, the point adjacent to the wall is in the log region, while this is not true for the other two finer grids. The boundary conditions for k and ϵ are more rigorous for points in the log region, as was discussed in the “Wall Functions” chapter. The different approaches are therefore expected to affect the results.

7.4 Prolate Spheroid

7.4.1 Introduction

Computation of the flow over a prolate spheroid at angle of attack is a particularly challenging problem for CFD. There exist regions of favorable and adverse pressure gradients, the flow on the leeward side may be massively separated, and laminar, transition, and turbulent regimes are frequently encountered.

In the late 1970's and early 1980's, a series of experiments was carried out at DFVLR (Deutsche Forschungs- und Versuchsanstalt für Luft- und Raumfahrt) to obtain detailed measurements of the surface flow on a prolate spheroid at angle of

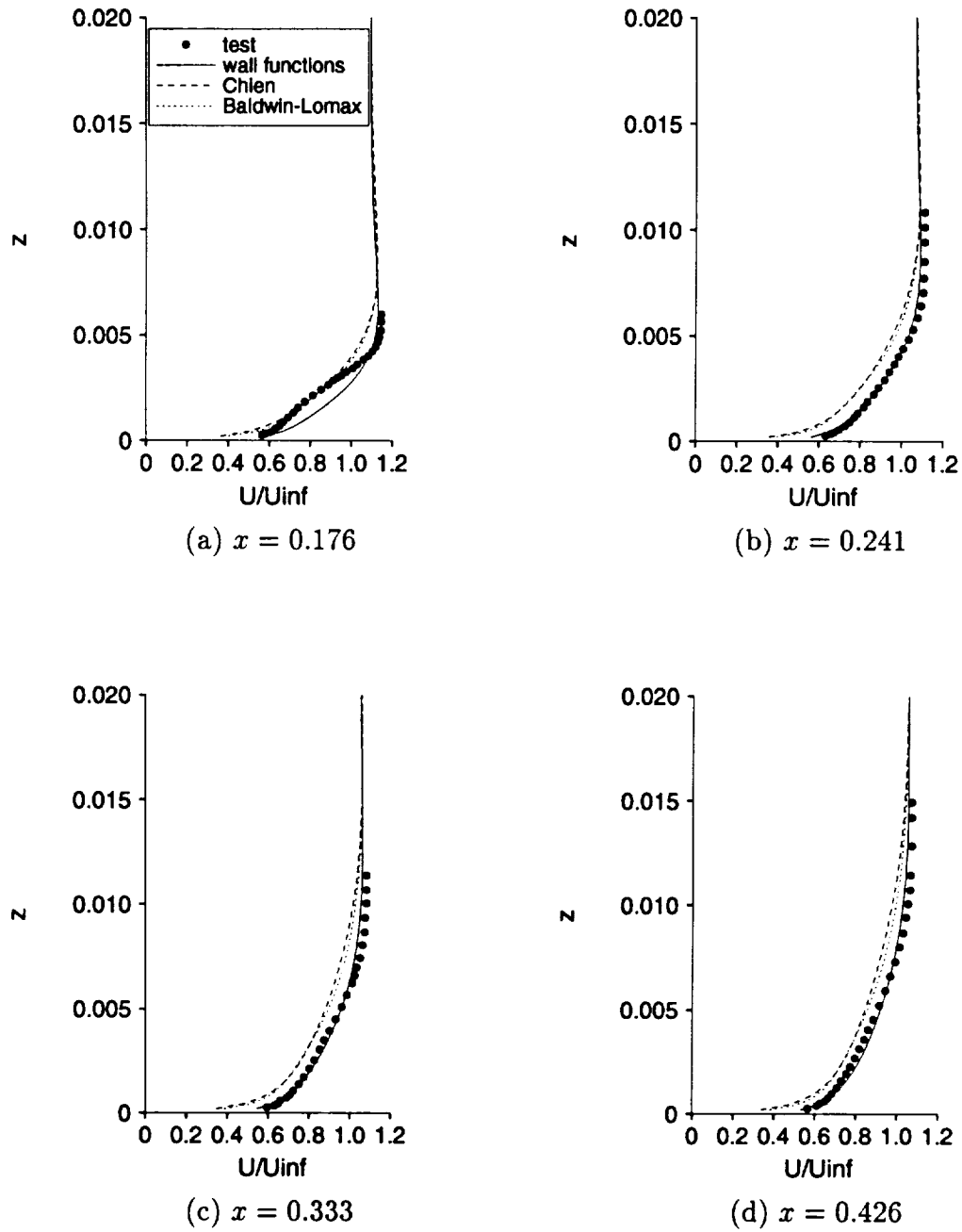


Figure 7.20: Velocity profiles, body of revolution, 101×91 grid

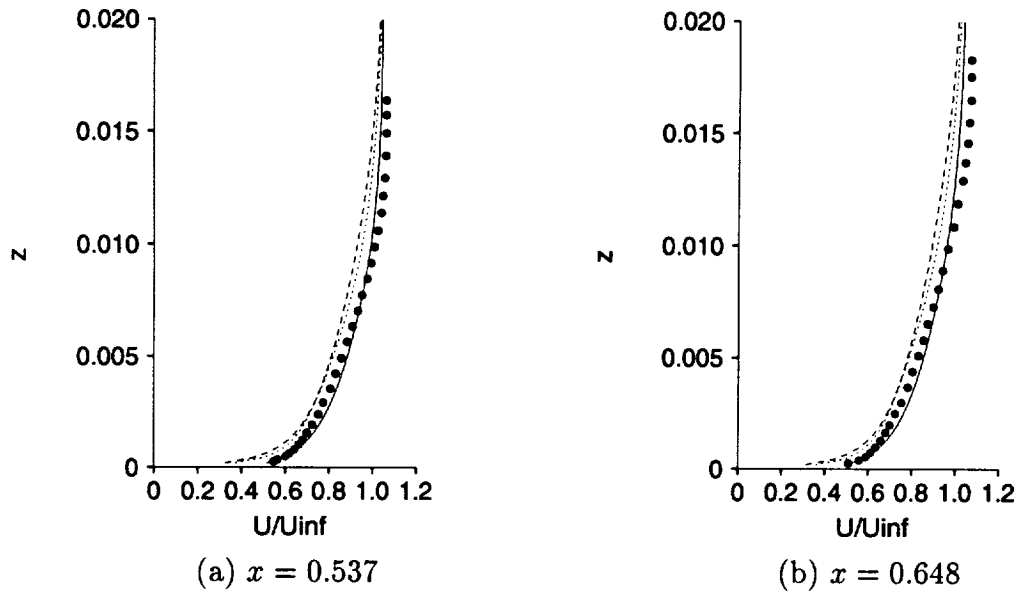
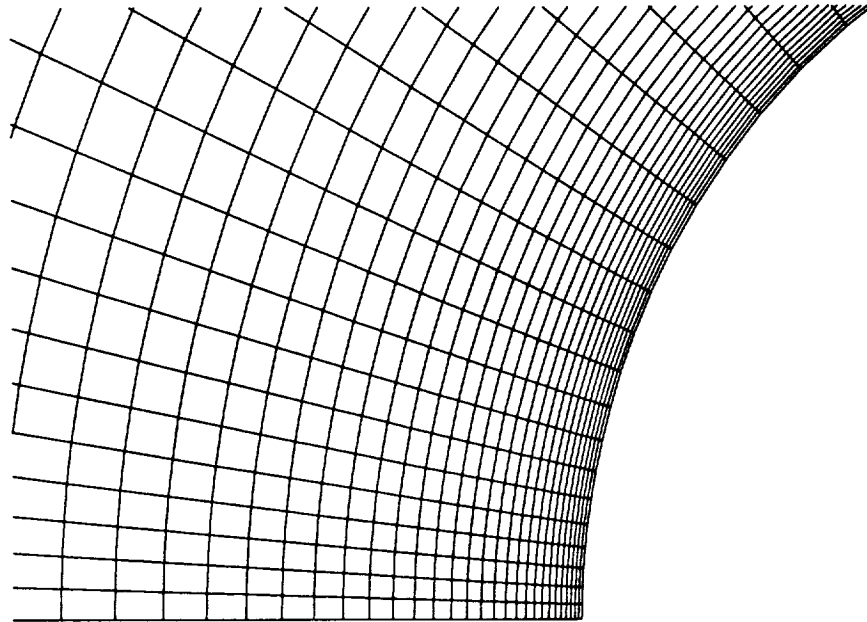


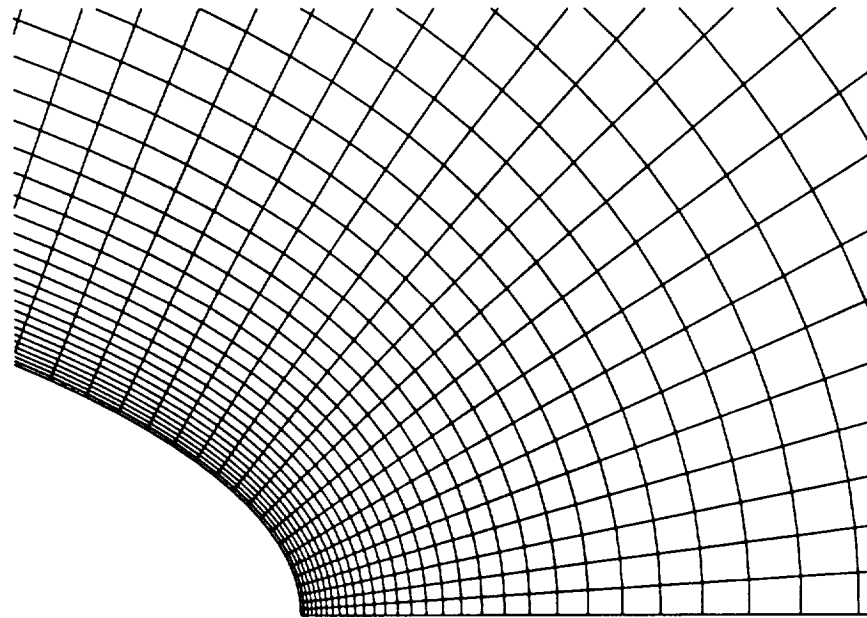
Figure 7.20 (Continued)

attack (Kreplin, Meier, and Maier 1978; Meier and Kreplin 1980a; Meier and Kreplin 1980b; Kreplin, Vollmers, and Meier 1982; Meier, Kreplin, and Vollmers 1983). One of the specific intents of the experiments was to provide data for turbulence modeling (Kreplin, Meier, and Maier 1978). Measurements were made over a range of Reynolds numbers and angles of attack. In some cases the boundary layer was tripped, while in others, natural transition was permitted to evolve.

In addition to surface pressure measurements, hot films were applied to the surface of the body to directly measure the magnitude and direction of the wall shear stress. Since the hot film was quite thin, it may be assumed that it was located within the viscous sublayer. Knowledge of the velocity and viscosity at a specified point in the viscous sublayer may be used to deduce the shear stress. Each hot film probe contained two elements at different angles to the flow direction. The difference



(a) Closeup of leading edge



(b) Closeup of trailing edge

Figure 7.21: Body of revolution, 101×80 grid

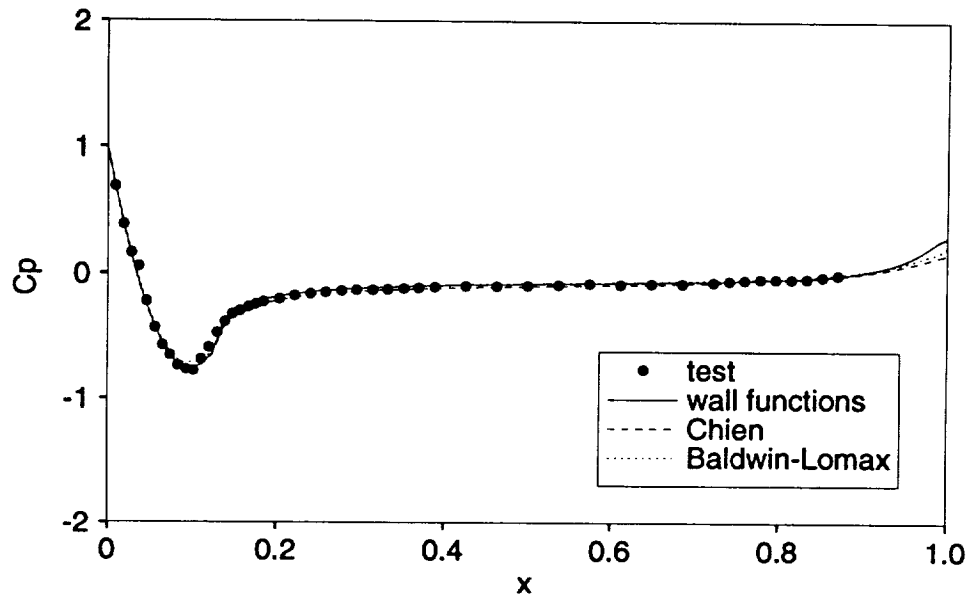


Figure 7.22: Pressure coefficient, body of revolution, 101×80 grid

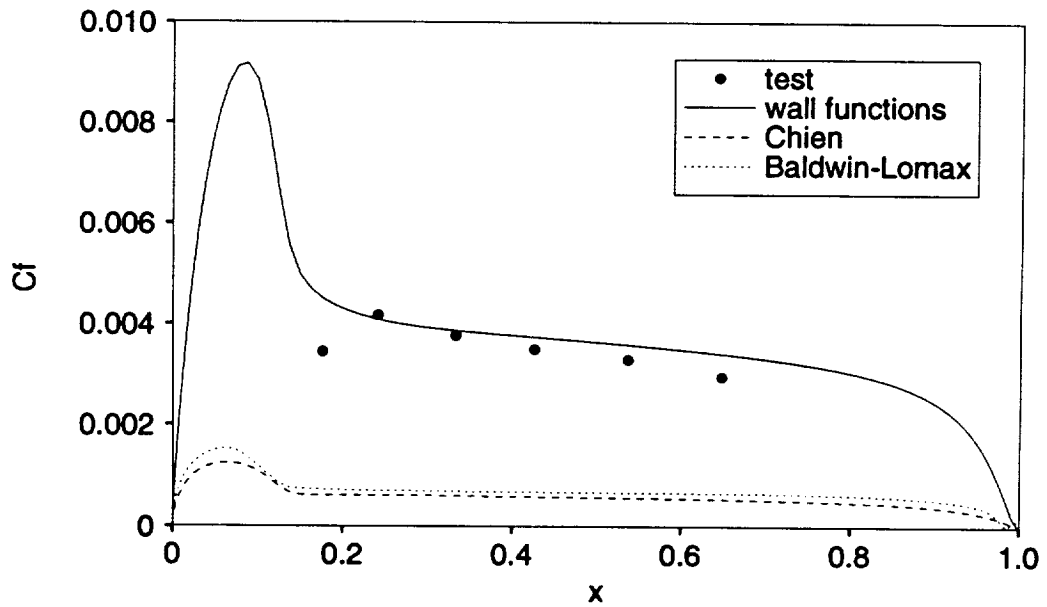


Figure 7.23: Friction coefficient, body of revolution, 101×80 grid

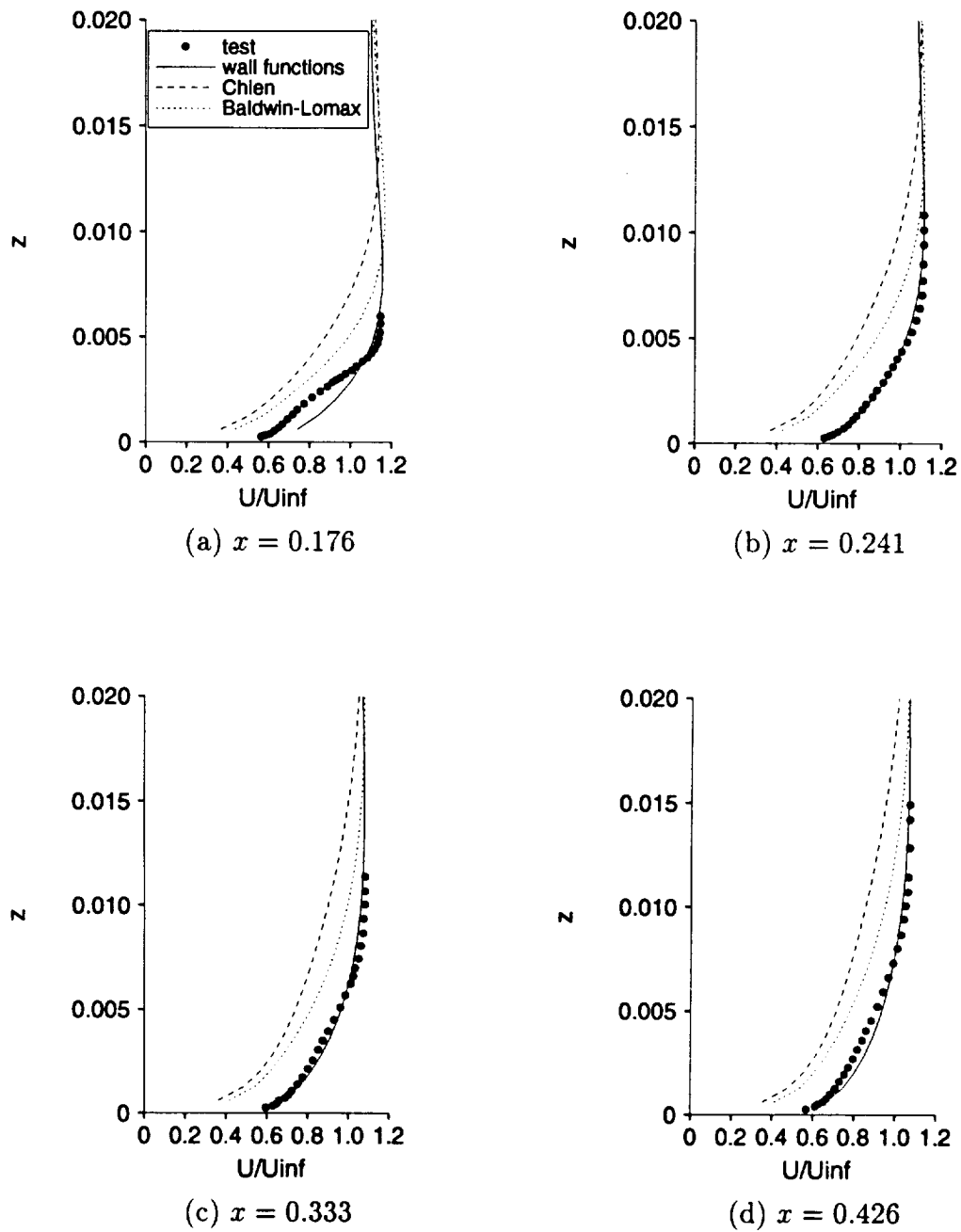


Figure 7.24: Velocity profiles, body of revolution, 101×80 grid

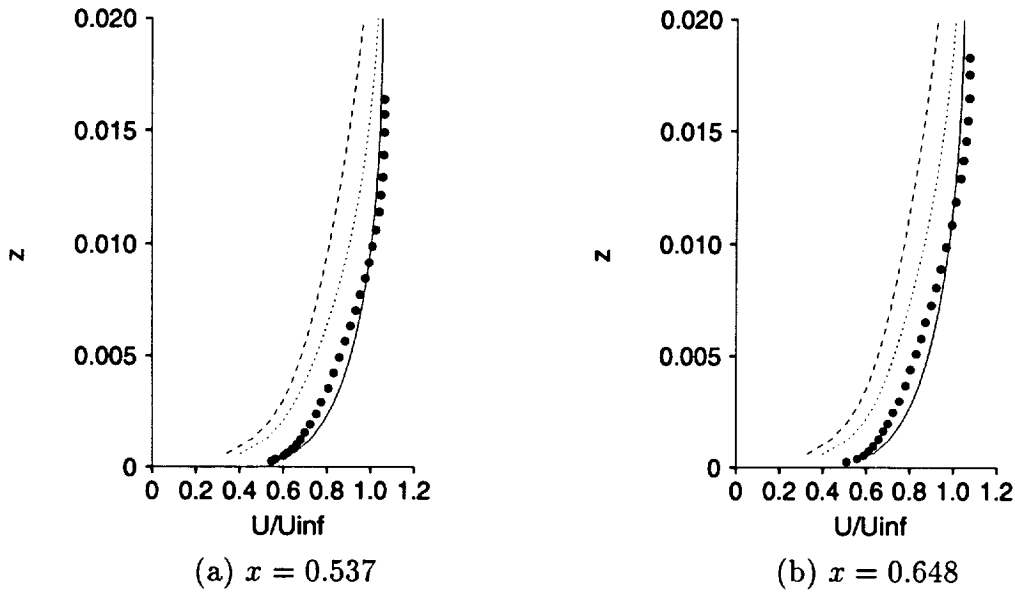


Figure 7.24 (Continued)

in response of each element was used to calculate the flow angle.

A number of investigators have computed this flowfield using both boundary-layer methods and the Navier-Stokes equations, and compared the results with the DFVLR test data. The Navier-Stokes computations are summarized in Table 7.1.

As can be seen in the table, a wide range of conditions were both tested and computed. The only computation shown which utilized a two-equation turbulence model was that of Kim and Patel. In their computation, a $k - \epsilon$ model was employed with a one-equation model patched in near the wall. It was therefore of interest to carry out the present computation at one of the conditions computed by Kim and Patel in order to compare the performance of wall functions to a method utilizing a different wall treatment.

The flow was laminar over most of the body in the $Re_{u_{\infty}} = 1.6 \times 10^6$ case, so

the case at $\alpha = 10^\circ$ and $Re_{u_\infty} = 7.2 \times 10^6$ was chosen for the present study. Another advantage of this case was that rather than tripping the boundary layer, it was permitted to go through natural transition to turbulence. This permitted trying a different method of forcing the transition point in the $k - \epsilon$ model (as compared to Kim and Patel). A freestream Mach number of 0.20 was chosen to minimize compressibility effects without excessively hindering convergence.

The use of wall functions is challenging for such a flow, due to the three-dimensionality of the boundary layer. In discussing their approach to solving this flowfield, Deng, Piquet, and Queutey (1990) stated that

The wall function approach is avoided in this work so that the equations ... are solved to the wall. For a significant increase in numerical troubles and of computing time (because the integration is carried out to $y^+ = .1 - .3$), the delicate problem of the threedimensional [*sic*] specification of the log-law is avoided.

7.4.2 Grid

It is desirable to have the grid point adjacent to the wall fall near the bottom of the log region. Since the values of Δy_w^+ are not known a priori, the following method was used for an estimate. The definitions of y^+ and C_f (equations (4.3) and (7.5)) show that $y^+ \propto \sqrt{C_f}$ for a given freestream velocity and viscosity. Using the flat plate equation (7.4) for a rough estimate of friction coefficient, it may be shown that $y^+ \propto \ln(Re)$. In the coarse grid test case for the body of revolution, $Re_{u_\infty} = 7.2 \times 10^6$, the wall spacing was 60×10^{-5} , and $\Delta y_w^+ \approx 48$. Using the above estimate of the variation of y^+ with Re_{u_∞} , wall spacing of 60×10^{-5} results

Table 7.1: Previous computations of DFVLR prolate spheroid

reference	$Re_{u_\infty} \times 10^{-6}$	angle of attack	equations	difference scheme	algorithm
Pan and Pulliam (1986)	1.6	10	TLNS ^a	central	ARC3D ^b
Vatsa, Thomas, and Wedan (1987)	1.6, 7.2, 7.7	10, 30	TLNS ^a	central, Roe	RK ^c
Panaras and Steger (1988)	7.7, 43.0	10, 30	TLNS ^a	F3D ^d	BTD ^e
Wang, Kandil, and Liu (1989)	1.6, 7.2, 7.7	10, 30	TLNS ^a , ITLNS ^f	Roe	RK ^c
Deng, Piquet, and Queutney (1990)	1.6	10	INS ^g	hybrid	PISO ^h , BG ⁱ
Kim and Patel (1991)	1.6, 7.2	10	INS ^g		PISO ^h , BTD ^e

^aTLNS, thin-layer Navier-Stokes.

^bARC3D, approximate factorization, diagonalized equations, scalar pentadiagonal solver.

^cRK, explicit four stage Runge-Kutta.

^dF3D, flux vector splitting in streamwise direction, central difference in other directions.

^eBTD, block tri-diagonal solver.

^fITLNS, incompressible TLNS.

^gINS, incompressible Navier-Stokes.

^hPISO, pressure implicit split operator.

ⁱBG, biconjugate gradient.

Table 7.1 (Continued)

reference	turbulence model	grid	approximate y_w^+	approximate domain size (body lengths)
Pan and Pulliam (1986)	laminar, BL ^j	66 × 66 × 66	4	10
Vatsa, Thomas, and Wedan (1987)	laminar, BL ^j	73 × 49 × 49		
Panaras and Steger (1988)	BL ^j	121 × 100 × 65	0.7	
Wang, Kandil, and Liu (1989)	laminar, BL ^j	75 × 49 × 49		6
Deng, Piquet, and Queutney (1990)	laminar, BL ^j	60 × 40 × 40	0.1-3.0	
Kim and Patel (1991)	CP ^k	70 × 41 × 60	<1	2-1/2

^jBL, Baldwin-Lomax.

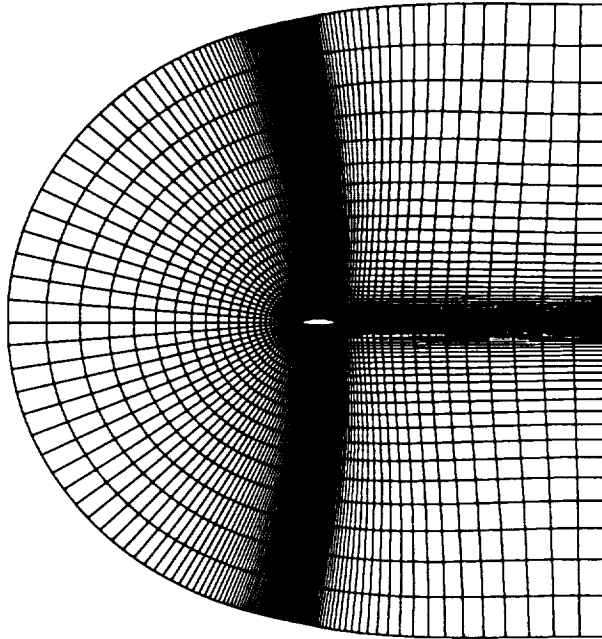
^kCP, Chien-Patel, $k - \epsilon$ model with one-equation model patched near wall.

in $\Delta y_w^+ \approx 44$ for the present Reynolds number. This value of Δy_w^+ is in the desired range, so a wall spacing of 60×10^{-5} is used for the present case.

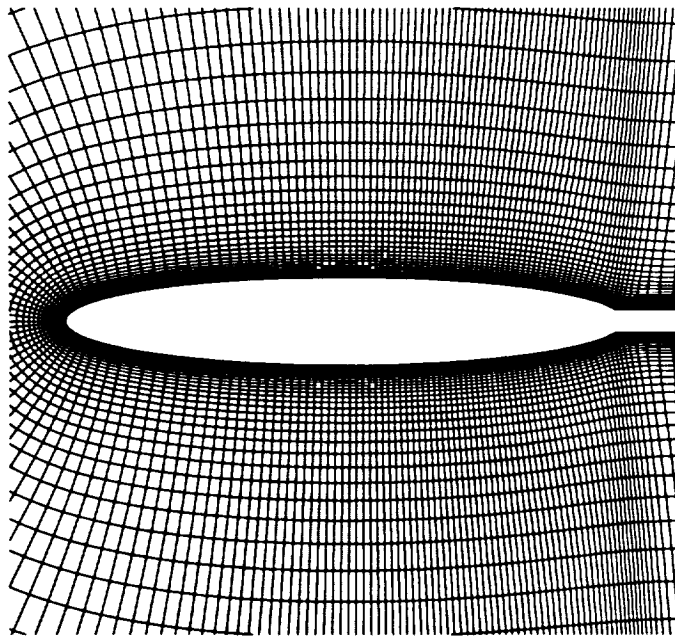
The test model was supported by a sting, and the sting is modeled in the present computation. A C-O grid is therefore employed. The domain for the body of revolution test cases extended approximately 20 body lengths in each direction. This proved to be more than adequate, so a domain size of 10 body lengths was used for the present case. A stretching ratio of 1.15 was chosen normal to the wall, resulting in 57 grid points (from equation (7.12)). There are 121 grid points along the surface of the body and sting, and 53 in the circumferential direction. The circumferential lines are somewhat clustered toward the leeward side in order to improve resolution in the separated region. Due to symmetry, only half of the flowfield was computed. The grid, which was generated using the same hyperbolic method as described in the previous section, is shown in Figure 7.25.

7.4.3 Boundary conditions

The boundary conditions for the present case were the same as those used for the body of revolution in the previous section with the exception of the axis at the leading edge, and with the addition of the symmetry plane conditions. In the previous case, the flow was irrotational along the axis since the body was at zero angle of attack, and Bernoulli's equation could be employed. In the present case this was not possible, so the following method was used. Density and the two components of momentum parallel to the symmetry plane were extrapolated to the axis. The component of momentum normal to the symmetry plane was set to zero due to symmetry. Using the extrapolated values of momentum, the pressure was then computed using the

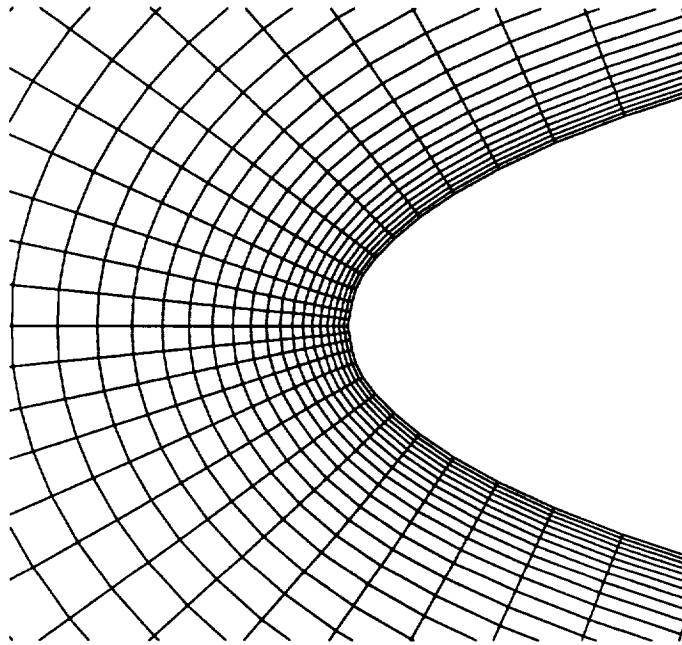


(a) Entire domain, side view

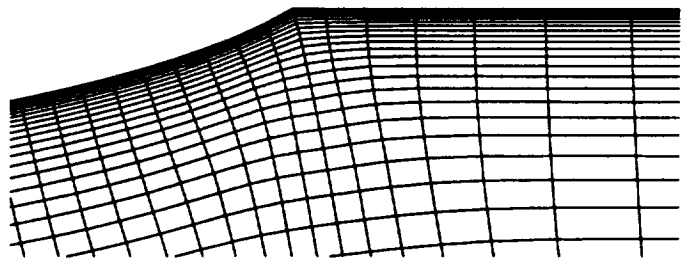
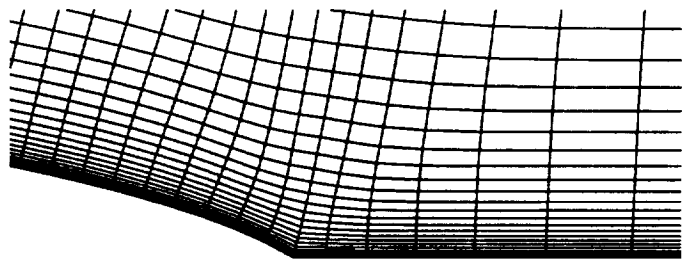


(b) Closeup of body, side view

Figure 7.25: Prolate spheroid, $121 \times 53 \times 57$ grid

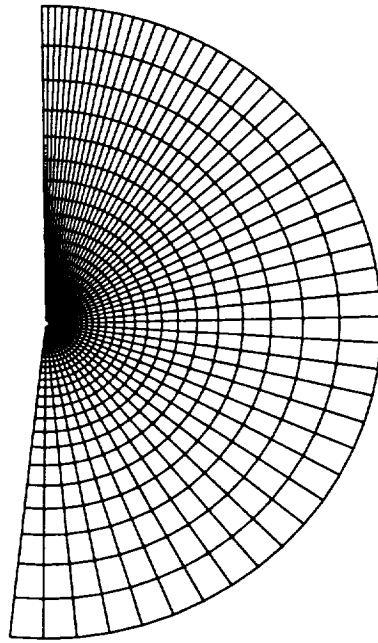


(c) Closeup of leading edge, side view

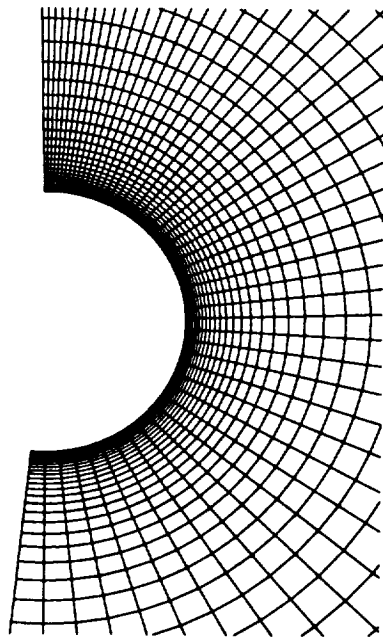


(d) Closeup of trailing edge, side view

Figure 7.25 (Continued)



(e) Entire domain, front view, near center of body



(f) Closeup of body, front view, near center of body

Figure 7.25 (Continued)

x-momentum equation. At the symmetry planes, values of all dependent variables are reflected, e.g. $\rho_{k=1} = \rho_{k=3}$.

It was found in previous runs that, below a certain level, the freestream turbulent kinetic energy had little effect on the results. Larger values, however, had a marked effect. For the small values, any diffusion of turbulent kinetic energy in to the boundary is apparently overwhelmed by the production rate in the boundary layer. Since the “small” values gave the best agreement with the test data, $k/(u_\infty)^2 = 1 \times 10^{-8}$ is used here. A small value is employed, rather than zero, because the source terms in the $\rho\epsilon$ transport equation contain k in several denominators. A nondimensional freestream turbulent viscosity of 0.01 was assumed, and the freestream ϵ was calculated from equation (3.6). The small value of μ_t was chosen so as not to affect the laminar flow significantly, as will be clarified below. As in the previous test cases, lower limiters on both k and ϵ are set to freestream values.

When using algebraic turbulence models, tripping a laminar boundary may be effected simply by turning the model on at a specified location in the flowfield. This is possible because the turbulent viscosity is a function of the local flowfield, and history effects are not considered. With two-equation models, the turbulence quantities are transported throughout the domain. Kim and Patel (1991) solved the turbulence transport equations over the entire domain, and then, at the end of each step, overwrote the computed turbulent viscosities with zeros at those points designated as being laminar. A problem with this approach is that k and ϵ are increasing in the boundary layer, mostly due to the production terms, in the region of laminar flow. Their profiles are quite developed by the time the points of forced transition are reached. In the present study, the time step was set to zero at all laminar grid

points. The freestream values of k and ϵ were therefore maintained at these points, and the turbulence was permitted to evolve downstream of the trip line. Since a small freestream value of μ_t is used, the laminar flow was not significantly affected.

The friction coefficient map taken from Kreplin, Vollmers, and Meier (1982) is shown in Figure 7.26. The vector lengths are proportional to the measured wall shear stresses, and they are oriented at the circumferential angles at which the shear stresses act. It is not possible to deduce a precise transition line from this map, but an approximate line may be determined from the regions where the friction coefficient rapidly increases. Figure 7.27 shows an unwrapped surface grid with points marked at the computational trip line.

7.4.4 Additional considerations

Smoothing coefficients of $\epsilon_4 = 0.10$ and $\epsilon_2 = 0.028$ were used (see equations (6.79) and (6.80)), based on several test runs to see how low they could be pushed without compromising stability.

Friction coefficient angle data were measured in the experiment, based on the difference in the response of the two elements of the hot-film probes. The friction coefficient angle, which is assumed to be identical to the flow angle in the computation, is changing as the wall is approached. The wall spacing is fairly large since wall functions are being used, and it is therefore difficult to deduce the limit of the angle at the wall. The flow angle was computed at the grid points near the wall, and second order Lagrangian extrapolation was used estimate the angle at the wall.

A similar difficulty was encountered in computing the friction coefficient in the laminar region of the flowfield. Third order Lagrangian interpolation was used to

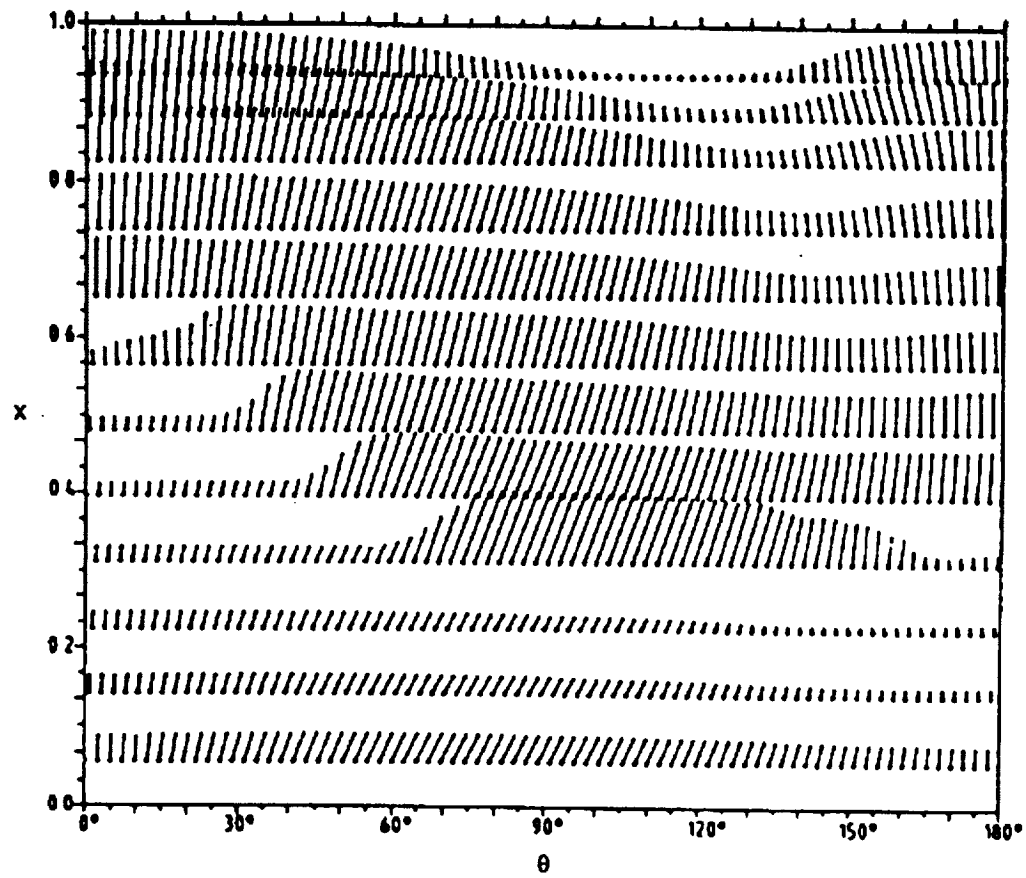


Figure 7.26: Friction coefficient map from Kreplin, Vollmers, and Meier (1982)

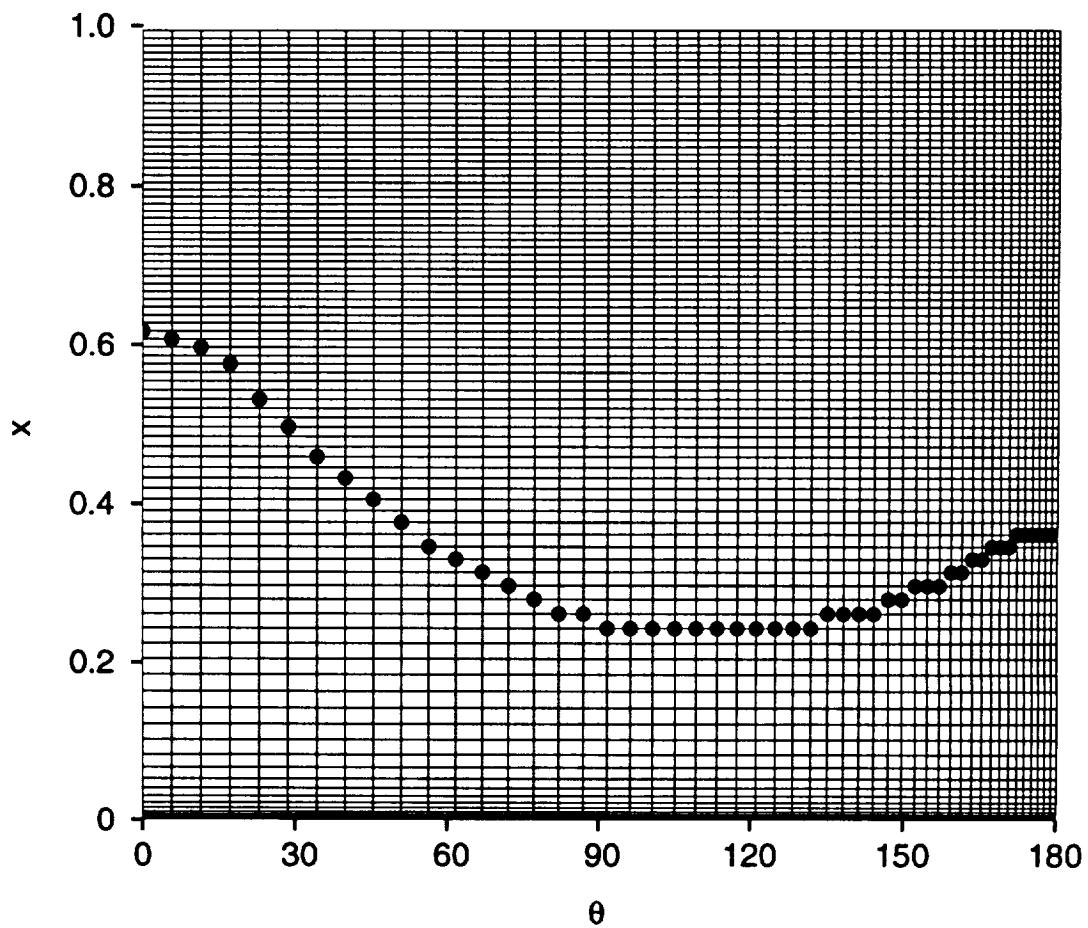


Figure 7.27: Unwrapped surface grid with trip points, prolate spheroid

estimate the velocity parallel to the wall, at a normal distance of 1×10^{-5} . The shear stress was then computed from $\tau_w = \mu V_p/n$, where V_p is the parallel velocity component, and n , the normal distance to the wall, is equal to 1×10^{-5} .

In Kreplin, Vollmers, and Meier (1982), both friction coefficients and friction coefficient angles were presented in the form of the friction coefficient map shown in Figure 7.26. It is difficult to deduce accurate friction coefficients and angles from data in this form. A tape containing the data had been sent to NASA Ames by Tuncer Cebeci of McDonnell-Douglas, and these are the data that were used for comparison. The tape also included surface pressures, which were not presented in the paper.

7.4.5 Results

Pressure coefficients at five axial locations are compared with the test data and with the computation of Kim and Patel (1991) in Figure 7.28. At all sections with the exception of the first, several test points fail to follow the trend of the remaining points. An example of this may be seen in Figure 7.28(d) at $\theta \approx 115$. None of these points coincide with the separation line, and no anomaly is apparent in the other measurements in the same regions, so the discrepancy is most likely due to measurement error.

In the results from the present computation, a small kink may be observed in Figure 7.28(b) at $\theta \approx 55$ and in Figure 7.28(c) at $\theta \approx 25$. These are the points at which the turbulence model was turned on in the computation to simulate transition. The pressure is affected by the sudden addition of the normal turbulent stresses (the $-\frac{2}{3}\delta_{ij}\bar{\rho}k$ term in equation (3.1)).

Both computations capture the character of the pressure distributions, but the

magnitudes of the pressures are somewhat off in both computations. Kim and Patel speculated that the differences were due to blockage effects in the wind tunnel or a bias in the pressure measurements. The present results imply that the differences may be due to errors in the computations, since the computed values straddle the measured values.

Friction coefficients are shown in Figure 7.29. At all sections with the exception of the first, several test points fail to follow the trend of the remaining points. An example of this may be seen in Figure 7.29(d) at $\theta \approx 115$. None of these points coincide with the separation line, and no anomaly is apparent in the other measurements at these points.

The match of the present computation is not very good at the first section. Here, the flow is fully laminar, and the difficulties in deducing laminar friction coefficients are encountered, as described above. This section is fairly close to the leading edge, and the boundary layer is relatively thin. The boundary layer is not well resolved here, encompassing approximately 5 – 7 grid points.

The next section, at $x = 0.395$, has laminar flow near the windward symmetry plane and turbulent flow over the remainder of the circumference. The transition to turbulence after the $k - \epsilon$ model is tripped is quite abrupt, even though the freestream k and ϵ are maintained up to the trip point. The present computation shows the beginning of separation near $\theta = 150^\circ$, but it is not yet evident in the test data.

At $x = 0.565$, the present computation compares fairly well with the test data. The minimum C_f , which is near the separation line, is close to that of the test data, and the increase in friction coefficient near the leeward symmetry plane is captured.

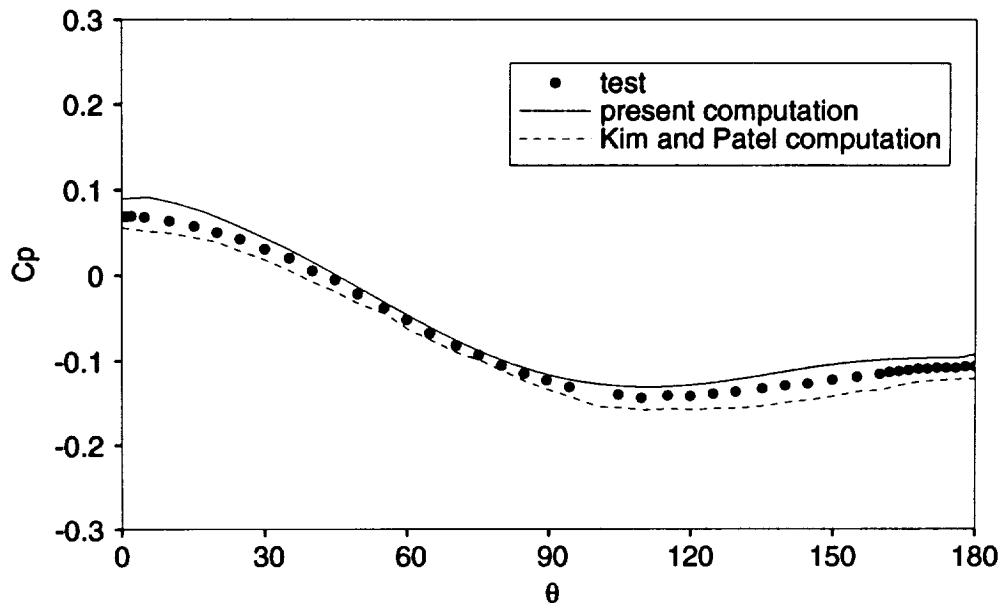
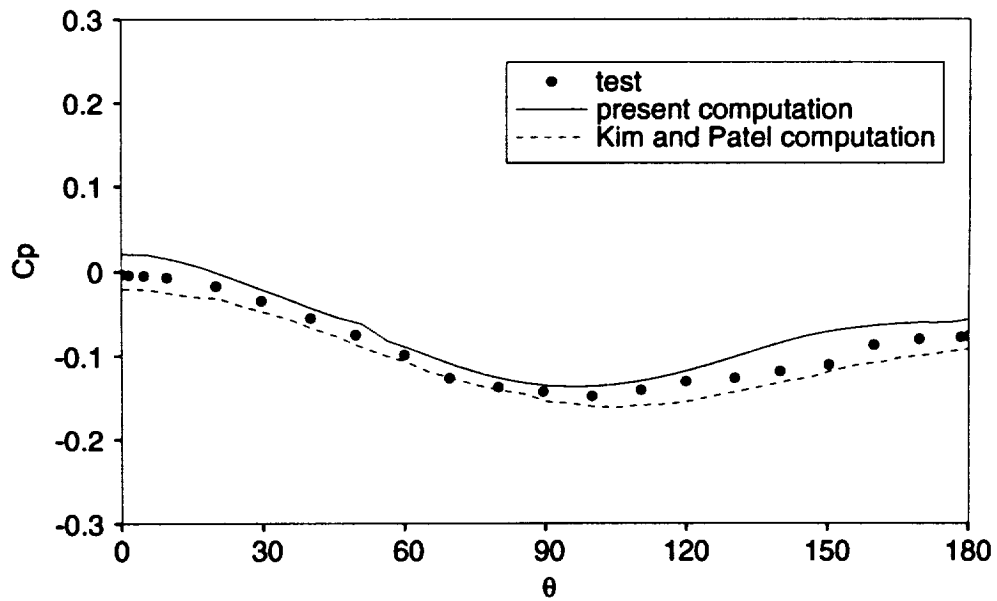
(a) $x = 0.190$ (b) $x = 0.356$

Figure 7.28: Pressure coefficient, prolate spheroid

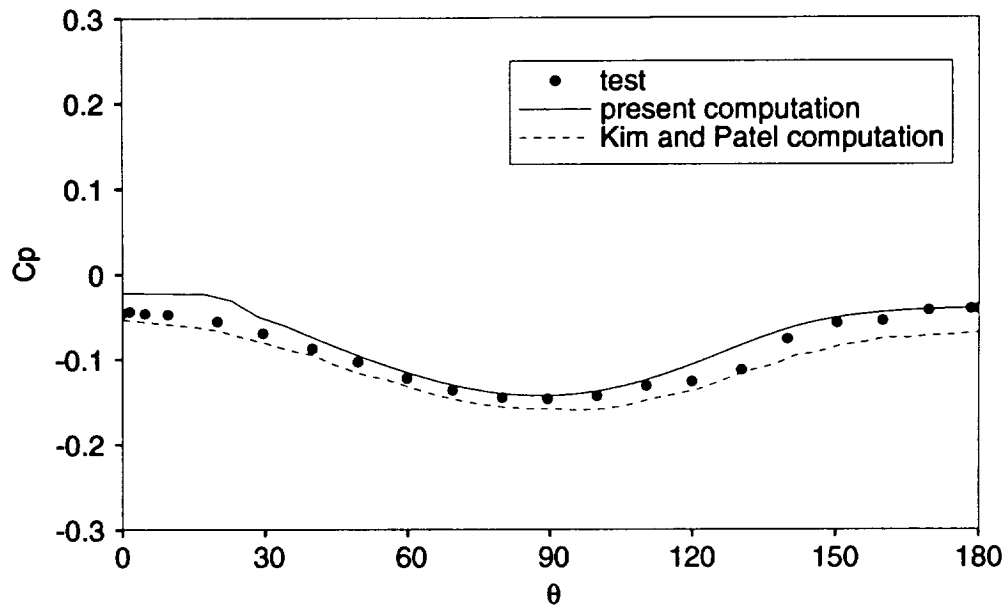
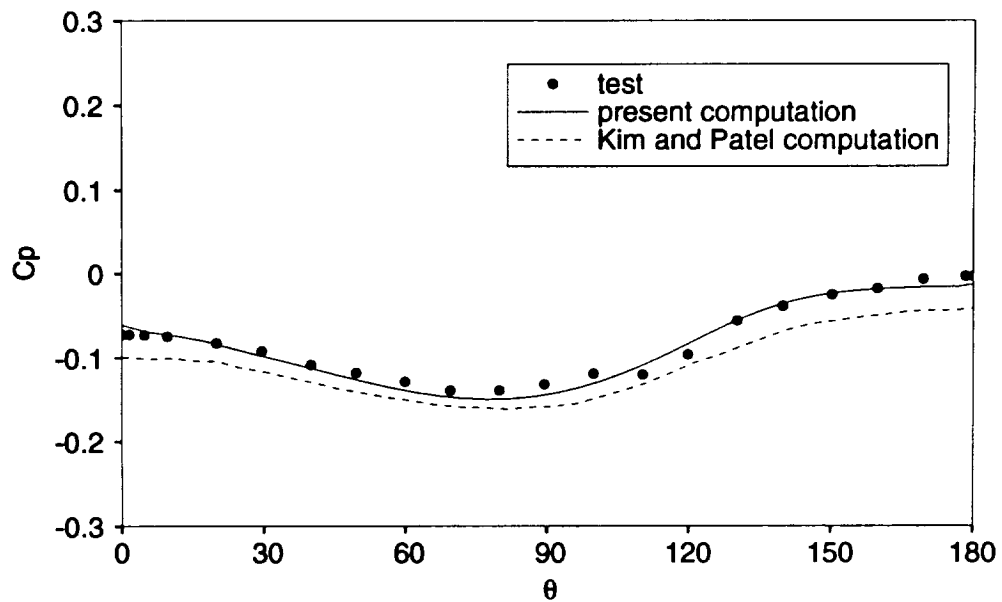
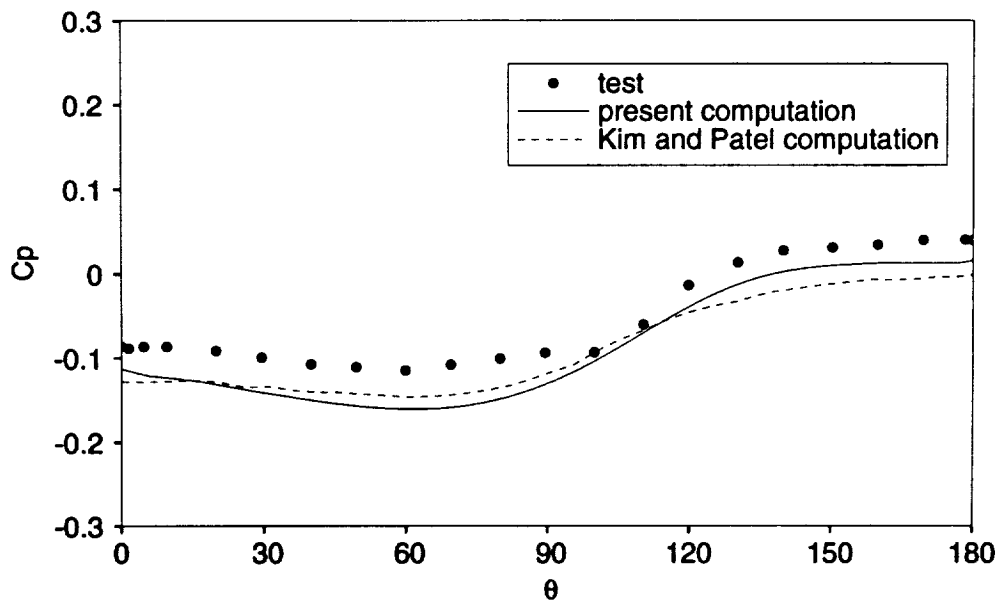
(c) $x = 0.523$ (d) $x = 0.689$

Figure 7.28 (Continued)



(e) $x = 0.835$

Figure 7.28 (Continued)

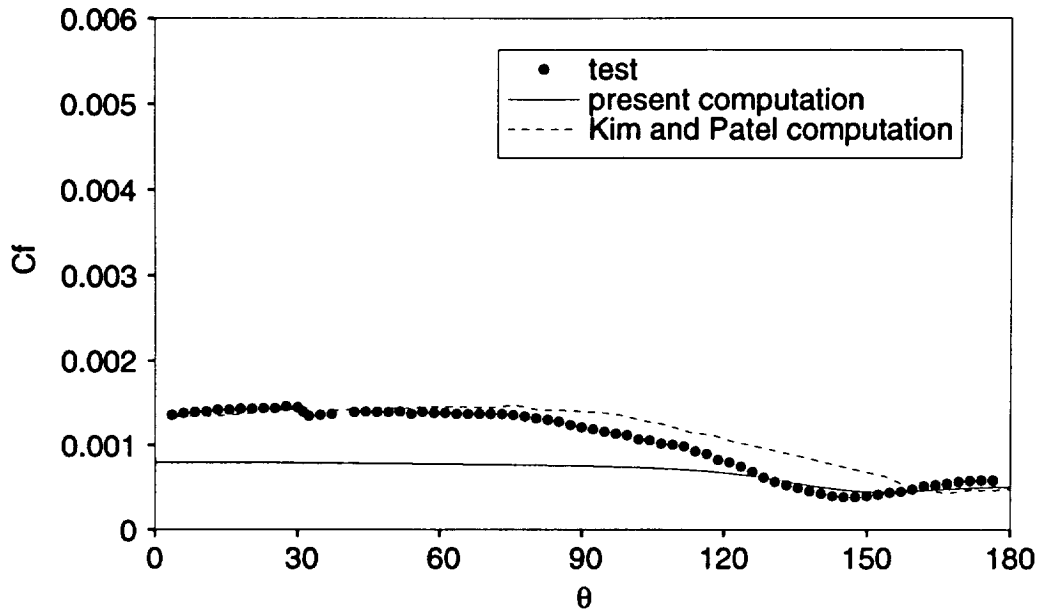
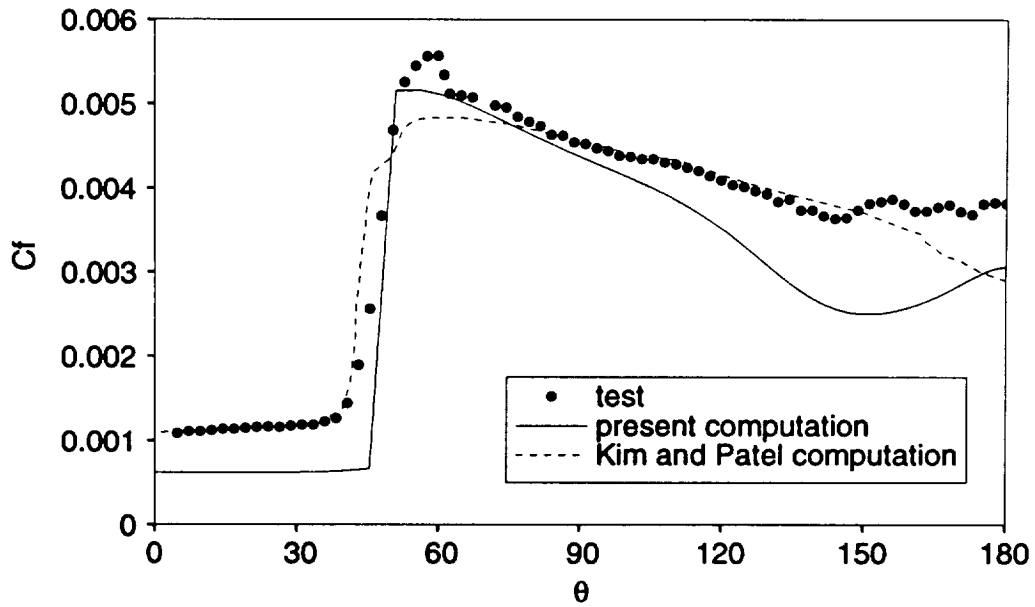
(a) $x = 0.223$ (b) $x = 0.395$

Figure 7.29: Friction coefficient, prolate spheroid

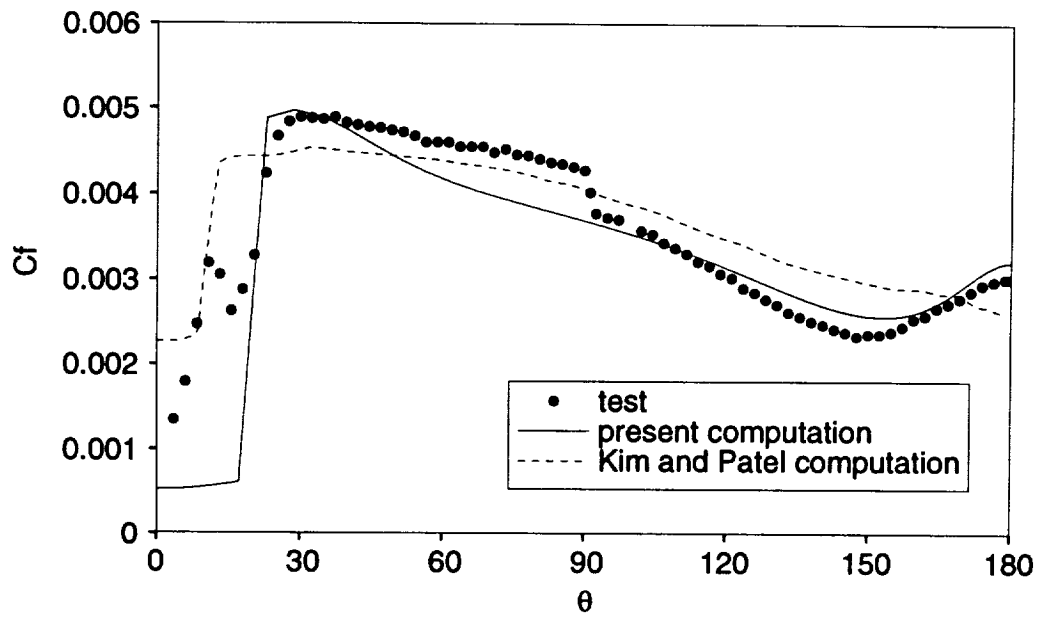
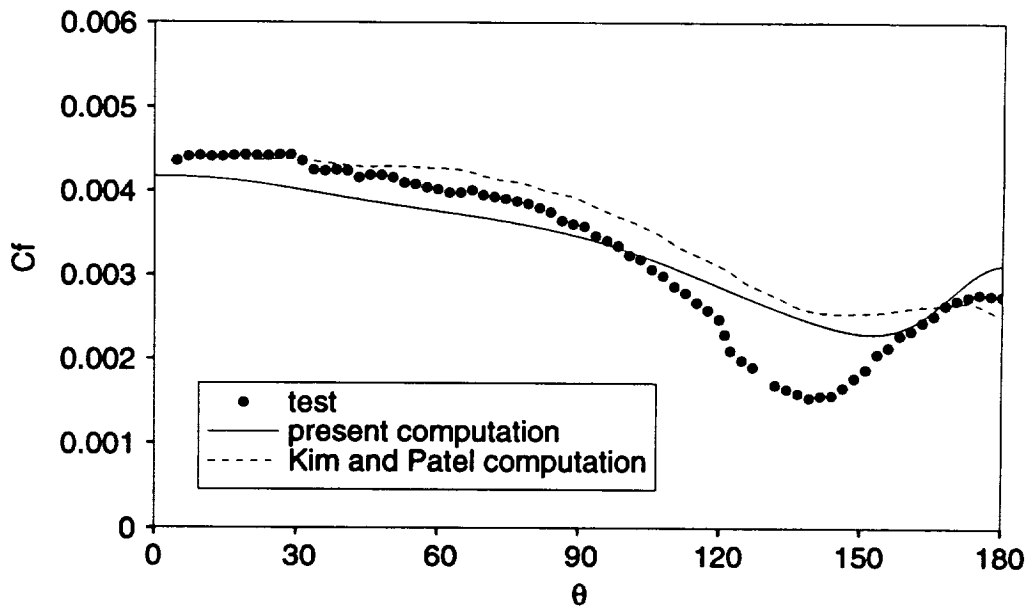
(c) $x = 0.565$ (d) $x = 0.738$

Figure 7.29 (Continued)

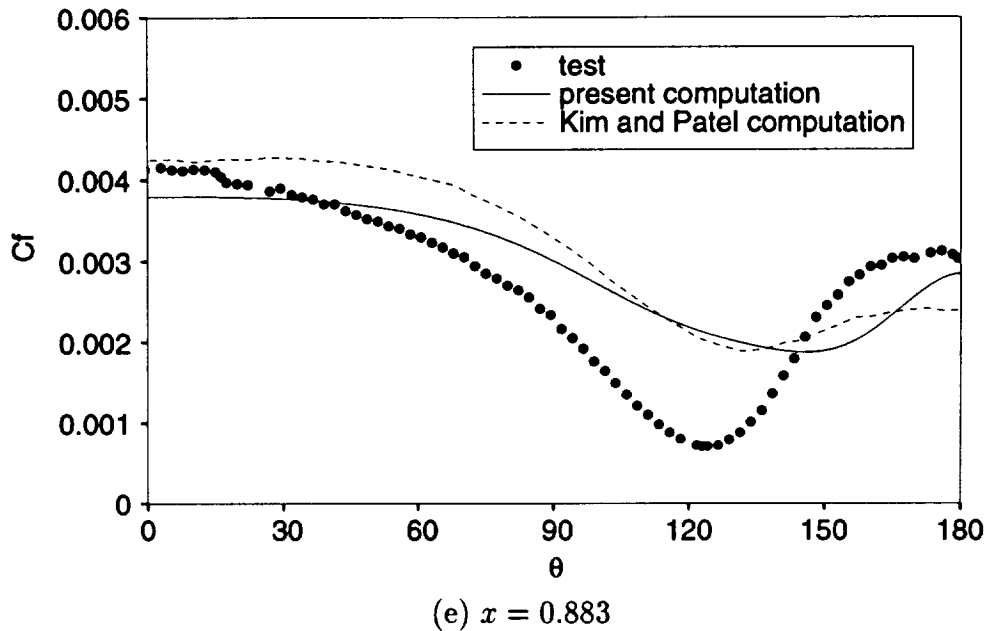


Figure 7.29 (Continued)

In the last two sections the dips in C_f are captured, but they are too close to the leeward symmetry plane. Neither computation does a very good job of predicting the magnitudes of the friction coefficients in the separated region.

In three-dimensional separated flows, the definition of the separation line is not as straightforward as in two-dimensional flows, because the flow does not necessarily reverse in the streamwise direction. In the present flowfield, the separation line may be defined as the line where the circumferential velocity component changes direction. Examining Figure 7.26, it is interesting to note that the separation line does not correspond to the line of minimum friction coefficient. At each cross-section the separation point is most clearly shown in plots of friction coefficient angle, where the line crosses $\gamma = 0$. The friction coefficient angle plots are shown in Figure 7.30. At the

first section, in which the flow is fully laminar (as may be seen in Figure 7.26), there is a separated region on the leeward side. At the second section, the flow on the leeward side has become turbulent, and it has reattached. As the flow moves downstream, it undergoes a second separation on the leeward side, and remains separated through the remaining measurement stations. The wall function computation captures the trend of the angles, but the magnitudes are not accurate, particularly in the separated regions. Near the aft end of the spheroid, the computed separation line is too close to the leeward symmetry plane. In order to help clarify the location of the computed separation line, top and side views of computed and experimental oil flow patterns are shown in Figures 7.31 and 7.32. It is also evident in these plots that the computed separation line is too close to the leeward symmetry plane.

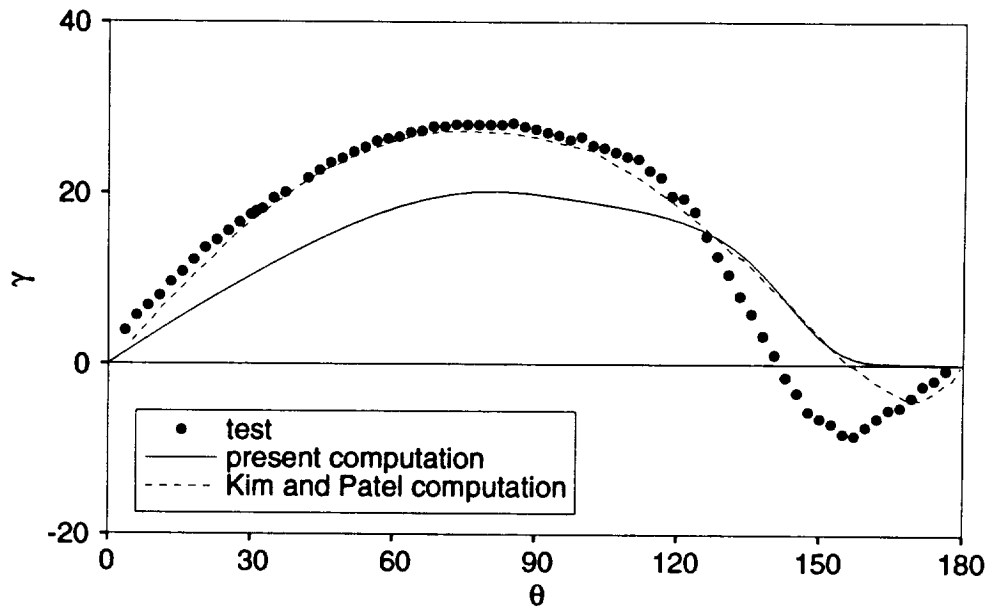
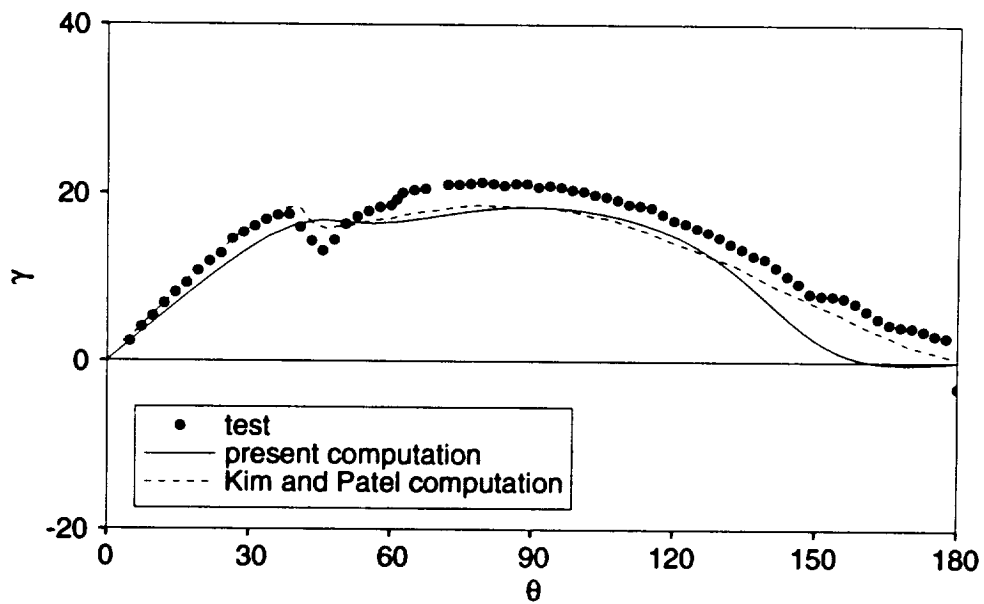
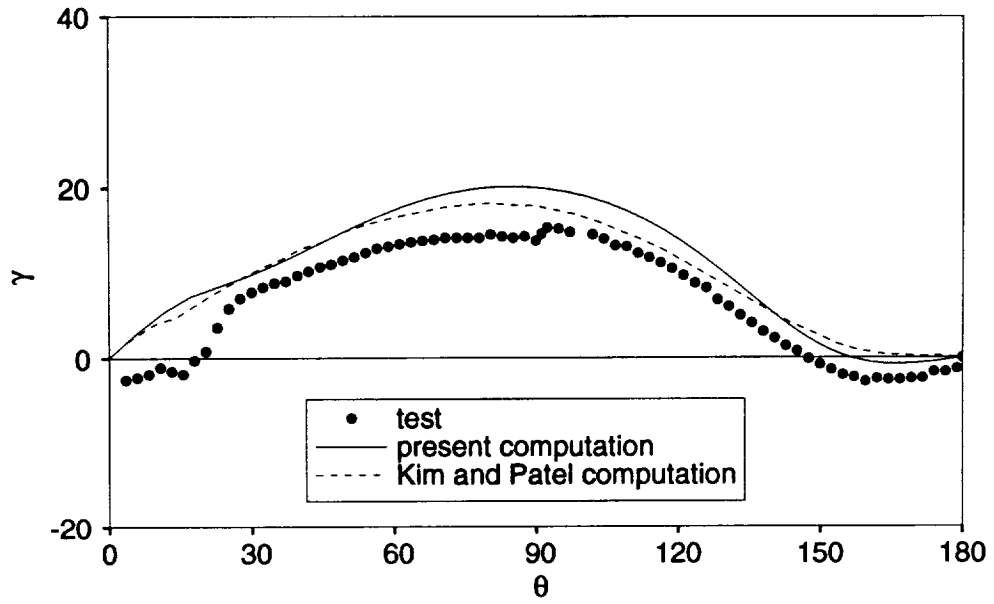
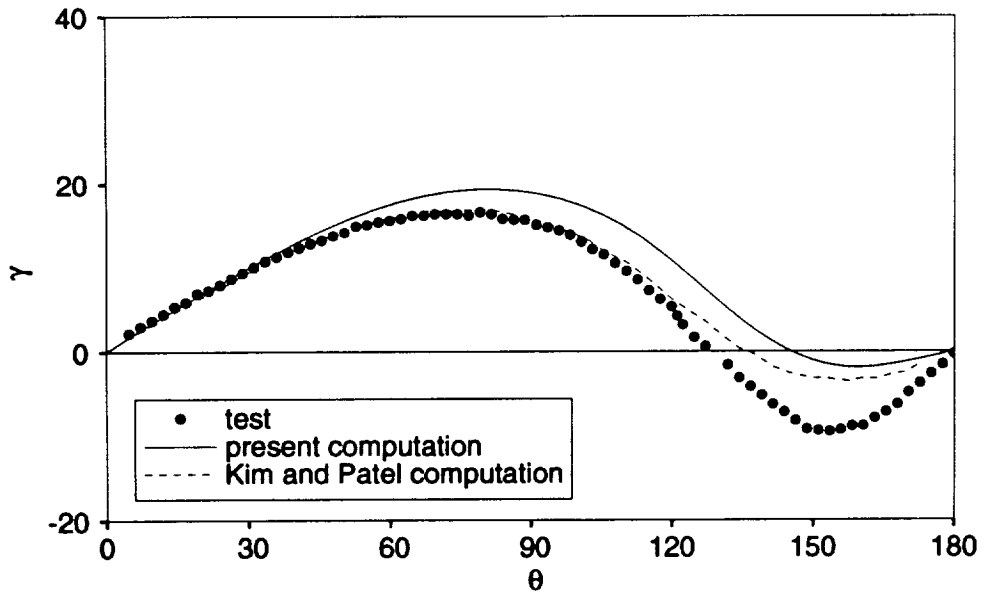
(a) $x = 0.223$ (b) $x = 0.395$

Figure 7.30: Friction coefficient angle, prolate spheroid

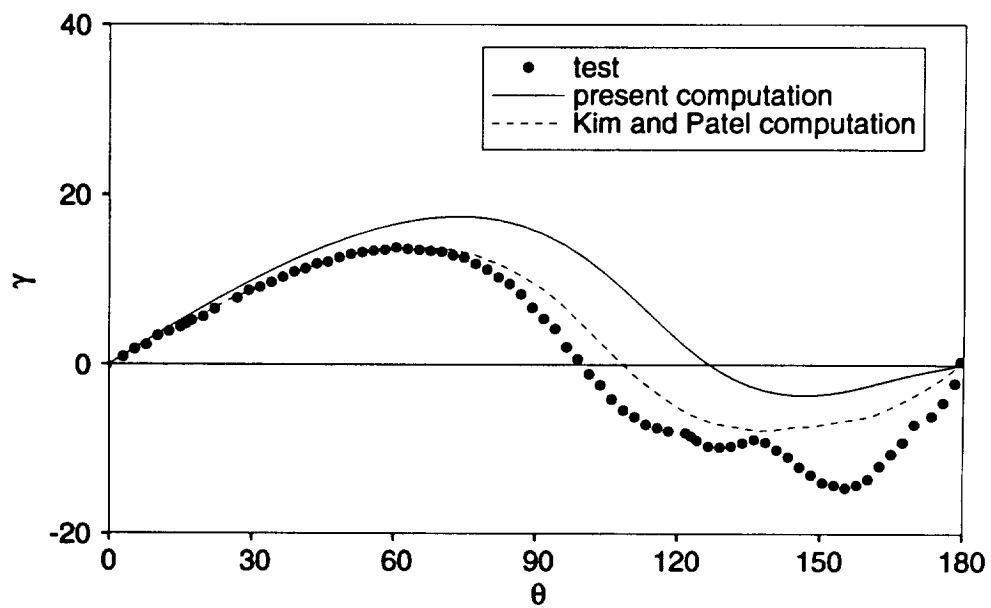


(c) $x = 0.565$



(d) $x = 0.738$

Figure 7.30 (Continued)



(e) $x = 0.883$

Figure 7.30 (Continued)

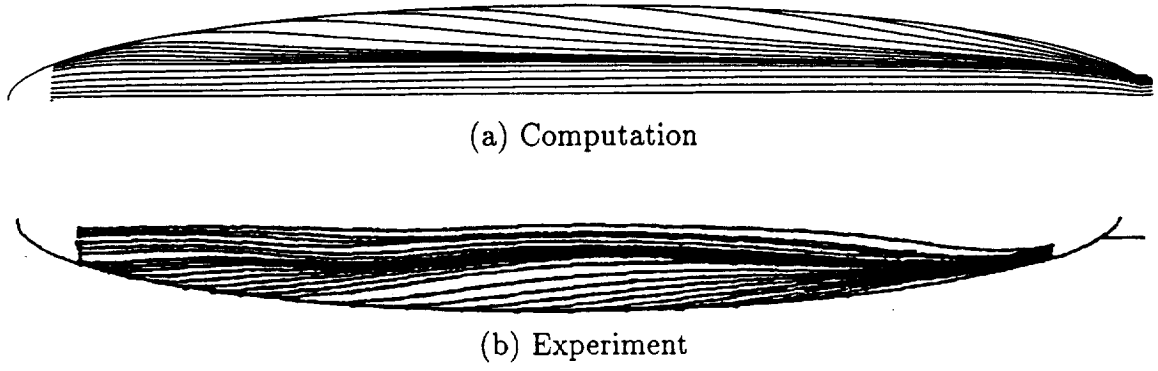
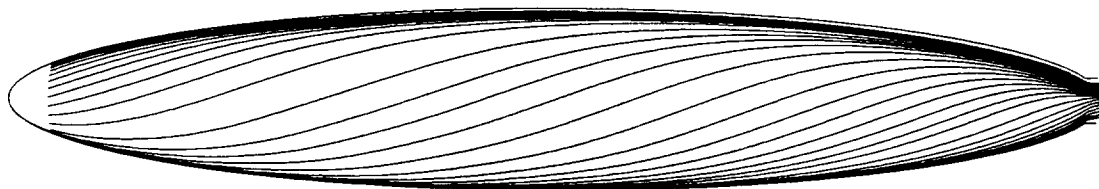
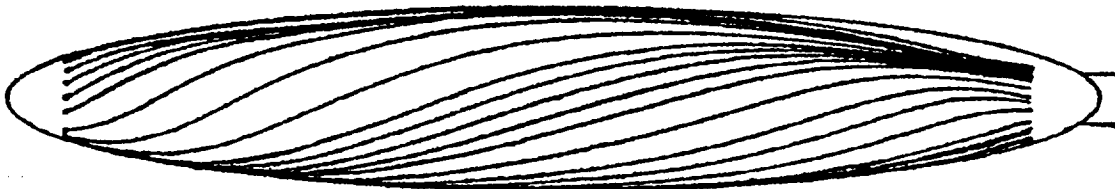


Figure 7.31: Surface oil flow pattern, top view



(a) Computation



(b) Experiment

Figure 7.32: Surface oil flow pattern, side view

8. CONCLUSIONS AND RECOMMENDATIONS

A method has been developed for the application of wall functions to generalized, curvilinear, nonorthogonal grids. It has been applied to a series of test cases of varying complexity. Flat plate test cases were first run to check for coding errors and to verify that the general formulation reduces correctly for this simple geometry. Computed friction coefficients were in good agreement with values from a semi-empirical equation. Since wall functions are based on the law of the wall, applicability of wall functions to these test cases was not an issue.

The test cases for the body of revolution at zero angle of attack were more challenging. This flowfield had favorable and adverse pressure gradients and curvature of the body surface. Pressure gradients were neglected in deriving the law of the wall, and if they are large, they may cause inaccuracies in the shear stress calculation. The standard $k - \epsilon$ model is also known to be less accurate for flows with adverse pressure gradients and/or strong streamline curvature (e.g., De Henneau, Raithby, and Thompson 1990). Even with these limitations, it was shown that the wall function formulation gave results comparable to the Baldwin-Lomax algebraic model and the Chien low-Reynolds-number $k - \epsilon$ model, all of which showed good agreement with test data when using a relatively fine grid. One of the primary advantages of wall functions is that they work well with coarse grid spacing, and this was also demon-

strated. As the grid spacing was increased, the wall functions continued to give good results while the other two models began to break down. The wall function solution did show a noticeable (though not drastic) change as the grid spacing at the wall was increased. This was attributed to the different boundary conditions used for k and ϵ in the viscous sublayer and the log region. Diminished grid resolution of the boundary layer may also have been a factor.

Solution of flow over a prolate spheroid at angle of attack is an ambitious goal for any turbulence model, and particularly for wall functions. The use of the law of the wall is questionable for separated flows, since the friction velocity may not be an appropriate velocity scale. Also, it may be necessary to resolve the flow close to the wall to accurately capture the location of the separation line if the boundary layer is highly skewed. Even so, wall functions have been shown in many instances to work well for fairly complex flowfields, so their use for this case is not out of the question. The goal of the present study was to demonstrate a method for applying wall functions to general geometries. The effectiveness of wall functions for solving complex flowfields is a related but separate issue.

The friction coefficients from the computation compared reasonably well with the test data in the regions of attached turbulent flow, and were comparable in accuracy to the two-equation model with a one-equation model patched in at the wall used by Kim and Patel (1991). Since the friction coefficient is computed directly from the wall function equations, it is the most important parameter to test the present formulation. The friction coefficient angle and separation line location did not match the test data as well as the friction coefficients, although the agreement was not unreasonable.

The problem of resolving the boundary layer in the laminar regions of the flowfield has several potential solutions. One is simply to use a finer grid. One of the main reasons for using wall functions is to permit the use of coarser grids, thereby saving grid points, so this solution is not ideal. A grid could be chosen which is a compromise between the two requirements, however. Another solution would be to use varying wall spacing. The wall spacing could be finer near the nose of the body and gradually become coarser downstream. Alternatively, a separate grid with fine wall spacing could be patched into the nose region. The flowfield could then be solved using a grid-embedding technique such as chimera (Benek, Buning, and Steger 1985).

There are several improvements which should be investigated to improve the wall function solution. It is possible to derive a modified law of the wall which accounts for streamwise pressure gradients (Ferrari 1959). The application of this equation to numerical schemes is not completely straightforward, since the equation takes on an indeterminate form as the pressure gradient approaches zero. There is a well defined limit at this point, however, so the problem should be surmountable. Although the pressure gradient is usually neglected in standard wall function formulations, its effect can be large (Mellor 1966; Tennekes and Lumley 1972), so the use of the modified law of the wall should improve the solution for flows with significant pressure gradients. It would be worthwhile to investigate this modification by solving a flowfield that is simpler than the prolate spheroid at angle of attack. A separating boundary layer in a two-dimensional diverging channel is a good choice.

A related possible improvement to the present formulation involves the application of the computed shear stress to the right hand side of the Navier-Stokes equations. The shear stress at a point between the wall and the grid point adjacent to

the wall is presently assumed to equal the wall shear stress. If the boundary layer assumption is invoked, the streamwise momentum equation evaluated at the wall yields the gradient of the shear stress as a function of streamwise pressure gradient. A better estimate of the shear stress near the wall is therefore possible. Although the boundary layer assumption is not correct in some regions of the flowfield, this modification should still be an improvement over neglecting the pressure gradient altogether.

As mentioned above, the $k - \epsilon$ model requires attention for flows with strong adverse pressure gradients and streamline curvature. Various modifications have been proposed (Launder, Priddin, and Sharma 1977; Hanjalic and Launder 1980; Rodi and Scheuerer 1983; Pourahmadi and Humphrey 1983). Evaluation of these modifications for relatively simple flowfields would be of value. The most promising formulation could then be applied to the prolate spheroid problem. The use of wall functions on curved surfaces should not pose any problems, since the law of the wall has been observed to hold close to both convex and concave surfaces (Moser and Moin 1987).

Since neither the present computation nor the computation of Kim and Patel (1991) gave accurate friction coefficients in the separated region of the flowfield (with the exception of the middle measurement station in the present computation), the problem may be in the $k - \epsilon$ model itself, rather than the wall treatment. Diagnosing this deficiency with the data available from the prolate spheroid measurements is difficult. It would be useful to have a detailed set of turbulence measurements (e.g. turbulent kinetic energy, Reynolds stress) available for a simpler separated flowfield such as flow over an airfoil or flow in a diverging duct. Computing the flowfield using

a variety of turbulence models would give insight into the specific deficiencies of each model.

9. REFERENCES

- Abid, R., Speziale, C. G., and Thangam, S. (1991). "Application of a New $K - \tau$ Model to Near Wall Turbulent Flows." AIAA paper 91-0614, presented at 29th Aerospace Sciences Meeting, Jan. 7-10, Reno, Nevada.
- Anderson, D. A., Tannehill, J. C., and Pletcher, R. H. (1984). *Computational Fluid Mechanics and Heat Transfer*. New York: McGraw-Hill.
- Anton, H. A. (1973). *Elementary Linear Algebra*. New York: John Wiley & Sons.
- Aris, R. (1962). *Vectors, Tensors, and the Basic Equations of Fluid Mechanics*. Englewood Cliffs: Prentice-Hall.
- Avva, R., Smith, C., and Singhal, A. (1990). "Comparative Study of High and Low Reynolds Number Versions of k-e Models." AIAA paper 90-0246, presented at the 28th Aerospace Sciences Meeting, Jan. 8-11, Reno, Nevada.
- Baldwin, B. S. and Lomax, H. (1978). "Thin Layer Approximation and Algebraic Model for Separated Turbulent Flows." AIAA paper 78-257, presented at the 16th Aerospace Sciences Meeting, Jan. 16-18, Huntsville, Alabama.
- Benek, J. A., Buning, P. G., and Steger, J. L. (1985). "A 3-D Chimera Grid Embedding Technique." AIAA paper 85-1523, presented at the 7th Computational Fluid Dynamics Conference, July 15-17, Cincinnati, Ohio.
- Bernard, P. S. (1986). "Limitations of the Near-Wall k-eps Turbulence Model." *AIAA Journal*, **24**, 619-622.
- Cebeci, T. and Smith, A. M. O. (1974). *Analysis of Turbulent Boundary Layers*. New York: Academic Press.

- Chan, W. and Steger, J. (1991). "A Generalized Scheme for Three-Dimensional Hyperbolic Grid Generation." AIAA paper 91-1588, presented at the 10th Computational Fluid Dynamics Conference, June 24-26, Honolulu, Hawaii.
- Chen, H. C. and Patel, V. C. (1987). "Practical Near-Wall Turbulence Models for Complex Flows Including Separation." AIAA paper 87-1300, presented at the 19th Fluid Dynamics, Plasma Dynamics, and Lasers Conference, June 8-10, Honolulu, Hawaii.
- Chien, K.-Y. (1982). "Predictions of Channel and Boundary-Layer Flows with a Low-Reynolds-Number Turbulence Model." *AIAA Journal*, **20**, 33-38.
- Chiang, C. C. and Launder, B. E. (1980). "On the Calculation of Turbulent Heat Transport Downstream From an Abrupt Pipe Expansion." *Numerical Heat Transfer*, **3**, 189-207.
- Chou, P. Y. (1945). "On Velocity Correlations and the Solutions of the Equations of Turbulent Fluctuation." *Quarterly of Applied Mathematics*, **3**, 38-54.
- Coakley, T. J. (1983). "Turbulence Modeling Methods for the Compressible Navier-Stokes Equations." AIAA paper 83-1693, presented at the 16th Fluid and Plasma Dynamics Conference, July 12-14, Danvers, Mass.
- Coles, D. E. (1956). "The Law of the Wake in the Turbulent Boundary Layer." *Journal of Fluid Mechanics*, **1**, 191-226.
- Coles, D. E. and Hirst, E. A., ed. (1969). *Proceedings, Computation of Turbulent Boundary Layers- 1968 AFOSR-IFP-Stanford Conference*. Vol. II, *Compiled Data*. Palo Alto: Thermosciences Division, Department of Mechanical Engineering, Stanford University.
- Daly, B. J. and Harlow, F. H. (1970). "Transport Equations in Turbulence." *The Physics of Fluids*, **13**, 2634-2649.
- De Henneau, V., Raithby, G. D., and Thompson, B. E. (1990). "Prediction of Flows with Strong Curvature and Pressure Gradient using the $k - \epsilon$ Turbulence Model." *ASME Journal of Fluid Mechanics*, **112**, 40-47.

- Deng, G. B., Piquet, J., and Queutey, P. (1990). "Navier-Stokes Computations of Vortical Flows." AIAA paper 90-1628, presented at the 21st Fluid Dynamics, Plasma Dynamics, and Lasers Conference, Aug. 17-19, Seattle, Wa.
- El Tahry, S. H. (1983). " $k - \epsilon$ Equation for Compressible Reciprocating Engine Flows." *Journal of Energy*, **7**, no. 4, 345-353.
- Ferrari, C. (1959). "Wall Turbulence." NASA Republication 2-8-59W, translation of Section C of the monograph entitled "Corso sulla Teoria della Turbolenza," from lectures delivered at the International Center of Mathematical Summer Studies (C.I.M.E.), Sept. 1-10, Varenna, Italy.
- Ferziger, J. H. (1987). "Simulation of Incompressible Turbulent Flows." *Journal of Computational Physics*, **69**, 1-48.
- Gibson, M. M., Jones, W. P., and Younis, B. A. (1981). "Calculation of Turbulent Boundary Layers on Curved Surfaces." *The Physics of Fluids*, **24**, 386-395.
- Gorski, J. J. (1984). "A New Near-Wall Formulation for the $k - \epsilon$ Equations of Turbulence." AIAA paper 86-0556, presented at 24th Aerospace Sciences Meeting, Jan. 6-9, Reno, Nevada.
- Hanjalic, K. and Launder, B. E. (1980). "Sensitizing the Dissipation Equation to Irrotational Strains." *ASME Journal of Fluids Engineering*, **102**, 34-40.
- Harlow, F. H. and Nakayama, P. I. (1967). "Turbulence Transport Equations." *The Physics of Fluids*, **10**, 2323-2332.
- Harlow, F. H. and Nakayama, P. I. (1968). "Transport of Turbulence Energy Decay Rate." Los Alamos: Los Alamos Scientific Laboratory. Report LA-3854.
- Hinze, J. O. (1987). *Turbulence*. 2nd ed. McGraw-Hill Classic Textbook Reissue Series. New York: McGraw-Hill.
- Hornbeck, R. W. (1975). *Numerical Methods*. New York: Quantum Publishers.
- Jones, W. P. and Launder, B. E. (1972). "The Prediction of Laminarization With a Two-Equation Model of Turbulence." *International Journal of Heat Transfer*, **15**, 301-314.

- Kaynak, Ü. and Flores, J. (1987). "Advances in the Computation of Transonic Separated Flows over Finite Wings." AIAA paper 87-1195, presented at the 19th Fluid Dynamics, Plasma Dynamics and Lasers Conference, June 8-10, Honolulu, Hawaii.
- Kim, S. E. and Patel, V. C. (1991). "Separation on a Spheroid at Incidence: Turbulent Flow." In *Proceedings of the Second Osaka International Colloquium on Viscous Fluid Dynamics in Ship and Ocean Technology, Osaka, Japan* by Osaka University. Osaka: Osaka University, 1-25.
- Kim, S.-W. and Chen, C.-P. (1989). "A Multiple-Time-Scale Turbulence Model Based on Variable Partitioning of the Turbulent Kinetic Energy Spectrum." *Numerical Heat Transfer, Part B*, **16**, 193-211.
- Klebanoff, P. S. (1955). "Characteristics of Turbulence in a Boundary Layer with Zero Pressure Gradient." Washington, D.C.: National Advisory Committee for Aeronautics. NACA Report 1247.
- Ko, S. H. and Rhode, D. L. (1990). "Derivation and Testing of a New Multi-Scale $k - \epsilon$ Turbulence Model." AIAA paper 90-1243, presented at the 28th Aerospace Sciences Meeting, Jan. 8-11, Reno, Nevada.
- Kreplin, H.-P., Meier, H. U., and Maier A. (1978). "Wind Tunnel Model and Measuring Techniques for the Investigation of Three-Dimensional Turbulent Boundary Layers." In *Proceedings of the AIAA 10th Aero. Testing Conference, San Diego, Ca.*, by the American Institute of Aeronautics and Astronautics. Washington, D.C.: American Institute of Aeronautics and Astronautics, 93-97.
- Kreplin, H.-P., Vollmers, H., and Meier, H. U. (1982). "Measurements of the Wall Shear Stress on an Inclined Prolate Spheroid." *Zeitschrift für Flugwissenschaft Weltraumforschung*, **6**, 248-252.
- Lauder, B. E. (1979). "Reynolds Stress Closures - Status and Prospects." in *Turbulent Boundary Layers - Experiments, Theory and Modelling: Proceedings of the 45th Panel Meeting/Symposium held in The Hague, Netherlands, Sept. 24-28*, by the Advisory Group for Aerospace Research and Development. AGARD Conference Proceedings No. 271. Neuilly sur Seine: the Advisory Group for Aerospace Research and Development. 13-1-13-13.
- Lauder, B. E. (1984). "Second-Moment Closure: Methodology and Practice." in *Turbulence Models and their Applications.*, vol. 2, Paris: Editions Eyrolles.

- Launder, B. E., Morse, A., Rodi, W., and Spalding, D. B. (1972). "Prediction of Free Shear Flows—A Comparison of the Performance of Six Turbulence Models." in *Free Turbulent Shear Flows: Proceedings of a conference held at NASA Langley Research Center, Hampton, Va., July 20-21*, by the National Aeronautics and Space Administration. NASA SP-321. Washington, D.C.: National Aeronautics and Space Administration. 361–426.
- Launder, B. E. and Spalding, D. B. (1974). "The Numerical Computation of Turbulent Flows." *Computer Methods in Applied Mechanics and Engineering*, **3**, 269–289.
- Launder, B. E., Priddin, C. H., and Sharma, B. I. (1977). "The Calculation of Turbulent Boundary Layers on Spinning and Curved Surfaces." *ASME Journal of Fluids Engineering*, **99**, 231–239.
- Lewis, J. P. and Pletcher, R. H. (1986). "A Boundary-Layer Computational Model for Predicting the Flow and Heat Transfer in Sudden Expansions." Ames: Iowa State University College of Engineering. Technical Report HTL-41, CFD-14.
- Mansour, N. N., Kim, J., and Moin, P. (1989). "Near-Wall $k - \epsilon$ Turbulence Modeling." *AIAA Journal*, **27**, 1068–1073.
- Meier, H. U. and Kreplin, H.-P. (1979). "Experimental Investigation of the Transition and Separation Phenomena on a Body of Revolution." *Proceedings of the 2nd Symposium on Turbulent Shear Flows, London, England, July 2-4, 1979*. London: Imperial College of Science and Technology, 15.1–15.7.
- Meier, H. U. and Kreplin, H.-P. (1980). "Experimental Investigation of the Boundary Layer Transition and Separation on a Body of Revolution." *Zeitschrift fur Flugwissenschaft Weltraumforschung*, **4**, 65–71.
- Meier, H. U., Kreplin, H.-P., and Vollmers, H. (1983). "Development of Boundary Layers and Separation Patterns on a Body of Revolution at Incidence." *Proceedings of the 2nd Symposium on Numerical and Physical Aspects of Aerodynamic Flows, Long Beach, Ca., Jan. 17-20*, by California State University at Long Beach. Long Beach: California State University, 1–9.
- Mellor, G. L. (1966). "The Effects of Pressure Gradients on Turbulent Flow Near a Smooth Wall." *Journal of Fluid Mechanics*, **24**, 255–274.

- Michelassi, V. and Shih, T.-H. (1991). Low Reynolds Number Two-Equation Modeling of Turbulent Flows." Washington, D. C.: National Aeronautics and Space Administration. NASA TM-104368.
- Monin, A. S. and Yaglom, A. M. (1987). *Statistical Fluid Mechanics: Mechanics of Turbulence*. vol. 1. Cambridge: The MIT Press.
- Moser, R. D. and Moin, P. (1987). "The Effects of Curvature in Wall-Bounded Turbulent Flows." *Journal of Fluid Mechanics*, **175**, 479-510.
- Norris, H. L. and Reynolds, W. C. (1975). "Turbulent Channel Flow with a Moving Wavy Boundary." Stanford: Stanford University. Department of Mechanical Engineering Technical Report TF-7.
- Pan, D. and Pulliam, T. H. (1986). "The Computation of Steady 3-D Separated Flows Over Aerodynamic Bodies at Incidence and Yaw." AIAA paper 86-0109, presented at the 24th Aerospace Sciences Meeting, Jan. 6-9, Reno, Nevada.
- Panaras, A. G. and Steger, J. L. (1988). "A Thin-Layer Solution of the Flow about a Prolate Spheroid." *Zeitschrift fur Flugwissenschaft Weltraumforschung*, **12**, 173-180.
- Patankar, S. V. and Spalding, D. B. (1970). *Heat and Mass Transfer in Boundary Layers*. 2nd ed. London: Intertext Books.
- Patel, V. P., Rodi, W., and Scheuerer, G. (1985). "Turbulence Models for Near-Wall and Low Reynolds Number Flows: A Review." *AIAA Journal*, **23**, 1308-1319.
- Peterson, V. L., Kim, J., Holst, T. L., Diewert, G. S., Cooper, D. M., Watson, A. B., and Bailey, F. R. (1989). "Supercomputer Requirements for Selected Disciplines Important to Aerospace." *Journal of I.E.E.E.*, **77**.
- Pourahmadi, F. and Humphrey, A. C. (1983). "Prediction of Curved Channel Flow with an Extended $k - \epsilon$ Model of Turbulence." *AIAA Journal*, **21**, 1365-1373.
- Pulliam, T. H. (1984). "Euler and Thin Layer Navier-Stokes Codes: ARC2D, ARC3D." *notes for Computational Fluid Dynamics User's Workshop held at The University of Tennessee Space Institute, Tullahoma, Tennessee, March 12-16*. Tullahoma: University of Tennessee Space Institute. Photocopied.

- Pulliam, T. H. (1985). "Artificial Dissipation Models for the Euler Equations." AIAA paper 85-0438, presented at the 23rd Aerospace Sciences Meeting, Jan. 14-17, Reno, Nevada.
- Rai, M. M. and Moin, P. (1989). "Direct Simulations of Turbulent Flow using Finite-Difference Schemes." AIAA paper 89-0369, presented at the 27th Aerospace Sciences Meeting, Jan. 9-12, Reno, Nevada.
- Ramaprian, B. R., Patel, V. C., and Choi, D. H. (1978). *Mean Flow Measurements in the Three-Dimensional Boundary Layer over a Body of Revolution at Incidence*. Iowa City: Iowa Institute of Hydraulic Research, The University of Iowa. IIHR Limited Distribution Report No. 56.
- Ramaprian, B. R., Patel, V. C., and Choi, D. H. (1981). "Mean Flow Measurements in the Three-Dimensional Boundary Layer over a Body of Revolution at Incidence." *Journal of Fluid Mechanics*, **103**, 479-504.
- Reynolds, O. (1895). "On the Dynamical Theory of Incompressible Viscous Fluids and the Determination of the Criterion." *Philosophical Transactions of the Royal Society of London*, **186**, Series A, 123-164.
- Rodi, W. (1972). "The Prediction of Free Turbulent Boundary Layers by the Use of a Two-Equation Model of Turbulence." Ph.D. thesis, Imperial College, London.
- Rodi, W. (1980). *Turbulence Models and their Application in Hydraulics — A State of the Art Review*. Delft: International Association for Hydraulic Research.
- Rodi, W. (1991). "Experience with Two-Layer Models Combining the $k - \epsilon$ Model with a One-Equation Model Near the Wall." AIAA paper 91-0216, presented at the 29th Aerospace Sciences Meeting, Jan. 7-10, Reno, Nevada.
- Rodi, W. and Scheuerer, G. (1983). "Calculation of Curved Shear Layers with Two-Equation Turbulence Models." *Physics of Fluids*, **26**, 1422-1436.
- Rodi, W. and Spalding, D. B. (1970). "A Two-Parameter Model of Turbulence, and its Application to Free Jets." *Warme-und Stoffubertragung*, **3**, 85-95.
- Schetz, J. A. (1980). *Injection and Mixing in Turbulent Flow*. New York: American Institute of Aeronautics and Astronautics.
- Schlichting, H. (1984). *Boundary-Layer Theory*. 7th ed. New York: McGraw-Hill.

- Shih, T. H. and Mansour, N. N. (1990). "Modeling of Near-Wall Turbulence." in *Proceedings of the CFD Symposium on Aeropropulsion at the NASA Lewis Research Center in Cleveland, Ohio, Apr. 24-26*, by the National Aeronautics and Space Administration. Washington, D.C.: National Aeronautics and Space Administration, 1-11.
- Shih, T. H. and Hsu, A. T. (1991). "An Improved $k - \epsilon$ Model for Near-Wall Turbulence." AIAA paper 91-0611, presented at the 29th Aerospace Sciences Meeting, Jan. 7-10, Reno, Nevada.
- Shih, T. I.-P. and Chyu, W. J. (1991). "Approximate Factorization with Source Terms." *AIAA Journal*, **29**, 1759-1760.
- Sokolnikoff, I. S. (1964). *Tensor Analysis Theory and Applications to Geometry and Mechanics of Continua*. 2nd ed. New York: John Wiley & Sons.
- Speziale, C. G. (1987). "On Nonlinear $K - l$ and $K - \epsilon$ Models of Turbulence." *Journal of Fluid Mechanics*, **178**, 459-475.
- Steger, J. L. and Warming, R. F. (1981). "Flux Vector Splitting of the Inviscid Gasdynamic Equations with Application to Finite-Difference Methods." *Journal of Computational Physics*, **40**, 263-293.
- Taylor, G. I. (1935). "Statistical Theory of Turbulence." *Proceedings of the Royal Society of London*, **151A**, 421-478.
- Tennekes, H. and Lumley, J. L. (1972). *A First Course in Turbulence*. Cambridge: The MIT Press.
- Van Driest, E. R. (1956). "On Turbulent Flow Near a Wall." *Journal of the Aeronautical Sciences*, **23**, 1007-1011, 1036.
- Vatsa, V. N., Thomas, J. L., and Wedan, B. W. (1987). "Navier-Stokes Computations of Prolate Spheroids at Angle of Attack." AIAA paper 87-2627, presented at the Atmospheric Flight Mechanics Conference, Aug. 17-19, Monterey, Ca.
- Viegas, J. R. and Rubesin, M. W. (1983). "Wall-Function Boundary Conditions in the Solution of the Navier-Stokes Equations for Complex Compressible Flows." AIAA paper 83-1694, presented at the 16th Fluid and Plasma Dynamics Conference, July 12-14, Danvers, Mass.

- Viegas, J. R., Rubesin, M. W., and Horstman, C. C. (1985). "On the Use of Wall Functions as Boundary Conditions for Two-Dimensional Separated Compressible Flows." AIAA paper 85-0180, presented at the 23rd Aerospace Sciences Meeting, Jan. 14-17, Reno, Nevada.
- White, F. M. (1974). *Viscous Fluid Flow*. New York: McGraw-Hill.
- Wilcox, D. C. (1988). "Reassessment of the Scale-Determining Equation for Advanced Turbulence Models." *AIAA Journal*, **26**, 1299-1310.
- Wong, T.-C., Kandil, O. A., and Liu, C. H. (1989). "Navier-Stokes Computations of Separated Vortical Flows Past Prolate Spheroid at Incidence." AIAA paper 89-0553, presented at the 27th Aerospace Sciences Meeting, Jan. 9-12, Reno, Nevada.
- Yakhot, V. and Orszag, S. A. (1986). "Renormalization Group Analysis of Turbulence. I. Basic Theory." *Journal of Scientific Computing*, **1**, 3-51.
- Ying, S. X., Steger, J. L., Schiff, L. B., and Baganoff, D. (1986). "Numerical Simulation of Unsteady, Viscous, High-Angle-of-Attack Flows Using a Partially Flux-Split Algorithm." AIAA paper 86-2179, presented at the 13th Atmospheric Flight Mechanics Conference, Aug. 18-20, Williamsburg, Virginia.
- Yoshizawa, A. (1988). "Statistical Modelling of Passive-Scalar Diffusion in Turbulent Shear Flows." *Journal of Fluid Mechanics*, **195**, 541-555.

10. APPENDIX A: FLUX JACOBIANS

10.1 Navier-Stokes

Before presenting these matrices, a word about their derivation is in order. Each flux vector may be considered to be a function of both the dependent variable vector Q and its spatial derivatives, for example $\partial Q/\partial x$. We may therefore write for a one-dimensional equation

$$\begin{aligned} A &= \frac{\partial E}{\partial Q} \\ &= \frac{\partial E(Q, Q_x)}{\partial Q} + \frac{\partial E(Q, Q_x)}{\partial Q_x} \frac{\partial Q_x}{\partial Q} \end{aligned} \quad (10.1)$$

It is common practice to neglect the second term on the right hand side (e.g. Pulliam 1984), and this approximation will be made here. Using the notation of Pulliam, the Jacobian matrices are as follows.

$$\hat{A} = \begin{bmatrix} \xi_t & \xi_x & \xi_y & & & \\ -u\theta + \xi_x\phi^2 & \xi_t + \theta - (\gamma - 2)\xi_x u & \xi_y u - (\gamma - 1)\xi_x v & & & \\ -v\theta + \xi_y\phi^2 & \xi_x v - (\gamma - 1)\xi_y u & \xi_t + \theta - (\gamma - 2)\xi_y v & & & \\ -w\theta + \xi_z\phi^2 & \xi_x w - (\gamma - 1)\xi_z u & \xi_y w - (\gamma - 1)\xi_z v & & & \\ \theta[\phi^2 - a_1] & \xi_x a_1 - (\gamma - 1)u\theta & \xi_y a_1 - (\gamma - 1)v\theta & & & \\ & & & \xi_z & 0 & \\ & & & \xi_z u - (\gamma - 1)\xi_x w & (\gamma - 1)\xi_x & \\ & & & \xi_z v - (\gamma - 1)\xi_y w & (\gamma - 1)\xi_y & \\ & & & \xi_t + \theta - (\gamma - 2)\xi_z w & (\gamma - 1)\xi_z & \\ & & & \xi_z a_1 - (\gamma - 1)w\theta & \gamma\theta + \xi_t & \end{bmatrix} \quad (10.2)$$

where

$$a_1 = \frac{\gamma\mathcal{E}}{\rho} - \phi^2 \quad (10.3)$$

$$\theta = \xi_x u + \xi_y v + \xi_z w \quad (10.4)$$

$$\phi^2 = \frac{1}{2}(\gamma - 1)(u^2 + v^2 + w^2) \quad (10.5)$$

The flux Jacobians \hat{B} and \hat{C} are identical to the above matrix, with the exception that all occurrences of ξ are replaced with η or ζ respectively.

The viscous Jacobian, neglecting cross-derivative terms, is

$$\hat{A}^v = \begin{bmatrix} 0 & 0 & 0 & 0 & 0 \\ m_{21} & \alpha_1 \frac{\partial \rho^{-1}}{\partial \xi} & \alpha_2 \frac{\partial \rho^{-1}}{\partial \xi} & \alpha_3 \frac{\partial \rho^{-1}}{\partial \xi} & 0 \\ m_{31} & \alpha_2 \frac{\partial \rho^{-1}}{\partial \xi} & \alpha_4 \frac{\partial \rho^{-1}}{\partial \xi} & \alpha_5 \frac{\partial \rho^{-1}}{\partial \xi} & 0 \\ m_{41} & \alpha_3 \frac{\partial \rho^{-1}}{\partial \xi} & \alpha_5 \frac{\partial \rho^{-1}}{\partial \xi} & \alpha_6 \frac{\partial \rho^{-1}}{\partial \xi} & 0 \\ m_{51} & m_{52} & m_{53} & m_{54} & m_{55} \end{bmatrix} \quad (10.6)$$

where

$$m_{21} = -\alpha_1 \frac{\partial}{\partial \xi} \left(\frac{u}{\rho} \right) - \alpha_2 \frac{\partial}{\partial \xi} \left(\frac{v}{\rho} \right) - \alpha_3 \frac{\partial}{\partial \xi} \left(\frac{w}{\rho} \right) \quad (10.7)$$

$$m_{31} = -\alpha_2 \frac{\partial}{\partial \xi} \left(\frac{u}{\rho} \right) - \alpha_4 \frac{\partial}{\partial \xi} \left(\frac{v}{\rho} \right) - \alpha_5 \frac{\partial}{\partial \xi} \left(\frac{w}{\rho} \right) \quad (10.8)$$

$$m_{41} = -\alpha_3 \frac{\partial}{\partial \xi} \left(\frac{u}{\rho} \right) - \alpha_5 \frac{\partial}{\partial \xi} \left(\frac{v}{\rho} \right) - \alpha_6 \frac{\partial}{\partial \xi} \left(\frac{w}{\rho} \right) \quad (10.9)$$

$$\begin{aligned} m_{51} &= \alpha_0 \frac{\partial}{\partial \xi} \left[-\frac{\mathcal{E}}{\rho^2} + \frac{1}{\rho} (u^2 + v^2 + w^2) \right] \\ &- \alpha_1 \frac{\partial}{\partial \xi} \left(\frac{u^2}{\rho} \right) - \alpha_2 \frac{\partial}{\partial \xi} \left(\frac{2uv}{\rho} \right) - \alpha_3 \frac{\partial}{\partial \xi} \left(\frac{2uw}{\rho} \right) \\ &- \alpha_4 \frac{\partial}{\partial \xi} \left(\frac{v^2}{\rho} \right) - \alpha_5 \frac{\partial}{\partial \xi} \left(\frac{2vw}{\rho} \right) - \alpha_6 \frac{\partial}{\partial \xi} \left(\frac{w^2}{\rho} \right) \end{aligned} \quad (10.10)$$

$$m_{52} = -m_{21} - \alpha_0 \frac{\partial}{\partial \xi} \left(\frac{u}{\rho} \right) \quad (10.11)$$

$$m_{53} = -m_{31} - \alpha_0 \frac{\partial}{\partial \xi} \left(\frac{v}{\rho} \right) \quad (10.12)$$

$$m_{54} = -m_{41} - \alpha_0 \frac{\partial}{\partial \xi} \left(\frac{w}{\rho} \right) \quad (10.13)$$

$$m_{55} = \alpha_0 \frac{\partial}{\partial \xi} \left(\frac{1}{\rho} \right) \quad (10.14)$$

$$\alpha_0 = \gamma \left(\frac{\mu}{Pr} + \frac{\mu_t}{Pr_t} \right) (\xi_x^2 + \xi_y^2 + \xi_z^2) \quad (10.15)$$

$$\alpha_1 = (\mu + \mu_t) \left(\frac{4}{3} \xi_x^2 + \xi_y^2 + \xi_z^2 \right) \quad (10.16)$$

$$\alpha_2 = \frac{1}{3} (\mu + \mu_t) \xi_x \xi_y \quad (10.17)$$

$$\alpha_3 = \frac{1}{3} (\mu + \mu_t) \xi_x \xi_z \quad (10.18)$$

$$\alpha_4 = (\mu + \mu_t) \left(\xi_x^2 + \frac{4}{3} \xi_y^2 + \xi_z^2 \right) \quad (10.19)$$

$$\alpha_5 = \frac{1}{3} (\mu + \mu_t) \xi_y \xi_z \quad (10.20)$$

$$\alpha_6 = (\mu + \mu_t) \left(\xi_x^2 + \xi_y^2 + \frac{4}{3} \xi_z^2 \right) \quad (10.21)$$

As with the inviscid Jacobians, the viscous Jacobians for the other two coordinate directions may be obtained by substituting η or ζ for ξ in the above equations.

10.2 $k - \epsilon$

For the standard $k - \epsilon$ model, the source term Jacobian is

$$\hat{D}_t = \begin{bmatrix} 2c_\mu \mathcal{A} \frac{k}{\epsilon} - \mathcal{B} & -c_\mu \mathcal{A} \left(\frac{k}{\epsilon} \right)^2 - 1 \\ c_1 c_\mu \mathcal{A} + c_2 \left(\frac{\epsilon}{k} \right)^2 & -c_1 \mathcal{B} - 2c_2 \frac{\epsilon}{k} \end{bmatrix} \quad (10.22)$$

where

$$\mathcal{A} = \left(\frac{\partial u_i}{\partial x_j} + \frac{\partial u_j}{\partial x_i} - \frac{2}{3} \delta_{ij} \frac{\partial u_k}{\partial x_k} \right) \frac{\partial u_i}{\partial x_j} \quad (10.23)$$

and

$$\mathcal{B} = -\frac{2}{3} \frac{\partial u_k}{\partial x_k} \quad (10.24)$$

11. APPENDIX B: $k - \epsilon$ SOLVER

11.1 Banded Solver

The k and ϵ transport equations are coupled to one another through the diffusion terms and the source terms. In linearizing the diffusion terms, the turbulent viscosity was taken from the previous time step, so the only remaining coupling is through the source terms. The linearized source terms have been included in the ζ direction factor, so the k and ϵ equations in the ξ and η direction factors are uncoupled from one another. A scalar banded solver may therefore be used for these factors.

The form of the system of equations is

$$\mathbf{Ax} = \mathbf{B} \quad (11.1)$$

where boldface print is used for matrices and vectors. The structure of the \mathbf{A} matrix is shown in Figure 11.1, the vector of unknowns (\mathbf{x}) in Figure 11.2, and the right hand side (\mathbf{B}) in Figure 11.3. The lower diagonal is eliminated as follows:

$$b_{k_i}^* = b_{k_i} - c_{k(i-1)} \frac{a_{k_i}}{b_{k(i-1)}} \quad (11.2)$$

$$b_{\epsilon_i}^* = b_{\epsilon_i} - c_{\epsilon(i-1)} \frac{a_{\epsilon_i}}{b_{\epsilon(i-1)}} \quad (11.3)$$

$$B_{k_i}^* = B_{k_i} - B_{k(i-1)} \frac{a_{k_i}}{b_{k(i-1)}} \quad (11.4)$$

$$\begin{array}{c}
 \left[\begin{array}{ccc}
 \begin{bmatrix} b_{k_2} & 0 \\ 0 & b_{\epsilon_2} \end{bmatrix} & \begin{bmatrix} c_{k_2} & 0 \\ 0 & c_{\epsilon_2} \end{bmatrix} & \\
 \begin{bmatrix} a_{k_3} & 0 \\ 0 & a_{\epsilon_3} \end{bmatrix} & \begin{bmatrix} b_{k_3} & 0 \\ 0 & b_{\epsilon_3} \end{bmatrix} & \begin{bmatrix} c_{k_3} & 0 \\ 0 & c_{\epsilon_3} \end{bmatrix} \\
 & \begin{bmatrix} a_{k_4} & 0 \\ 0 & a_{\epsilon_4} \end{bmatrix} & \begin{bmatrix} b_{k_4} & 0 \\ 0 & b_{\epsilon_4} \end{bmatrix} & \begin{bmatrix} c_{k_4} & 0 \\ 0 & c_{\epsilon_4} \end{bmatrix} \\
 \vdots & & \cdot & \\
 \vdots & & \cdot & \\
 \vdots & & \cdot &
 \end{array} \right]
 \end{array}$$

Figure 11.1: Structure of banded matrix

$$\begin{array}{c}
 \left[\begin{array}{c}
 \begin{bmatrix} x_{k_2} \\ x_{\epsilon_2} \end{bmatrix} \\
 \begin{bmatrix} x_{k_3} \\ x_{\epsilon_3} \end{bmatrix} \\
 \begin{bmatrix} x_{k_4} \\ x_{\epsilon_4} \end{bmatrix} \\
 \vdots \\
 \vdots \\
 \vdots
 \end{array} \right]
 \end{array}$$

Figure 11.2: Structure of vector of unknowns

$$\begin{bmatrix} \begin{bmatrix} B_{k_2} \\ B_{\epsilon_2} \end{bmatrix} \\ \begin{bmatrix} B_{k_3} \\ B_{\epsilon_3} \end{bmatrix} \\ \begin{bmatrix} B_{k_4} \\ B_{\epsilon_4} \end{bmatrix} \\ \vdots \\ \vdots \\ \vdots \end{bmatrix}$$

Figure 11.3: Structure of right hand side

$$B_{\epsilon_i}^* = B_{\epsilon_i} - B_{\epsilon_{(i-1)}} \frac{a_{\epsilon_i}}{b_{\epsilon_{(i-1)}}} \quad (11.5)$$

The “*” indicates a revised value and i is the row number. These equations are applied to each row starting from $i = 3$ (the second row).

The back substitution starts at the last row in the matrix, $N - 1$, where N is the total number of grid points. For the last row,

$$x_{k_{(N-1)}} = \frac{B_{k_{(N-1)}}^*}{b_{k_{(N-1)}}^*} \quad (11.6)$$

and

$$x_{\epsilon_{(N-1)}} = \frac{B_{\epsilon_{(N-1)}}^*}{b_{\epsilon_{(N-1)}}^*} \quad (11.7)$$

Marching backwards through the remaining rows,

$$x_{k_i} = \frac{B_{k_i}^* - c_{k_i} x_{(i+1)}}{b_{k_i}^*} \quad (11.8)$$

and

$$x_{\epsilon_i} = \frac{B_{\epsilon_i}^* - c_{\epsilon_i} x_{i+1}}{b_{\epsilon_i}^*} \quad (11.9)$$

This fully solves the system.

11.2 Block Solver

The equations in the ζ direction factor are coupled through the linearized source terms, so a block tridiagonal solver is required. Since the blocks are 2×2 , they may be inverted algebraically. For a general nonsingular 2×2 matrix

$$[\mathbf{Q}] = \begin{bmatrix} q & r \\ s & t \end{bmatrix} \quad (11.10)$$

the inverse is given by (e.g. Anton 1973)

$$[\mathbf{Q}]^{-1} = \frac{1}{qt - rs} \begin{bmatrix} t & -r \\ -s & q \end{bmatrix} \quad (11.11)$$

The procedure used here is a standard block tridiagonal solver with algebraic inversions. The structure of the block matrix is shown in Figure 11.4. The solution procedure is similar to that for the banded scalar tridiagonal matrix. The lower diagonal is eliminated with the equations

$$[\mathbf{b}_i^*] = [\mathbf{b}_i] - [\mathbf{a}_i] [\mathbf{b}_{(i-1)}]^{-1} [\mathbf{c}_{(i-1)}] \quad (11.12)$$

and

$$[\mathbf{B}_i^*] = [\mathbf{B}_i] - [\mathbf{a}_i] [\mathbf{b}_{(i-1)}]^{-1} [\mathbf{B}_{(i-1)}] \quad (11.13)$$

The backsweep begins in the last row,

$$[\mathbf{x}_{(N-1)}] = [\mathbf{b}_{(N-1)}^*]^{-1} [\mathbf{B}_{(i-1)}^*] \quad (11.14)$$

For the remaining rows,

$$[\mathbf{x}_i] = [\mathbf{b}_i^*]^{-1} \{ [\mathbf{B}_i^*] - [\mathbf{c}_i] [\mathbf{x}_{(i+1)}] \} \quad (11.15)$$

$$\begin{bmatrix} [\mathbf{b}_2] & [\mathbf{c}_2] & & \\ [\mathbf{a}_3] & [\mathbf{b}_3] & [\mathbf{c}_3] & \\ & [\mathbf{a}_4] & [\mathbf{b}_4] & [\mathbf{c}_4] \\ \vdots & & \cdot & \\ \vdots & & & \cdot \end{bmatrix}$$

Figure 11.4: Structure of block matrix

